Modelling, Observation and Control of Needle Steering in Soft Tissue

by

Bita Fallahi

A thesis submitted in partial fulfillment of the requirements for the degree of

Doctor of Philosophy

in

Control Systems

Department of Electrical and Computer Engineering

University of Alberta

Abstract

Steerable needles have been widely used in minimally-invasive surgical procedures such as brachytherapy, biopsy, and neurosurgery in which long flexible needles are inserted into the human body for treatment, diagnosis or sample removal. Prostate brachytherapy, known as a cost-effective and minimally invasive method, is a type of radiotherapy treatment which delivers radiation internally by implanting radioactive seeds at specific spots inside or around the prostate. Here accurate positioning of the needle plays a vital role as no proper treatment will happen if targeting accuracy is low. Moreover, poor placement of the radioactive seeds can cause long-term side effects due to the disruption of neighboring tissues or organs. Investigations reveal that using available techniques, even expert practitioners cannot achieve an average accuracy of less than 5 mm in seed placement. This may be improved by employing computer-controlled robots to compensate for the placement errors caused by needle deflection and tissue deformation.

This research aims to improve the needle placement accuracy using needle insertion robotic assistants. To this end, steering algorithms and controllers are employed in a feedback closed-loop structure. In these structures, the controllers are fed by needle tip deflection measurements, and perform any necessary control action to compensate the targeting errors. In this research different control strategies are proposed to compensate for the needle positioning errors. All the proposed controllers in this work are based on needle deflection measurements obtained from ultrasound images. To deal with system uncertainties, sliding

mode control technique is used to control the needle tip position in 2D and 3D environments. Considering the planar case, a switching controller is proposed to compensate the needle tip deflection in one plane. Considering the trade-off between the performance (small targeting error) and cost (tissue trauma), a controller tuning method is provided which ensures the stability of the closed-loop system. This method is extended to the 3D environment using model averaging and input transformation technique to produce a multi-mode PWM representation of the system. Considering the constraints imposed by model averaging, proper controllers are designed and implemented to compensate for the tip positioning errors. To decrease the number of needle rotations and consequently decrease the tissue trauma, the switching controller is replaced by a sliding mode controller. This method considers two surfaces and finds the required rotation angle to compensate the tip defection error in 3D space. The proposed method is then improved by using an adaptive structure in which the sliding surfaces are rotated. Since ultrasound images can only provide measurements of the needle tip position and no information about the needle tip orientation can be retrieved from ultrasound images, model-based state observers are designed to overcome the measurement limitations and used in a feedback control scheme. The controllers are designed to meet the observer requirements and guarantee the stability of the system. As another step in compensating needle tip placement errors, we propose an extension to kinematic unicycle/bicycle model, which has been widely used for planning and control purposes. The goal of this modeling is to add new parameters to the existing model to account for tissue motion.

Preface

In the following, all contents of this thesis published in peer-reviewed conferences and journals are listed. The observer review presented in Chapter 1 is part of the work published in *Automatisierungstechnik, Methoden und Anwendungen der Steuerungs-, Regelungs- und Informationstechnik (AT - Automation Technology: Methods and Applications of Control, Regulation, and Information Technology)* [1]. The method proposed in Chapter 2 is published in *IEEE Robotics and Automation Letters* [2]. The contents of Chapter 3 and 4 are published in *Journal of Medical Robotics Research* [3] and *Control Engineering Practice* [4], respectively. The contents of Chapter 5 were presented at *2016 IEEE/ASME International Conference on Advanced Intelligent Mechatronics* [5] and the contents of Appendix B are presented at *2015 IEEE/RSJ International Conference on Intelligent Robots and Systems* [6]. The contents of Chapter 6 are submitted to *IEEE Transaction on Control Systems Technology*. In all of the above listed publications, Bita Fallahi is the first author. The literature review provided in Section 1.2 is the author's own work. All described devices and algorithms that are the work of others are acknowledged where appropriate.

To my parents.

Acknowledgements

I would like to express my sincerest gratitude to my supervisor Dr. Mahdi Tavakoli for the continuous support of my Ph.D. study and research, for his patience, motivation, immense knowledge, and for giving me the opportunity to learn about myself and different aspects of life. Thank you also to my co-supervisor, Dr. Ron Sloboda for the expert advice, support, suggestions, and constructive feedback on my work and writing. I would also like to thank Dr. Carlos Rossa for his great guidance and thoughtful comments, which helped to improve my work and manuscripts. Thank you to Dr. Nawaid Usmani for his continuous support and providing expert advice on the surgical aspects. Thanks also to my peers Jay Carriere, Mohsen Khadem, Thomas Lehmann, and Michael Waine for the excellent teamwork and helping me in different situations. I would also like to thank all the members of the Telerobotic and Biorobotic Systems Group for a great time spending together in a friendly work atmosphere, and the fun social events and activities. Furthermore, thank you also to Dr. Tongwen Chen, the member of my supervisory committee, and all other professors on my candidacy and final thesis examination, who served as examiners. Finally, my deep and sincere gratitude to my family for their continuous love, help and support. The research presented in this thesis was supported by the Canada Foundation for Innovation (CFI), the Alberta Innovation and Advanced Education Ministry, the Natural Sciences and Engineering Research Council (NSERC) of Canada, the Canadian Institutes of Health Research (CIHR), the Alberta Innovates - Health Solutions (AIHS) and by a University of Alberta startup grant.

Contents

List of Tables

List of Figures

Chapter 1

Introduction

Steerable needles have been widely used in minimally invasive procedures such as brachytherapy, biopsy, and neurosurgery. In such methods, flexible beveled-tip needles are inserted into human tissue for diagnosis, treatment, or sample removal. During these procedures, imaging modalities such as ultrasound, X-ray, and fluoroscopy are used to monitor the organs and the needle's position. The efficiency of these methods is highly dependent on accurate control and positioning of the needle tip since poor needle placement can cause undesirable side effects on neighboring tissues or organs. However, due to the tissue deformation, needle deflection and limitations in controlling the needle from outside the body, accurate needle tip placement turns into a challenging problem.

1.1 Prostate Brachytherapy

Prostate cancer is recognized as the second frequent diagnosed cancer in men around the world with an estimation of 1.1 million new cases to have occurred in 2012 [7]. Prostate brachytherapy under ultrasound guidance is a treatment method for early-stage cancers. This method is a type of radiotherapy, in which the radiations are delivered internally by implanting radioactive seeds in or around the prostate gland. The seed implantation is preceded by taking axial images to find the margins of the prostate and the target volume. Using these images the distribution of the seeds is pre-planned to have the desired dose distribution. The desired locations of the seeds are registered with respect to a template grid, and as a result, it is desired to insert the needle to the final depth on a straight line. Several needles loaded with rows of seeds are manually inserted through a 5 mm template grid. After reaching the final depth, each needle is retracted, and the seeds are pushed out using a stylet. During the insertion, the needles are visually tracked using a transrectal ultrasound probe (TRUS) to help the needle guidance.

In brachytherapy, implanting the seeds at the pre-planned location is of great importance as it determines the defined dosage of radiation to the cancerous tissue. Errors in seed positioning reduce the efficiency of the method as instead of cancerous tissue, the radiations

are imposed on the healthy tissue. As mentioned before, the assumption during the pre-planning is to insert the needle on a straight trajectory. However, using beveled-tip needles, due to the asymmetry of the forces at the needle tip, the needle bends in the same direction of the bevel. This feature of the beveled-tip needles enables needle steering by rotating the needle and changing the bevel orientation. In fact, this technique is commonly used in prostate brachytherapy. The needle deflection should be controlled by an expert surgeon to reach the desired depth and be close to a straight needle at the final insertion depth. The absolute seed positioning error obtained from manual insertions by experienced practitioners is approximately ± 5 mm [8].

The accuracy of these procedures can be enhanced using intelligent assistant robots to compensate for the targeting errors caused by needle deflection and tissue deformation. The first step in semi-automating the insertion procedure is to have physical models that relate the needle/tissue interaction to various inputs such as needle insertion velocity, axial rotation, needle base lateral position and needle base force/torque. Such physical modeling of needle-tissue interaction provides a means to estimate needle deflection and provides an opportunity to minimize needle placement errors through feedback control.

For safety reasons, it is always desired to involve the clinician in the loop. In robot-assisted procedures we envision, the steering action is divided between the robot and the clinician to hit the right balance between improving the targeting accuracy of insertions and the treatment safety issues. Consequently, in robot-assisted procedures, some of the inputs such as needle rotations are adjusted automatically while the other inputs such as needle insertion velocity and the initial insertion points are controlled by the surgeon.

1.2 Various Problems in Needle Insertion Research

1.2.1 Modeling Needle Deflection

Designing intelligent assistant systems to steer the needle from outside the body demands having models to represent the needle/tissue interaction and estimate the needle deflection during the insertion. Several needle/tissue interaction models have been developed which include finite element modeling, energy-based methods, flexible beam modeling and kinematic models. DiMaio and Salcudean [9] have proposed a model using the 2D Finite Element

2

Method (FEM) for quantifying the needle/tissue interaction and deformation. Alterovitz *et al.* [10] developed an interactive simulation of needle insertion and radioactive seed placements in soft tissues. Based on these, other models are developed considering the needle flexibility [11]. Later Goksel *et al.* extended this model into 3D [12]. Using the FEM model for the tissue, Dehghan *et al.* developed a planning method for rigid needles [13].

Other research groups have employed beam theories to develop mechanics-based models. Yan *et al.* proposed a spring-beam-damper model which, unlike the FEM method, employs an unconstrained model for analysis and derivation of the dynamic equations [14]. This is improved by taking the tissue inhomogeneity into account using depth varying parameters to calculate the spring and damper effects [15]. Chentanez *et al.* modeled the needle in 3D space as a 1D rod using Cosserat theory [16]. Goksel *et al.* developed three different models to simulate the needle deformations and compared their efficiency and accuracy [17]. Misra *et al.* presented an energy-based method to predict needle behavior based on fundamental mechanical and geometrical properties of the needle and tissue [18]. Using Rayleigh-Ritz method, Misra *et al.* developed a mechanics-based model for needles undergoing multiple bends [19]. Ignoring the tissue properties, Webster *et al.* proposed a kinematic nonholonomic model for the needle using unicycle equations [20]. In this model, the needle is assumed to move on a curved path with constant curvature (circle). For each needle-tissue combination, the path curvature is found using curve fitting methods. This model is advantageous as it provides a simple, intuitive model for analysis that is efficient for numerical computations. These models provide a means for predicting the needle tip position and model the needle/tissue interaction.

1.2.2 Path and Motion Planning

Considering the motion of the needle, the nonholonomic constraints on the needle kinematics limit the steerability of the needle. The desired needle path, however, depends on the application. In biopsy, it is desired to reach a constant final deflection whereas in brachytherapy the needle should follow a straight path. In case of having obstacles on the needle path (such as bones or nerves), the needle should follow a pre-planned curved path. To find a feasible path, there have been different path planning methods proposed in the literature. Hamze *et al.* proposed an optimization-based pre-operative algorithm to find an optimal

needle trajectory, which accounts for needle flexibility and tissue motion. Their method employs a parameterized finite element formulation to model the deformations caused by needle/tissue interaction [21]. Girbacia *et al.* used genetic algorithms in brachytherapy to find a trajectory to the target point while avoiding any intersections with vital organs [22]. Considering different initial insertion angles, Tsumura *et al.* proposed a planning method for finding the optimal path to minimize the deflection [23]. Alterovitz *et al.* proposed a planning algorithm in 2D space with obstacles using 2D finite element model to find the tissue deformation and compute the optimal value for the initial insertion angle, position and bevel orientation [24].

In addition to the path planning algorithms, there are different motion planning methods, which not only calculate the feasible path, but also find the necessary actions to steer the needle on this desired path. Using beveled-tip needles, the path traveled by the needle depends on the orientation of the bevel, which changes by needle axial rotations and provides a way for steering the needle on different paths.

Authors in [25, 26] formulated the motion planning problem as a Markov decision process to find an optimal discrete control sequence in 2D space using dynamic programming. Park *et al.* considered the planning problem in 3D space for a stiff tissue with no obstacles using the propagation of needle position probability [27]. Authors in [28] used an ultrasound-based deflection predictor and developed a 2D semi-automated needle steering strategy. In this approach, the surgeon is in charge of needle insertion to ensure the safety of the operation, while the needle tip bevel location is robotically controlled to minimize the targeting error. Xu *et al.* and Duindam *et al.* presented motion planners for 3D environment with obstacles using rapidly exploring random tree (RRT) searching method [29, 30].

Duty cycle spinning is a method proposed by Minhas *et al.*, which is based on simultaneous insertion and rotation of the needle. The duty cycle, which determines the time intervals of pure insertion and simultaneous insertion and rotation, is found as a function of the desired path curvature. It is shown that by duty cycle spinning of the needle, paths with different curvatures can be achieved [31]. Many of the motion planning algorithms in the literature are combined with the duty cycle spinning for steering the needle on the desired path. Majewiez *et al.* presented two methods for duty cycle spinning to overcome hardware limitations such as cable wind-up [32]. To have paths with variable curvature, this

method is combined with 3D planners in [33] for environments with obstacles. Authors in [34, 35, 36] employed RRT-based methods to perform real-time re-planning and combined it with duty cycle spinning to steer the needle to the desired position. Sun *et al.* proposed an LQR-based planning method and used it with duty cycle spinning [37]. Li *et al.* used a kinematic model of the needle and a potential field-based planning method along with the duty cycle spinning [38]. The duty-cycle spinning method requires the maximum needle path curvature which may vary during the insertions due to tissue inhomogeneity. The steering method presented in [33] uses the needle path curvature as a constant model parameter to perform any necessary rotations to move the needle toward the target point. To compensate the effect of tissue inhomogeneity on needle path curvature Moreira *et al.* integrate online curvature estimation to 3D planners and duty-cycle spinning [39]. Reed *et al.* combined a 2D planner with a sequence of image-guided needle rotations which compensate the out of plane motions of the needle [40]. During the insertion in these methods, if errors occur due to tissue non-homogeneity or uncertainties, re-planning is required to find a new desired path to compensate for the errors.

1.2.3   Needle Steering Control

Viewing the needle insertion system as a control system, the control objective can either be regulation or tracking. In regulation, the goal is to reach the desired deflection, regardless of the path traveled. In tracking, the goal is to control the needle to travel on a straight path by minimizing needle bending or travel on an appropriate curved path that specifies the desired deflection at every depth assuming the path satisfies the nonholonomic constraints, which can be used to avoid obstacles. To this end, two control inputs affecting the system are the insertion velocity and the needle axial rotations. The axial rotations change the bevel orientation causing the needle to travel on different paths in 3D space. In this case, the steering problem can be viewed as a feedback control loop shown in Fig.1.1.

To keep the needle moving as straight as possible, Abolhassani *et al.* has proposed a method to perform the axial rotations when the needle deflection reaches some predefined threshold [41]. In this method, the deflection and the rotation locations are calculated based on the force data and needle's model (flexible beam model) which may encounter uncertainties.
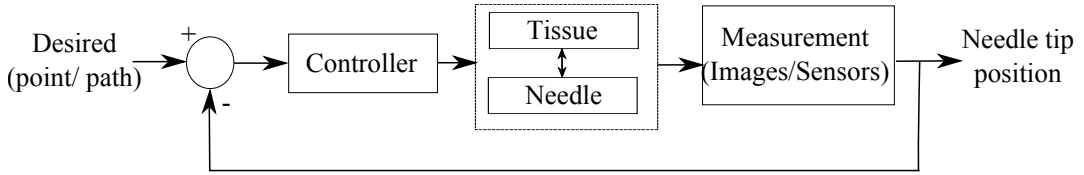
Figure 1.1: Control loop for needle steering

From a control perspective, in [42], the controllability of the needle in soft tissue is studied using a dynamic model. Khadem *et al.* proposed a mechanics-based model of needle steering and developed a nonlinear model predictive controller (MPC) for 2D needle steering using iterative optimization of the predictions [43]. Authors in [44] proposed a stochastic optimal steering method using Markov chain approach for 2D needle steering in the presence of obstacles, uncertainty and tissue motion. Abayazid *et al.* combined planning and control methods and used the geometric and trigonometric relations between the needle's current position and the target in a feedback loop [45]. In some of these algorithms, the exact knowledge of system parameters such as the needle's path curvature or its maximum value is needed. In [46], a sliding mode controller is presented which is based on the 3D unicycle model proposed in [20]. In this method, a 5DOF magnetic tracking sensor is used which is combined with a with Kalman filter to provide the full information about the needle tip position and orientation. Measuring the orientation requires utilizing a sensor such as a needle-mounted electromagnetic tracking sensor, which itself suffers from sterilization and size issues. Since suitable sensors are not accessible, state observers can be employed to estimate the needle tip orientation using the measured needle tip position [47]. Besides, if orientation observers or estimators are going to be used, the overall stability of the observer/controller loop should be studied, which is not a trivial task. Motaharifar *et al.* proposed an adaptive output feedback controller to deal with parameter uncertainties. In this method, a nonlinear high gain observer is designed to estimate the non-measurable system states to be used in the adaptation law. [48].

There have been many different measurement methods utilized for planning and steering such as acoustic radiation force impulse imaging method (ARFI) to find the needle curvature [49], fiber Bragg grating sensors [50], and electromagnetic tracking [46, 51] for needle tip position measurement. In [49], the on-line and off-line curvature estimation method are incorporated using ARFI imaging technique for finding the value of variable curvature. This

steering algorithm is an optimization-based method that uses the updated amount of curvature to improve the targeting error.

1.3 Observers in Medical Robotics

The application of the robotics in medical procedures is very task dependent. According to the application, observers can be used as a replacement for sensors or can be used in situations where sensors are not applicable. In rehabilitation applications replacing sensors with observers provides a way to reduce the cost and the weight of the devices. In these applications where the rehabilitation devices (such as exoskeleton devices) are used by the patient for a long duration, reducing the cost and the weight of the devices is very advantageous. Moreover, due to the limited space in some devices such as hand exoskeleton [52], force sensors should be replaced by other measurement or estimation methods. In MIS procedures, where the fine tools are inserted into the body through small incisions, placing measurement devices at the tip of the surgical tools to be inserted into the body is not practical. Besides, one of the important issues in surgical procedures is the sterilization of the equipment, as well as the sensors. Replacing sensors with observers relaxes this issue. There are also different challenges in designing and using the observers. In medical procedures, safety is a very important issue, which should also be considered in designing observers. The performance of the observer (convergence to the real values) should be guaranteed to provide the surgeon/assistant robot with realistic values to ensure the safety of the patient and the efficiency of the method. Especially, when the observers are used to control the assistant robots, the stability of the observer/controller should be guaranteed. Besides, effective observers require a good model describing the system's behavior. In some applications, finding such a model is not a trivial task.

1.3.1 Force Estimation

Rigid Tool: When it comes to human-robot interaction, using force control methods become crucial for providing a safe and effective environment for the human and prevent any excessive damage or trauma to patient's body [53]. In robot-assisted surgeries or telesurgeries, the robot is in direct contact with the soft tissue. In this case, it is important to detect

the contact and measure the force applied by the robot on the soft tissue. In such cases, force control strategies provide better solutions for controlling the robotic manipulators [54]. In rehabilitation tasks, in which the goal is to rehabilitate the musculoskeletal system, the robot is also in interaction with the patient. There have been different types of wearable exoskeleton robots developed for rehabilitation of upper and lower limbs [55], spine [56], knee [57], hand [58], etc. These robots are designed to improve the functionality of body joints and limbs after stroke or other disability events [59, 60, 61]. These devices demonstrate another example of direct interaction between a robot and human, in which measuring the interaction forces is imperative. In both of aforementioned applications, using sensor-less methods would be beneficial to decrease the costs and increase the applicability of the designed devices; however, the difficulty arises in terms of designing observers and estimators and analysis of the effects of the estimation error on combined observer/control strategies, and guaranteeing stability, safety and efficiency.

Due to the nonlinear dynamics of rigid robots, nonlinear disturbance observer (NDOB) are used. The main task of a disturbance observer (DOB) is to estimate the disturbances and modelling uncertainties [62]. To design an NDOB, the robot's unmodeled dynamics are considered as additive uncertainties and all these uncertainties and external forces are lumped into one disturbance vector. In the conventional NDOB, it is assumed that the joint accelerations are measured. In the case that no acceleration sensors are available, an advanced NDOB [63] provides a suitable structure. Kalman filters also provide another approach for estimating the interaction forces. Mitsantisuk et al. use a Kalman-filter based state observer for estimating the hand and wrist forces of the patient in robot-assisted rehabilitation [64]. Pehlivan et al. employ a Kalman filter and Lyapunov analysis to provide a stable and fast force estimation in upper limb rehabilitation [65]. Fakoorian et al. use extended Kalman filter as well as unscented Kalman filter (UKF) for estimating robot states and the ground reaction forces in a prosthetic leg [66]. Mitsantisuk et al. propose a method that takes the advantage of both DOB and Kalman filter [67].

Flexible Tool: As stated before, in order to increase the efficiency of needle insertion procedures, accurate steering algorithms are required. Since the needle bends as a result of forces acting on the needle, any information about the needle/tissue interaction will be
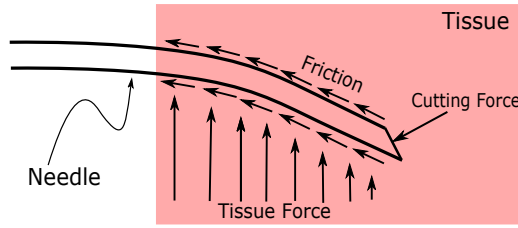
Figure 1.2: Needle/tissue interaction forces. The cutting force is at the needle tip, friction forces act along the needle shaft and tissue forces depends on tissue stiffness.

helpful for steering the needle. The needle/tissue interaction forces are composed of cutting, stiffness and friction forces [68] as shown in Fig. 1.2. The cutting force is the force at the needle tip causing the needle to slice the tissue and move through it, which is a constant value. The friction force acts along the needle shaft during the insertion and the stiffness force depends on the tissue properties. Since there are no clinically approved needle mounted sensors available, it is not possible to measure the needle/tissue interaction forces. However, a needle-based-mounted force sensor provides a practical way for measuring the total forces acting on the needle at its base.

The force estimation methods in needle insertion procedures are mainly the techniques described in the previously. In these methods, the force data is found using the deflection information and the forces measured at needle base. Asadian et al. model the interaction forces base on LuGre [69] model and estimate the parameters online using multiple EKFs [70]. Fukushima et al. employ a DOB and the recursive least squares (RLS) technique to find the tip and friction force acting on the needle [71]. Maghsoudi et al. propose two methods for estimating the forces; a DOB and a model-based method [72]. The two methods are then compared in a needle insertion control loop and the results show the robustness of DOB to uncertainties. Having the total force acting on the needle, Suzuki et al. combine a reaction force observer [73] with the RLS method to find the stiffness force of the tissue in a stiffness assessment task in liver teleoperation biopsy [74].

1.3.2 Pose and Motion Estimation

Physiological Motion: To avoid inaccuracy during surgical interventions, it is desired to remove any unwanted motions or disturbances. Even if the patient is still, there may be physiological organ motion. There are two types of physiological motions: periodic mo-

tion such as the heartbeat and respiration, and the non-periodic motions. The examples of non-periodic motions, which are very relevant in surgical interventions, are the organ motion after opening the body such as brain [75] and abdominal cavity during MIS [76]. The two main sources of periodic physiological motions are the respiration and the heartbeat. Respiration causes low-frequency, large-amplitude cyclic motions while heartbeat produces high-frequency, small-amplitude semi-periodic motion in the heart.

There have been different methods proposed in the literature for estimating the heart motion using images. Sauv et al. consider two approaches based on landmark and texture tracking for 3D heart surface tracking [77]. Richa et al. employ a thin-plate spline warping model (TPS) for 3D tracking of beating heart using endoscopic images [78]. Yang et al. propose a robust 3D tracking scheme based on two methods [79]. To predict the heart motion, there are non-model based methods proposed in the literature which use a long embedding vector of past measurements of the heart motion and predict the motion by finding a previous embedding vector similar to the current vector [80].

However, these methods lack the required robustness and accuracy, since they are only based on the images and no information about the dynamics of the heart motion and the respiratory system are taken into account. Also, imaging methods fail to predict the motion in case of any occlusions such as surgical instrument, blood, and smoke. Another issue in retrieving the heart motion only based on images is data acquisition delay. In this case, predictive strategies can be used to compensate for the data acquisition and processing delay.

According to the nature of the physiological motion, a quasi-periodic model can be used to estimate the heart and respiratory motion. The quasi-periodic motion is defined as a time-varying Fourier series, for which the coefficients can be estimated using different methods [81, 82]. Extended Kalman filter (EKF) is an estimation method in which the current measurements and the mathematical model are simultaneously used to estimate the unknown variables, which also overcomes the low update rate of the images and can be used to predict the motion in case of any occlusions. Bowthorpe and Tavakoli have considered the quasi-periodic model for the heart motion and found the coefficients using the Extended Kalman filter [83]. Similarly, in the work done by Yuen et al., the heart motion is estimated and is used to predict the future heart motion [84]. To model both the breathing and heart

beat motions, Richa et al. [85] and Yang et al. [86] propose the summation of two Fourier series and use Extended Kalman filtering method for estimating the parameters.

Tool Pose: In robotic-assisted surgeries, where the surgical tool is manipulated by a robotic system, the position and orientation of the surgical tool are valuable information for controlling the robotic manipulator. Some of that information can be obtained from imaging modalities. Ultrasound imaging is a cost-effective and widely used imaging modality, which has been employed in many applications. There have been different methods proposed in the literature for localization (position estimation) of the surgical instruments and needles inside the body using ultrasound images. Different issues in needle steering can be found in the work done by Rossa et al. [87]. According to needle kinematics [47], the three fixed angles of roll, yaw, and pitch, representing the needle tip orientation, are highly involved in the system motion and having knowledge of them is very beneficial for controlling the needle tip position. However, due to the small diameter of the needle and the low resolution of the ultrasound images, it is not possible to measure the needle tip orientation from ultrasound images. This motivates the idea of designing state observers for estimating the needle tip orientation using the needle tip position obtained from ultrasound images. There are a few researches on estimating the needle tip orientation using observation methods. In the sliding mode controller proposed by Rucker et al., the needle tip orientation is required for calculation of the control action [46]. In this work, a 5 DOF magnetic tracking sensor is used which is combined with a Kalman filter to find the full information about the needle tip position and orientation. This may work in a lab setting but is not clinically feasible due to sterilization issues.

1.4 Challenges and Objectives of This Work

In this work, the needle steering problem is viewed as a feedback control problem to compensate for needle positioning errors in needle insertion procedures. In this case, the control objective can either be regulation or tracking. In regulation, the goal is to control the needle to travel on an appropriate curved path to reach a desired and feasible deflection at a given final depth. In tracking, the goal is to control the needle to travel on a curved path that specifies the desired deflection at every depth assuming the path is feasible. The feedback

loop is completed by feeding the controller with the needle tip position obtained from ultrasound images. In this work, the needle tip position error, which is the difference between the desired deflection and the actual tip deflection is used to evaluate the performance of the proposed methods. As mentioned before, the absolute positioning accuracy in manual brachytherapy seed placements performed by expert surgeons is ± 5 mm. To introduce improvements to needle tip positioning, we consider the maximum acceptable tip error to be ± 2 mm, which is the size of the smallest lesion detectable in ultrasound images [88].

Needle defection at each depth of insertion can be projected on two planes, representing in-plane and out-of-plane motion. From this point of view, the needle represents an under-actuated system as there are two objectives; controlling the in-plane and out-of-plane defections while there is only one control input, the axial needle rotations. Besides, due to the bevel at the needle tip, the needle bends during the insertion, which shows that the system does not have any equilibrium points. These issues along with some nonholonomic constraints imposed on the needle kinematics, parameter uncertainties, and equation singularities, turn the needle steering procedure into a challenging control problem.

Moreover, it is important to access a suitable model for the system which can be used in controller design and real-time implementations. In this work, we use the kinematic unicycle model for the needle [20]. The advantage of this model is its simplicity as it only represents the kinematics of the needle with certain assumptions and ignores the effects of the needle/tissue interaction forces. However, this simplicity may be limiting in certain situations, some of which are considered in this work.

This thesis is divided into two main parts. Chapters 2, 3, and 4 are devoted to the design and implementation of controllers for 2D and 3D needle steering. In Chapters 5, and 6 observation methods and observer-based control strategies are presented. The remainder of this chapter is devoted to introducing the kinematic bicycle model for the needle and the experimental setup which are used throughout the next chapters.

1.5 Experimental Setup

To verify the accuracy of the proposed methods, the experimental setup shown in Fig. 1.3 is used. The system consists of a carriage actuated by a DC motor through a belt and pul-

ley mechanism which performs the translational motion of the needle. Another DC motor is assembled on the translational stage to which the needle base is attached, and performs the needle axial rotations. This motor is equipped with an encoder, and its position is controlled using a PID controller. To track needle tip, 2D transverse ultrasound images are used (SonixTouch, Ultrasonix, BC, Canada), which provide information about the needle position. In clinical manual insertions, the surgeon uses the ultrasound images visually to track the needle. Here this visual feedback is combined with image processing and Kalman filtering technique to calculate the needle tip deflection from partial observations of the needle [89]. Since the ultrasound images are the only source providing us with the needle tip position, this information should be accepted as the true measurement value. However, in order to find the tip position, the needle tip should be visible in the images. Issues about the required image quality and different artifacts affecting the needle position measurement are discussed in [89], which is out of the scope of this work. Here, the information obtained from ultrasound images is considered as the true value of the needle tip deflection, which provides numerical measurements to be used by the controller. The needle tip deflection is fed back to the controller and is updated every 0.05 sec. The ultrasound probe is attached to a translational platform to track the needle tip.

1.6 An Introduction to Unicycle/Bicycle Model

Among several needle-tissue interaction models, the kinematic nonholonomic model has been proposed as an empirical parameter-identifiable model that can estimate needle deflection based only on limited knowledge about tissue-needle interaction. This model describes the kinematics of the needle tip based on constraints imposed by tissue and has been widely used for path planning and needle steering [27, 46, 20]. The main assumption made in this model is that the tissue is stiff relative to the needle. Inserting the needle into stiff tissue causes negligible deformation in tissue as the needle bends. Thus, it is assumed that the needle tip moves on a circular path with a constant curvature. Approximating the path followed by the needle tip with a circle makes the path planning procedure simple as the radius and center of the circular path can be analytically derived. However, if the tissue is not stiff
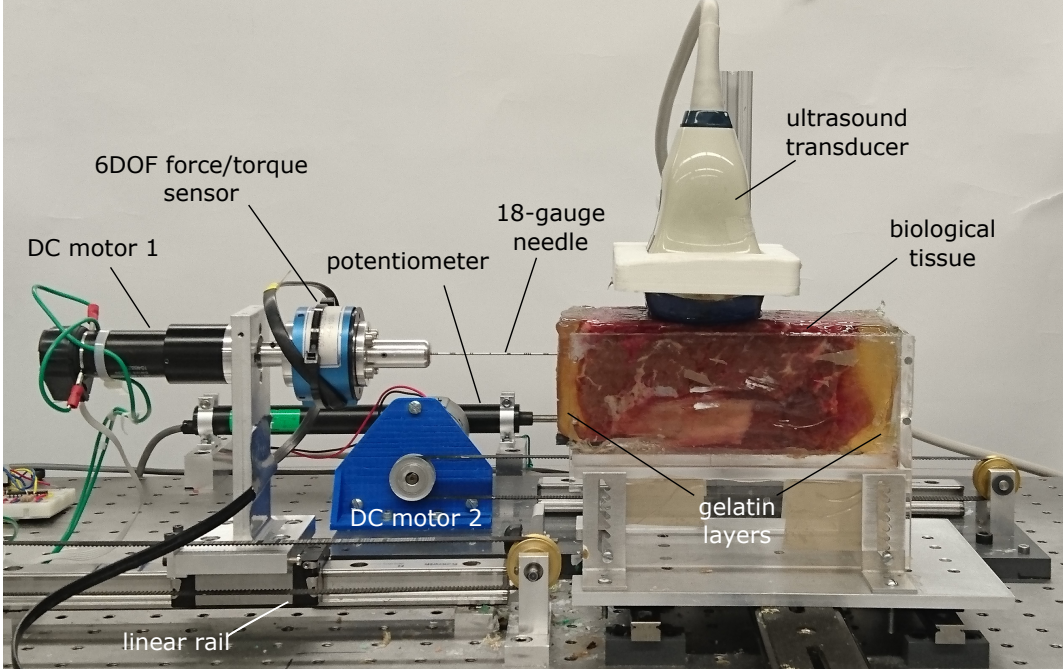
Figure 1.3: Experimental setup used to perform needle insertion. The setup provides translational and rotational motion of the needle. An ultrasound machine (SonixTouch, Ultrasonix, BC, Canada) is used to track the needle tip position. A 6DOF force/torque sensor is attached to the needle base which is not used in this work.

relative to the needle, as the needle bends during insertion the tissue is compressed and in turn displaces the needle tip from a circle, thus producing non-circular paths [90, 18].

A beveled-tip needle inserted into soft tissue is usually driven with two inputs, namely longitudinal insertion, and axial rotation. During insertion, as a result of tissue reaction forces, the needle bends in 3D space. In [20], it is shown that the needle tip posture i.e., position and orientation, resembles the posture of a bicycle moving on a circular planar path with the insertion velocity acting as the riding speed.

Fig. 1.4 illustrates this model of a bevel tip needle with the associated bicycle wheels. In this figure, frames $\{B\}$ and $\{C\}$ represent the moving body frames attached to the wheels. The parameters ℓ_1 and ℓ_2 denote the distance between the two wheels and the distance between the back wheel and the needle tip, respectively. Using the procedure provided in Appendix A the kinematic model for the needle is found as

$$\dot{g}_{ab}(t) = g_{ab}(t)\left(v\begin{bmatrix} e_3 \\ ke_1 \end{bmatrix} + u\begin{bmatrix} 0 \\ e_3 \end{bmatrix}\right) \tag{1.1}$$
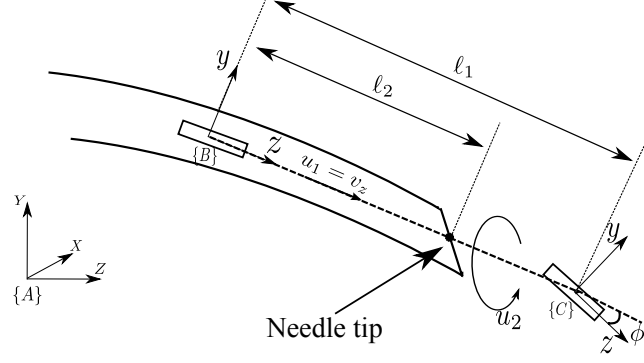
Figure 1.4: Bicycle model of a bevel tip needle. The frames $\{C\}$ and $\{B\}$ are attached to front and back wheels.

In (1.1), v and u denote the insertion velocity and the needle axial rotational velocity, respectively, and g_{ab} is given by $g_{ab} = \begin{bmatrix} R_{ab} & p_{ab} \\ 0^T & 1 \end{bmatrix}$ with $p_{ab} = [x,\ y,\ z\ ]^T$ and R_{ab} being the position and orientation of the moving frame $\{B\}$ with respect to the fixed frame $\{A\}$, respectively as shown in Fig. 1.5, and $e_i, i = 1, 2, 3$, represent the standard basis vectors in $\mathbb{R}^3$ and k is the needle path curvature. The insertion velocity v has minimal effect on the tip path and is therefore assumed to be constant. A unicycle moving on a circular path with constant curvature k has also exactly the same kinematic equations. Expanding (1.1), the coordinate free needle equations can be re-written as

$$\dot{p} = R \begin{bmatrix} 0 \\ 0 \\ v \end{bmatrix} \tag{1.2a}$$

$$\dot{R} = R \begin{bmatrix} 0 & -u & 0 \\ u & 0 & -kv \\ 0 & kv & 0 \end{bmatrix} \tag{1.2b}$$

Using the vector $\mathbf{q} = \begin{bmatrix} x, & y, & z, & \alpha, & \beta, & \gamma \end{bmatrix}$ as the generalized coordinates which is well defined on

$$\mathcal{U} = \{\mathbf{q} \in \mathbb{R}^6 : \alpha, \gamma \in \mathbb{R}, \beta \in [-\pi/2, \pi/2]\} \tag{1.3}$$
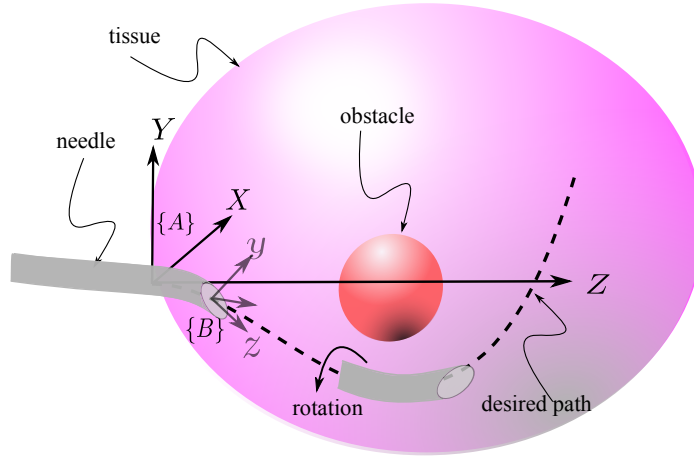
Figure 1.5: The needle in 3D space, desired path and obstacle. Frame $\{A\}$ is the fixed frame and frame $\{B\}$ attached to the needle tip is the moving frame.

the needle kinematics (1.1) can be presented as: [47]

$$\dot{x} = v \sin \beta \qquad (1.4a)$$

$$\dot{y} = -v \cos \beta \sin \alpha \qquad (1.4b)$$

$$\dot{z} = v \cos \alpha \cos \beta \qquad (1.4c)$$

$$\dot{\alpha} = kv \cos \gamma \sec \beta \qquad (1.4d)$$

$$\dot{\beta} = kv \sin \gamma \qquad (1.4e)$$

$$\dot{\gamma} = -kv \cos \gamma \tan \beta + u \qquad (1.4f)$$

Here, $\begin{bmatrix} x & y & z \end{bmatrix}^T$ represents the position of the origin of the moving frame $\{B\}$ with respect to the fixed frame $\{A\}$. The angles α, β and γ are the yaw, pitch, roll angles, representing the orientation of the frame $\{B\}$ with respect to frame $\{A\}$. Using these three angles, the orientation of the moving frame can be obtained by three successive rotations about the axes of the fixed frame. Since the rotations are performed about the fixed axes, the corresponding rotation matrix can be found by pre-multiplying the three basic rotation matrices [91].

Chapter 2

Sliding-based Switching Control for Needle Steering

The main purpose of the chapter is to study the feasibility of a simple technique for a regulating problem to steer beveled-tip needles into a target point in soft tissue. The target point is a 2D point which is specified by the desired deflection at the desired insertion depth. To steer the needle to the target point, the proposed algorithm only uses the information from visual feedback, and no information about the needle or tissue parameters is involved in the controller structure. Especially, the exact value of the needle path curvature is used extensively in many other papers as a parameter in their planning or control algorithms. However, this parameter can be variable due to the tissue inhomogeneity. In this chapter, we only require a rough estimate of the curvature. It should be noted that since the value of the curvature is not directly used in the steering algorithm, the algorithm is not sensitive to curvature uncertainties. The parameter tuning process is an advantage as it provides a way to trade off deflection errors with the number of rotations.

2.1   Controller

To analyze the proposed switching controller consider the planar needle motion equations

$$\begin{bmatrix} \dot{z} \\ \dot{y} \\ \dot{\alpha} \end{bmatrix} = \begin{bmatrix} \cos \alpha \\ \sin \alpha \\ k \end{bmatrix} v.$$

Here $(\dot{\times})$ denotes the time derivative and z and y represent the position of the needle tip in the $(y-z)$ plane (the insertion direction is z and the orthogonal direction is y, respectively). $\alpha \in [-\pi/2, \pi/2]$ gives the needle tip angle found as the angle between the z-axis of the moving frame $\{B\}$ attached to the needle tip and the z-axis of the fixed frame $\{A\}$. v is the constant insertion velocity and k denotes the needle path curvature. For a planar motion, k

can be written as $\pm k_0$ with $k_0 > 0$ where $\pm$ determines the orientation of the bevel tip, which specifies the concavity of the needle path curve. The bevel orientation can be changed by rotating the needle by $180°$. Using this equation, the needle is derived with two inputs, the insertion velocity v and the needle axial rotations, which can be used to steer the needle to the target point. In order to reach the desired deflection, one can perform sequences of $180°$ axial rotations. Assuming the axial rotation velocity to be much larger than the insertion velocity, the out of plane motion can be neglected. The needles considered in this work are flexible beveled-tip needles clinically used in prostate brachytherapy. The asymmetric force at the needle tip due to the bevel will cause the needle to bend as it is inserted into the tissue. For clinical reasons (radioactive seed implantation on a straight line), it is desired to steer the needle tip into a target point. In this chapter, the target point in the plane is determined either by a straight line or by a desired deflection at a desired depth. In both cases, the needle targeting error equals the needle tip deflection when the needle reaches the specified depth. As said above, the error is defined as the difference between the desired deflection and the actual deflection of the needle tip as measured from US images.

In the planar case, since there are only two options available for the bevel orientation, the sequence of axial rotations is determined by switching decisions between the two modes of the system, i.e. mode 1 with $k > 0$ and mode 2 with $k < 0$. Here, we will use sliding mode control to find the switching instants that steer the needle toward the desired position. Let the sliding surface be

$$S = b\dot{e}_y + ce_y \tag{2.1}$$

in which $e_y = y - y_d$ is the deflection error, y is the needle tip deflection and y_d is the desired deflection. For a constant desired deflection y_d, $\dot{y}_d$ and $\ddot{y}_d$ equal zero and the sliding surface simplifies to

$$S = b\dot{y} + ce_y \tag{2.2}$$

Starting from zero initial condition, i.e. $y = 0$, $y_d = 0$ is equivalent to moving the needle on a straight path. In the next section, we will show that by proper switching between the two system modes, the stability of the closed-loop system and convergence of the error can be guaranteed.

2.2 Stability

2.2.1 Lyapunov Stability

To analyze the stability of the closed-loop system, consider the following Lyapunov function

$$V = \frac{1}{2}S^2 \tag{2.3}$$

For this positive valued function V, if $\dot{V} < 0$, V and hence $|S|$ will be decreasing. Assuming that $|S|$ is initially bounded and it is decreasing, then S will remain bounded. If the switching is performed such that

$$\dot{V} = S\dot{S} < -\eta|S| \tag{2.4}$$

for some $\eta > 0$, then S approaches zero [92]. This condition can be written as

$$\begin{cases} \dot{S} > \eta, & \text{if } S < 0. \\ \dot{S} < -\eta, & \text{if } S > 0. \end{cases} \tag{2.5}$$

Taking the time derivative of (2.2), we have

$$\dot{S} = b\ddot{y} + c\dot{y} \tag{2.6}$$

The parameters b and c of the sliding surface need to be chosen to meet (2.4).

Using (2.1), (2.6) can be written as

$$\dot{S} = v\{\pm bk_0v\cos\alpha + c\sin\alpha\} \tag{2.7}$$

since $\alpha \in [-\pi/2, \pi/2]$, the first term in (2.7) is strictly positive and strictly negative for modes 1 and 2, respectively. Assuming the angle α is limited to $|\alpha| \leq \alpha^*$ for some $0 < \alpha^* < \pi/4$, choosing the parameters b and c such that

$$\frac{bk_0v}{c} > \tan\alpha^* \tag{2.8}$$

ensures that $\dot{S} > \eta$ for mode 1 and $\dot{S} < -\eta$ for mode 2 which is appropriate when $S > 0$ and $S < 0$, respectively. In other words, if (2.8) is satisfied and the switching is performed such that when $S > 0$ the system resides in mode 2 ($k < 0$) at which $\dot{S} < -\eta$, and when $S < 0$ the system resides in mode 1 ($k > 0$) at which $\dot{S} > \eta$, (2.5) will be satisfied. So, choosing the sign of the switching surface as the switching rule makes S and consequently the deflection error tend to zero.

It should be noted that how fast the tip deflection error approaches zero, i.e. the error dynamics, are determined by parameters b and c. According to (2.8), since v and k_0 are constant, $\frac{b}{c}$ is lower bounded, which means that the time constant cannot be chosen arbitrarily. This value should be selected as small as possible as it determines the time constant of the error dynamics. For a constant b, a larger value of $\frac{b}{c}$ is equivalent to having a smaller value for c, which reduces the weight of the deflection error in the sliding surface, increasing the time required for the error to approach zero.

In practical applications where the needle is manually inserted into the human body, the surgeon usually performs 1-2 rotations to steer the needle into desired position. This is because surgeons are concerned that too many rotations cause drilling and damaging the tissue and increase trauma to tissue as a result of all the cutting and the heat produced by the needle/tissue friction. This has been previously investigated in the literature [93, 94]. Since our proposed method is based on sliding mode control, it is desired to keep the sliding surface close to zero. This means that rotations are needed whenever the switching surface changes sign. However, this may cause a chattering in the response, which is equivalent to continuous switching (too many needle rotations). To prevent such a phenomenon, the rotation locations are determined based on a hysteresis framework. It should be noted that adding a hard nonlinearity such as hysteresis may have undesirable effects such as instability or limit cycle [95] and its effect should be studied. However, this study is ignored in this work and only the switching thresholds are found as a function of the system parameters.

Using the hysteresis block, the needle rotates when the switching surface reaches some switching threshold (and not as soon as it changes sign) as shown in Table 2.1. In this case, a smaller switching threshold is more desirable for containing the needle deflection errors however it increases the number of rotations. For a large switching threshold, the number of rotations are reduced at the expense of increased needle tip deflection errors.

20

Table 2.1: Selection of the operating mode based on S

Region	System Mode	$sign(\dot{S})$
$S < -S_s$	Mode 1($k > 0$)	+
$-S_s \leq S \leq S_s$	No mode change	+ or -
$S > S_s$	Mode 2 ($k < 0$)	-

2.2.2 Constraints on Switching Threshold

To find a proper value of S_s, for which the value of α remains in the desired range $[-\alpha^*, \alpha^*]$, let $[t_0, T]$ be the time interval between two consequent switches. Since during this interval the system resides in one mode, according to (2.1) and the switching rule, S and α will both be monotonic. Therefore, using (2.2), the variations in S can be written as

$$\Delta S = b(\dot{y}(T) - \dot{y}(t_0)) + c(y(T) - y(t_0)) \tag{2.9}$$

In this equation, $y(T)$ can be found by integrating (2.1), which leads to

$$\alpha(T) = kv(T - t_0) + \alpha(t_0) = \Delta\alpha + \alpha(t_0) \tag{2.10}$$

$$y(T) = \frac{-1}{k}(\cos\alpha(T) - \cos\alpha(t_0)) + y(t_0) \tag{2.11}$$

substituting (2.10) and (2.11) in (2.9), the variations in S can be expressed as a function of $\Delta\alpha$

$$\Delta S = m_1(\cos\Delta\alpha - 1) + m_2\sin\Delta\alpha \tag{2.12}$$

with

$$m_1 = -\frac{c}{k}\cos\alpha(t_0) + bv\sin\alpha(t_0) \tag{2.13}$$

$$m_2 = bv\cos\alpha(t_0) + \frac{c}{k}\sin\alpha(t_0) \tag{2.14}$$

Note that m_1 and m_2 are functions of the initial angle $\alpha(t_0)$ at the beginning of the switching interval. Taking the partial derivative of (2.9) with respect to $\Delta\alpha$, the extremum of ΔS occurs at $\Delta\alpha_m = \tan^{-1}(\frac{m_2}{m_1})$. From (2.8), for any $|\alpha(t_0)| < \alpha^*$, m_2 is positive and the sign of $\Delta\alpha_m$ is determined by the sign of m_1. Using the second derivative test for ΔS, it can

be shown that for $m_1 > 0$, $\Delta\alpha_m$ is positive and makes the function ΔS take its maximum, and for $m_1 < 0$, $\Delta\alpha_m$ is negative and makes the function take its minimum. If the system is in mode 1 ($k > 0$), where $\Delta\alpha > 0$, for $m_1 < 0$, the minimum point $\Delta\alpha_m < 0$ ensures that ΔS will be monotonically increasing with respect to $\Delta\alpha$ and its maximum happens at the upper boundary of $\Delta\alpha$. In order to have $\Delta\alpha_m < 0$ for $k > 0$, the initial condition at the beginning of the switching interval should satisfy

$$\frac{-k_0 bv}{c} < tan\alpha(t_0) < \frac{c}{k_0 bv} \tag{2.15}$$

in which the right hand side is imposed by $m_1 < 0$ and the left hand side is obtained from (2.8). The same analysis can be done for mode 2 ($k < 0$) which leads to

$$-\frac{c}{k_0 bv} < \tan\alpha(t_0) < \frac{k_0 bv}{c} \tag{2.16}$$

However, since $\alpha(t_0)$ at the beginning of each interval is the final result from the previous interval, if

$$\frac{bk_0 v}{c} < 1 \tag{2.17}$$

both (2.15) and (2.16) are satisfied for any $|\alpha(t_0)| < \alpha^*$ and ΔS will be monotonic with respect to $\Delta\alpha$ for both $k > 0$ and $k < 0$ which means that $\max|\Delta S|$ happens at $\max|\Delta\alpha|$. Now in order to find the conditions under which α does not exceed the desired limit α^*, consider the initial condition $\alpha_0 = 0$ and y_0 with $\dot{y}_0 = \ddot{y}_0 = 0$ which leads to $S(0) = ce(0) = c(y(0) - yd)$. At $t = 0$, according to $\text{sign}(S(0))$, the system will be in one of the two system modes causing the value of the sliding surface to change until it reaches one of the switching thresholds S_s or $-S_s$. During this phase α changes from the initial value zero but it is assumed to remain within the desired range. To have such a condition, using (2.12), S should be selected such that

$$S_s \leq m_1(\cos\alpha^* - 1) + m_2 \sin\alpha^* + S(0) \tag{2.18}$$

in which m_1 and m_2 are calculated from (2.13) and (2.14) for $\alpha(t_0) = \alpha_0 = 0$. From this relation it can be seen that the initial condition $|S(0)|$ should be small enough to have $S_s > 0$. This inequality gives the upper bound on switching threshold value which ensures
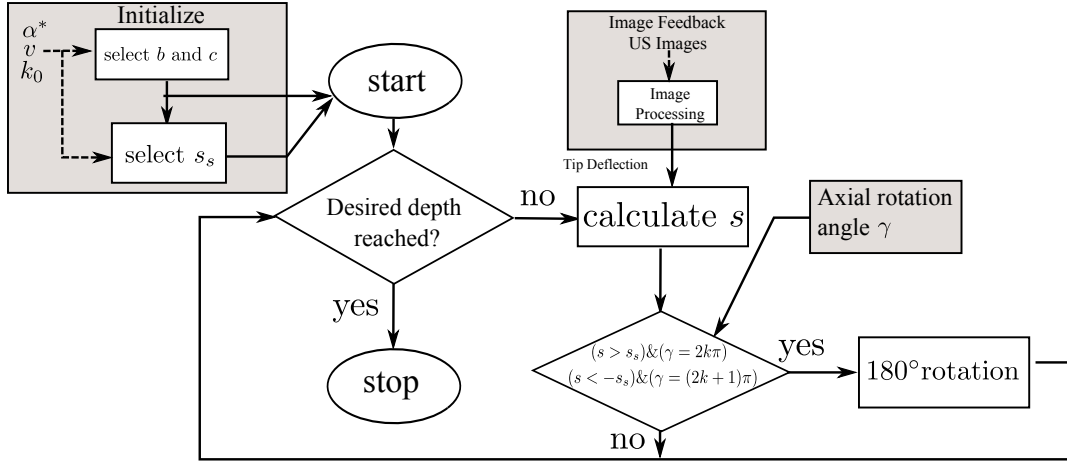
Figure 2.1: The procedure of finding the controller parameters and the steering algorithm

that the needle tip angle will not exceed the predetermined angle α^* to guarantee the stability of the system. The value of α^* can be determined based on the maximum deflection that the needle is allowed to have. Although choosing larger values for α^* is equivalent to letting the needle to bend more, it affects the ratio $\frac{b}{c}$ and the maximum allowable value of S_s.

In (2.18), the initial value $S(0) = ce(0)$ can be used to determine the initial insertion point. For zero initial condition $y_0 = 0$ and zero desired deflection $y_d = 0$ the needle is supposed to move on a straight path. For a nonzero $S(0)$, the needle initial position differs from the desired deflection and the needle is controlled to bend towards the desired deflection.

In summary, selecting a maximum needle tip angle (α^*) and knowing a rough estimate for the curvature (k_0), the other three parameters $(b, c$ and $S_s)$ can be found using (2.8) and (2.18). Since these equations involve inequalities, the value of the curvature can be chosen conservatively such that the inequalities result in worst-case values for algorithm parameters. An estimate of curvature can be obtained from previous insertion data and by adding some safety margin, especially when pre-insertions are undesirable. The proposed algorithm and the procedure for finding the corresponding parameters are shown in Fig. 2.1

2.3 Experiments

In this section, the steering method introduced in this chapter is implemented for needle insertion into phantom and biological tissue using the experimental setup introduced in 1.5.

The needle used to perform insertions is a standard 18-gauge brachytherapy needle (Eckert & Ziegler BEBIG Inc., Oxford, CT, USA) made of stainless steel, with an outer diameter of 1.27 mm, an inner diameter of 1 mm, and a bevel angle of approximately $20°$. In these experiments the switches between two system modes are performed by $180°$ axial rotations.

The phantom tissue used in the experiments is gelatin made by mixing porcine gelatin powder (Sigma-Aldrich Co., ON, Canada) with water at a temperature of $70°C$. Two different weight ratios of gelatin-to-water mixture, 15% and 20%, are considered for these experiments. Here the tissue is considered to have a flat surface, however for non-flat tissue phantoms the translational aspects of the system should be taken into account [96]. To evaluate the performance of the proposed method, five sets of experiments on phantom tissue, with six trials each, and one set of experiments on biological tissue for ten trials are presented. In these experiments, the needle is inserted with a constant velocity and is stopped when the desired depth of 120 mm is reached. To study the effect of the insertion velocity, two different velocities of $v = 2$ mm/sec and $v = 4$ mm/sec are considered for the experiments which are sufficiently smaller than the axial rotation velocity of 5π rad/sec that it can be assumed that the needle remains in plane. In each set of experiments only one parameter is changed so the results can be compared for the specific parameter change. In all experiments, the needle is initially inserted for 5 mm to be detectable by the ultrasound probe and the initial bevel orientation is assigned to be the same so that the needle initially deflects in the same direction. According to (2.2), the algorithm requires the needle tip deflection and its derivative. This signal is filtered by fitting polynomials to the deflection values. In these calculations, the lack of data points at the first moments of the experiment leads to a noisy response that may cause chattering. Consequently, the algorithm is ignored for the first few seconds as far as switching the needle orientation is considered. To find the switching parameters, a conservative estimate of needle curvature $k_0 = 10^{-3}$ 1/mm is used.

In the first two sets of experiments we want the needle to be controlled on a straight path, i.e. $y_d = 0$, with different values of switching thresholds. In addition, since the desired performance is to reach the target point on a straight line, the needle tip angle will be limited to small values; we choose α^* to be 0.03 rad which leads to $S_s < 1.34$. In the first and second set of experiments, we have chosen $S_s = 1$ and $S_s = 0.5$, respectively. The results are displayed in Fig. 2.2 and Fig. 2.3. The number of rotations and the error values are

summarized in Table 2.2. The experiments show that for $S_s = 1$ and $S = 0.5$ in 15%
mixture tissue, the mean absolute error is 0.62 ± 0.39 mm and 0.47 ± 0.31 mm, with the
maximum targeting error of 1.23 mm and 0.91 mm, respectively. As we can see, reducing
the switching threshold from 1 to 0.5 causes a decrease of 0.12 mm in the mean error and an
increase of 3 in the maximum number of rotations between different trials. In the third set
of experiments, the insertion velocity is increased from $v = 2$ mm/sec to $v = 4$ mm/sec and
accordingly the value of the parameter b is updated to 8. As stated in section 2.2, smaller b
leads to a faster error dynamic that makes the error tend to zero faster. In this case the mean
absolute error is 0.37 ± 0.34 mm with a maximum targeting error of 0.89 mm.

In order to study the effect of the tissue on the system's performance, in the next set of
experiments the weight ratio of gelatin to water is increased from 15% to 20%. The results
are shown in Fig. 2.3(a) and 2.3(b). Since the switching threshold is determined according to
(2.18), the deflection error will not change with the change in the tissue properties. However,
the number of rotations depend on how fast the sliding surface, which is a function of the
needle deflection, reaches the switching thresholds and is therefore affected by a change in
tissue properties. A stiffer tissue can cause more deflection as the needle is inserted and
consequently the number of rotations increases. Comparing the result in Table 2.2, it can
be seen that the error for 20% mixture is comparable with that for the 15% mixture but
the average number of rotations is slightly more as the higher weight ratio leads to a stiffer
tissue, which results in more needle deflection. The next set of experiments involve steering
the needle tip to reach a target regardless of its path, which is the case for applications such
as biopsy. According to equation (2.18), the value of $S(0) = ce(0))$ should be considered in
determining S_s. Moreover, in such a condition, the needle should be allowed to deflect more
to reach the desired deflection y_d, and α^* should be selected larger, which leads to different
values for b and c. By choosing a feasible value of α^*, other parameters can be found. Here,
for $y_d = -2$ mm and $\alpha^* = 0.05$ rad, we have chosen $b = 25$ and $c = 1$, which satisfy
(2.8) and lead to $S_s < 1.74$ from which S_s is selected to be 1. The results in Table 2.2 show
a mean absolute error of 0.67 ± 0.75 mm with a maximum targeting error of 0.58 mm. In
the last set of experiments, the biological tissue (pork) is embedded into gelatin used in the
first set of experiments in order to simulate a 2-layer biological tissue. In these experiments,
the tissue is nonhomogeneous as the first layer is gelatin and the second layer is biological

tissue (pork), which itself has different layers. Fig. 2.3(e),2.3(f) and Table 2.2 show the results with a mean absolute error of 0.51 ± 0.32 mm and a maximum targeting error of 1.76 mm. The results show the insensitivity of the proposed method to tissue parameters, meaning that the proposed algorithm has the capability of being used in real tissue with different and nonhomogeneous layers.

From Fig. 2.2 and Fig. 2.3 it can be seen that there is a significant difference between the individual trials. This can be caused by the needle tip initial condition. Though it is attempted to have the initial angle equal to zero for all trials, it is difficult to account for and adjust. Moreover, the insertions may be affected by the tracks made in the tissue caused by previous insertions. Having said the above, the results show the insensitivity of the method to such uncertainties.

In all of the experiments the maximum value of error is less than 2 mm which is the size of the smallest lesion that can be detected by ultrasound images [49]. Moreover the maximum number of rotations obtained in these experiments is comparable to other methods proposed in literature [45].

Table 2.2: Summary of the experimental results using the switching method

	System Parameters						Results					
#	Tissue	b	c	V_{ins} [mm/sec]	S_s	y_d [mm]	Min # of rotation	Max # of rotations	Mean Absolute Error [mm]	σ	RMSE [mm]	Mean Max Error [mm]	Max Targeting Error [mm]
1	gelatin 15%	15	1	2	1	0	3	6	0.62	0.39	0.74	1.39	1.23
2	gelatin 15%	15	1	2	0.5	0	5	9	0.47	0.31	0.61	1.14	0.91
3	gelatin 15%	8	1	4	1	0	4	5	0.37	0.34	0.46	1.01	0.89
4	gelatin 20%	15	1	2	1	0	5	7	0.46	0.33	0.54	1.13	1.16
5	gelatin 15%	25	1	2	0.8	-2	4	7	0.67	0.75	0.92	2.1	0.58
6	biological	15	1	2	1	0	3	7	0.51	0.32	0.59	1.12	1.76

2.4 Discussion

Duty cycle spinning is a technique of simultaneously inserting and rotating the needle, enabling it to move on paths with different curvatures. Many control methods proposed in the literature have combined this technique with different planning methods for needle steering. In this method, the needle is inserted and rotated for the time duration T_{rot} and is inserted for the time duration T_{ins}. The duty cycle factor a is defined as the ratio between these two periods as

$$a = \frac{T_{rot}}{T_{rot} + T_{ins}} \tag{2.19}$$
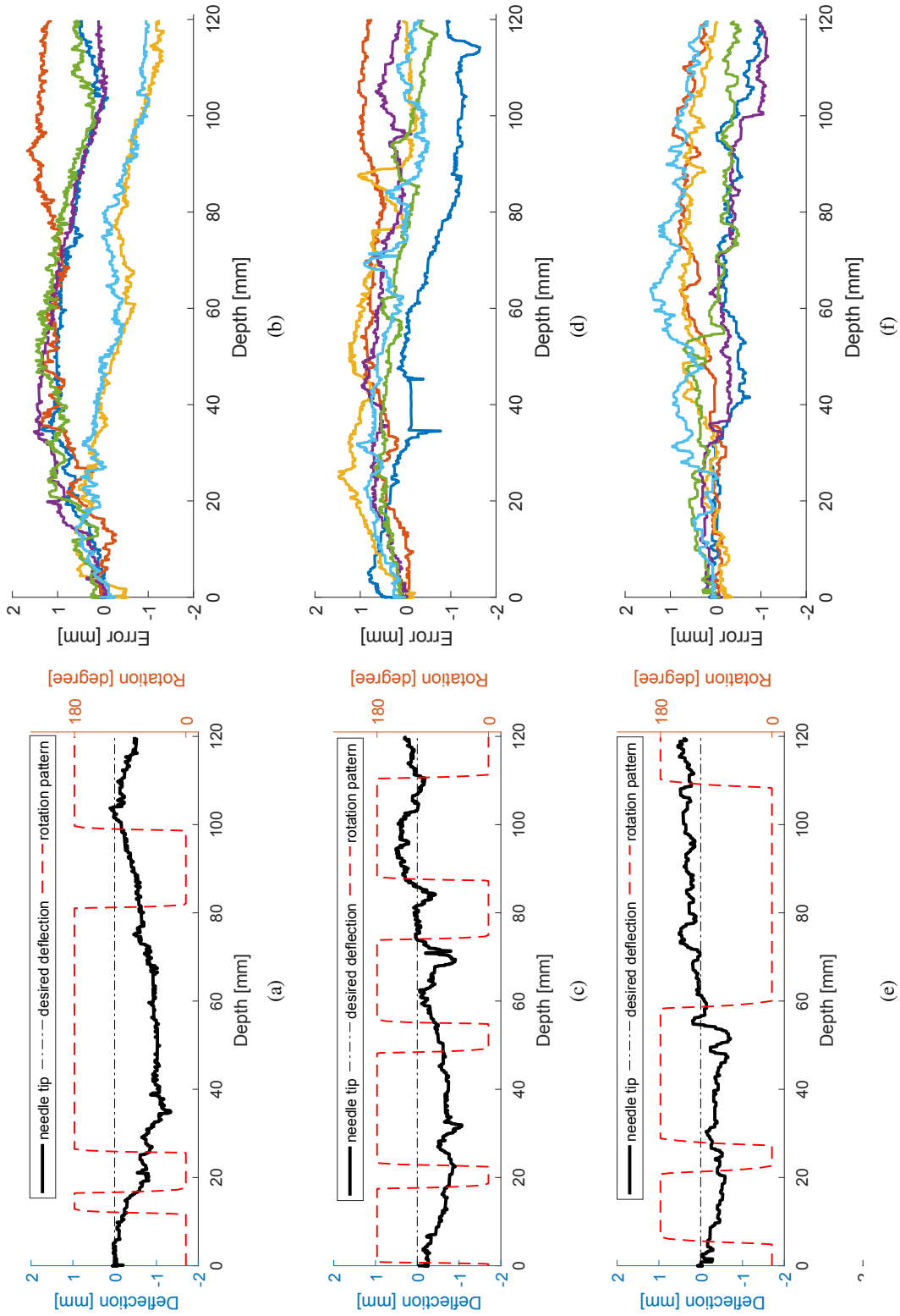
Figure 2.2: Experimental results for needle insertion usign the switching method. (a),(b) for gelatin tissue with $b = 15$, $c = 1$, $S_s = 1$, $y_d = 0\,mm$, $v_{ins} = 2\,mm/sec$ and 15% tissue mixture. (c),(d) for gelatin tissue with $b = 15$, $c = 1$, $S_s = 0.5$, $y_d = 0\,mm$, $v_{ins} = 2\,mm/sec$ and 15% tissue mixture. (e),(f) for gelatin tissue with $b = 8$, $c = 1$, $S_s = 1$, $y_d = 0\,mm$, $v_{ins} = 4\,mm/sec$ and 15% tissue mixture. (a), (c), (e) demonstrate one of the insertion trials as well as the rotation pattern obtained from the controller. (b), (d), (f) show the deflection error for the trials.

27
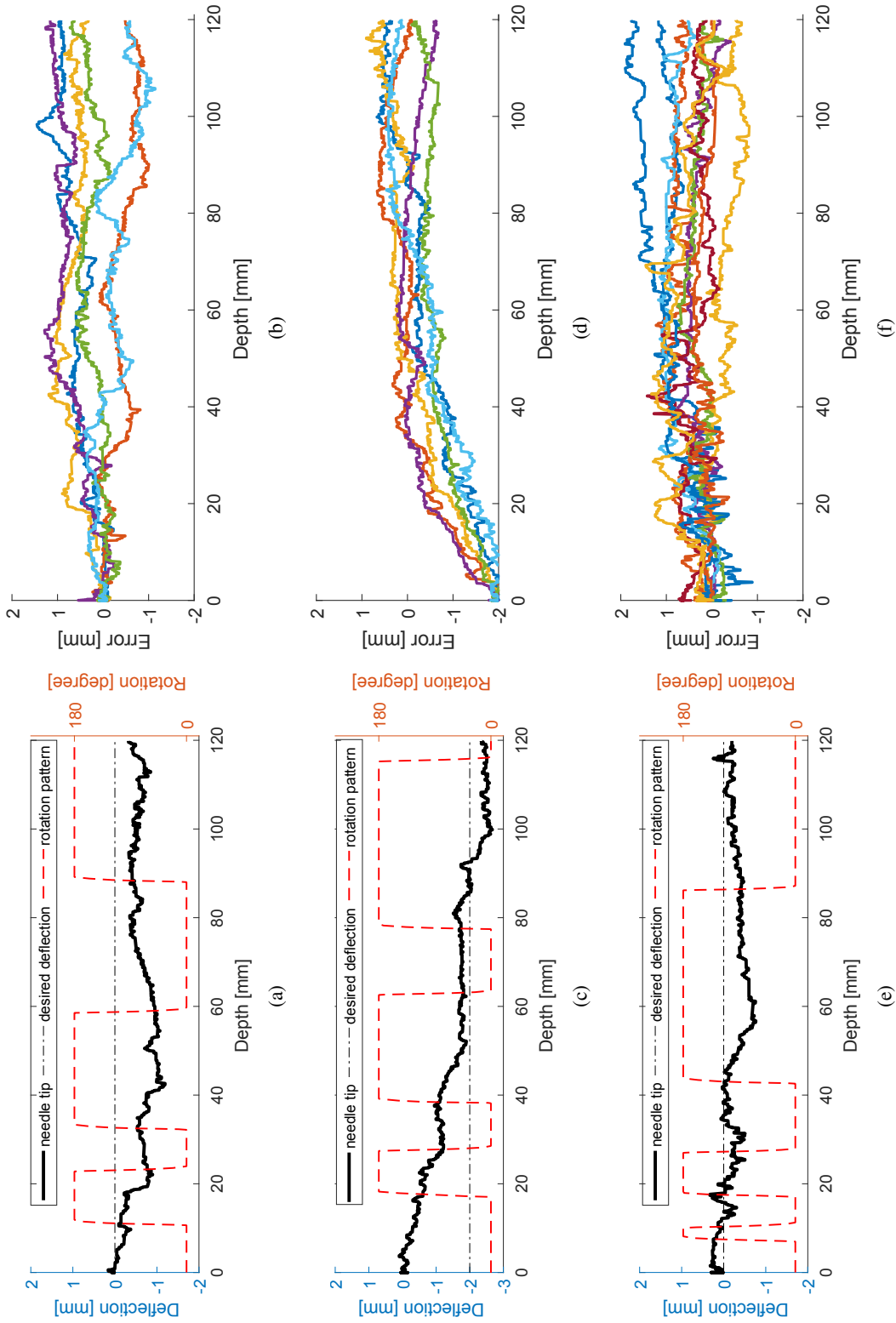
Figure 2.3: Experimental results for needle insertion usign the switching method. (a),(b) for gelatin tissue with $b = 15$, $c = 1$, $S_s = 1$, $y_d = 0 mm$, $v_{ins} = 2\,mm/sec$ and 20% tissue mixture. (c),(d) for gelatin tissue with $b = 25$, $c = 1$, $S_s = 0.8$, $y_d = -2\,mm$, $v_{ins} = 2\,mm/sec$ and 15% tissue mixture. (e),(f) for biological tissue embedded in 15% gelatin mixture with $b = 15$, $c = 1$, $S_s = 1$, $y_d = 0\,mm$ and $v_{ins} = 2\,mm/sec$. (a), (c), (e) demonstrate one of the insertion trials as well as the rotation pattern obtained from the controller. (b), (d), (f) show the deflection error for the trials.

This factor determines the relation between the desired curvature k_{des} and the maximum needle curvature k_{max} as

$$k_{des} = k_{max}(1 - a) \tag{2.20}$$

However, to find a, both k_{max} and k_{des} should be known. k_{max} can be found by pre-operative insertions and by fitting circles to the needle path and k_{des} should be determined by path planning methods. As stated before, for brachytherapy application, it is desired to keep the needle moving on a straight path. For a straight line path with minimum curvature ($k_{des} = 0$), a equals 1 which is equivalent to $T_{ins} = 0$ or continuously rotating the needle. This leads to a large number of rotations and potentially excessive tissue trauma. Moreover, this method requires an exact estimation of the maximum curvature k_{max}, which may be variable during the insertion due to tissue inhomogeneity. The method presented in this chapter does not require any accurate estimation of curvature as some conservative value of it can be employed to determine the switching parameters. Besides, for regulating the needle position to a stationary point, no planning is needed. Moreover, the number of switches can be reduced by increasing the value of switching threshold S_s and accepting some reasonable values of error.

2.5 Concluding Remarks

In this chapter, we have proposed a control structure for steering flexible beveled-tip needles toward fixed points in soft tissue using a two-mode switching control scheme. As a feedback system, the controller is supplied with the needle deflection error obtained from ultrasound images and constructs the control law to switch the system to the proper mode for reducing the targeting error. Using kinematic unicycle equations for the needle, the constraints on switching parameters are derived to ensure the stability of the system and convergence of the error. The experiments show an average error of 0.62 ± 0.39 mm with a maximum number of rotations of 6 in phantom tissue and for the biological tissue an average error of 0.51 ± 0.32 mm with the maximum number of rotations of 7. In the next chapter, this switching idea is extended to control both the in- and out-of-plane deflection to steer the needle to any feasible point or along a desired feasible trajectory in the presence of obstacles in the 3D environment.

Chapter 3

Model Averaging and Input Transformation for 3D Needle Steering

In this chapter, the continuous 3D needle steering problem is modeled as a four-mode switching system, and a new average-based formulation is provided to transform the continuous input into a switching sequence. In this structure, the continuous 3D system is mapped as two, 2-mode switching subsystems with virtual inputs for in-plane and out-of-plane motions. Time-averaging each subsystem across the PWM period can be representative of the original subsystem, which provides a map between the binary-input subsystems and their duty cycle. Each averaged subsystem has its own input, for which a controller can be designed to adjust a switching duty cycle. The duty cycles from the two subsystems are then combined to provide an axial needle rotation command to control the needle deflection in 3D. In order to show the application of the proposed formulation, robust sliding mode technique is employed to design controllers for each subsystem and, thus for the total system in 3D. The controllers are designed to be robust with respect to uncertainties in the value of the needle path curvature and to deal with measurement limitations. The performance of the proposed framework is shown by performing experiments in different scenarios.

Compared to the motion planning methods, in which the errors are compensated through re-planning, the proposed structure is computationally less expensive as the error is compensated by the controller in a feedback loop. Moreover, this new formulation provides a way to utilize different control strategies proposed in the literature and to implement those strategies through a PWM framework. Any controllers designed for continuous-input time-averaged systems that satisfy the system constraints and provide good performance can be used in this framework.

3.1 Switched Four-mode System

For the 2D planar case, there are two possibilities for the bevel, assuming that the needle flips instantly as explained in Chapter 2. In the 3D case, assuming the roll angle γ in 1.4 can only take two fixed values separated by $180°$ in two opposing quadrants, each subsystem is defined as a two-mode switching system. The needle deflection dynamics in the x direction can be written as

$$\dot{x} = v \sin \beta \tag{3.1a}$$

$$\dot{\beta} = (kv)\bar{u}_x \tag{3.1b}$$

or equivalently based on (1.4)

$$\ddot{x} = b_x \bar{u}_x \tag{3.2}$$

where $b_x = kv^2 \cos \beta$ and $\bar{u}_x = \sin \gamma_d$ with $|\sin \gamma_d|$ being constant and $\gamma_d \in [0, \pi]$ to have $\bar{u}_x > 0$, or $\gamma_d \in [\pi, 2\pi]$ to have $\bar{u}_x < 0$, representing the two switching modes. Assuming the switching happens according to the normalized PWM period $D_x = \begin{bmatrix} d_x & 1 - d_x \end{bmatrix}^T$ with $\|D_x\|_1 = 1$, the averaged system is obtained as

$$\ddot{x}_a = d_x b_x |\bar{u}_x| - (1 - d_x)b_x|\bar{u}_x| = b_x u_x \tag{3.3}$$

with

$$u_x = (2d_x - 1)|\bar{u}_x| \tag{3.4}$$

Similarly, for the y direction the subsystem equations can be written as

$$\dot{y} = -v \cos \beta \sin \alpha \tag{3.5a}$$

$$\dot{\alpha} = (kv) \sec \beta \bar{u}_y \tag{3.5b}$$

where $\bar{u}_y = \cos \gamma_d$ with $|\cos \gamma_d|$ being constant. γ_d can have only two values either in $[-\pi/2, \pi/2]$ to have $\bar{u}_y > 0$ or $[\pi/2, 3\pi/2]$ to have $\bar{u}_y < 0$. Using this, (3.5) can equiva-

lently be written based on (1.4) as

$$\ddot{y} = f_y + b_y \bar{u}_y \tag{3.6}$$

with $f_y = kv^2 \sin\alpha \sin\beta \sin\gamma_d$ and $b_y = -kv^2 \cos\alpha$. Using the PWM period $D_y = \begin{bmatrix} d_y & 1-d_y \end{bmatrix}^T$ with $\|D_y\|_1 = 1$, the time-averaged model of (3.6) can be written as

$$\ddot{y}_a = d_y(f_y + b_y|\bar{u}_y|) + (1-d_y)(f_y - b_y|\bar{u}_y|) = f_y + b_y u_y \tag{3.7}$$

in which

$$u_y = (2d_y - 1)|\bar{u}_y| \tag{3.8}$$

In this format, u_x and u_y are continuous virtual inputs to be designed for the subsystems (3.3) and (3.7), respectively. Regardless of the control strategy used for calculating u_x and u_y, in order to use these signals in the switched control, these values should be converted to the duty cycles D_y and D_x using

$$d_i = \frac{(u_i/|\bar{u}_i| + 1)}{2} \quad i = x, y \tag{3.9}$$

The values d_x and d_y determine the duty cycle for switching between the two modes in each subsystem. However, from (3.8) and (3.4), it is clear that u_y and u_x are not independent as they both depend on the value of γ_d. Since $\bar{u}_x$ and $\bar{u}_y$ depend on $\sin\gamma_d$ and $\cos\gamma_d$, respectively, it is possible to integrate the two 2-mode subsystems to build up a four-mode composite system. The four modes can be defined based on the fact that for each subsystem, γ_d is selected to be in a half-plane, i.e., up/down half plane for x direction and left/right half plane for y direction, as shown in Fig. 3.1. These four modes cover the four possibilities for $\sin\gamma_d$ and $\cos\gamma_d$ as each mode represents one quadrant in the plane. Through this selection, the magnitude γ_d can also be considered as a weighting parameter to change the magnitude of $\bar{u}_x$ and $\bar{u}_y$. If $|\tan\gamma| = 1$, the weights over x and y directions are equal; however, it is possible to emphasize error in the x and y directions by selecting $|\tan\gamma_d| > 1$ and $|\tan\gamma_d| < 1$, respectively. Since the duty cycles D_x and D_y determine the time required for the system to stay in each mode, in one cycle, the system uses a maximum number of
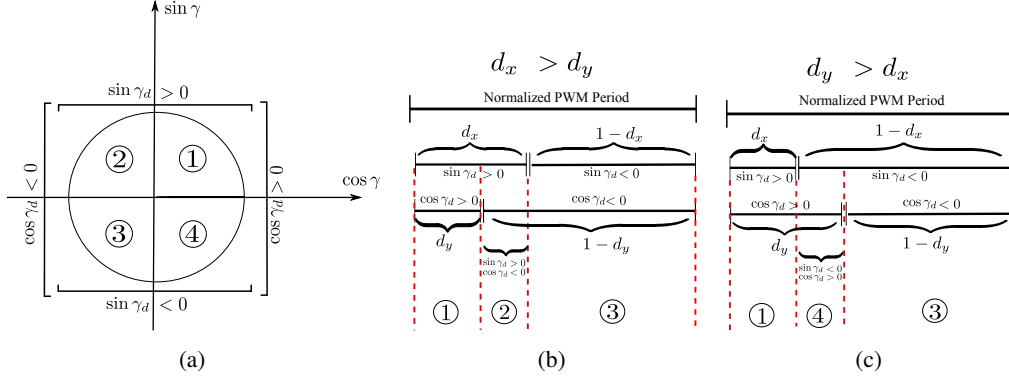
Figure 3.1: The switching pattern for the combined four-mode system. (a): Half planes representing two modes for each subsystem and the corresponding four modes: 1) $\sin \gamma_d > 0, \cos \gamma_d > 0$, 2) $\sin \gamma_d > 0, \cos \gamma_d < 0$, 3) $\sin \gamma_d < 0, \cos \gamma_d < 0$, 4) $\sin \gamma_d < 0, \cos \gamma_d > 0$. (b): The switching pattern when $d_x > d_y$. (c): The switching pattern when $d_y > d_x$

Table 3.1: The four-mode switching pattern based on the duty cycle

	$d_x > d_y$			$d_y > d_x$		
time	d_y	$d_x - d_y$	$1 - d_x$	d_x	$d_y - d_x$	$1 - d_y$
mode	1	2	3	1	4	3

three of the four available modes. The switching sequence can be performed according to the time required for each direction as shown in Table 3.1.

Using this formulation, any continuous control law u_y and u_x which provides the desired performance for the averaged subsystems can be transformed into duty cycles D_y and D_x using (3.8) and (3.4). This provides the possibility of using different control strategies and translating them into a switching framework for steering the needle to the desired position. In the next section, the sliding mode technique is employed for controlling the two subsystems. Due to the uncertainties in the system parameters and the presence of non-measurable states, sliding mode control provides a robust approach for overcoming the uncertainties and disturbances while reaching the desired performance.

The above formulation is based on the assumption that the angle γ can accurately be controlled to the desired value γ_d. However, since the orientation of the needle cannot be measured using ultrasound images, accurate measurement of this angle is not possible. However, since clinically used needles (also used in this work) are torsionally highly stiff and also the curvature for these needles is very small, considering some bounds on the orientation angles, we have assumed that angle γ is equal to the needle base angle.

3.2 Controller

While the average transformed model can be used with more than one control method, we use sliding mode control to show the utility of the averaged model. From equations (3.7) and (3.3), the needle path curvature k enters in the subsystem equations. This parameter depends on needle and tissue properties, which due to tissue inhomogeneity, encounters uncertainties. However, this parameter can be considered to be bounded, with bounds determined by pre-operative tests. Moreover, the angles α and β, representing the needle tip orientation, are also present in the system equations (1.4). Incorporating these angles in the control law requires good measurements or estimations of the needle tip orientation, which is not a trivial task and requires using orientation measurement sensors that are not compatible with clinical realities. Besides, the combination of a state observer with a feedback controller represents new challenges, which require additional analysis for ensuring the stability of the closed-loop system. However, fortunately, the orientation-dependent terms appear as bounded nonlinear functions, which can be considered as an uncertainty around some nominal model.

Sliding mode control is a technique that provides high robustness with respect to parametric uncertainties and other disturbances [97]. According to the uncertainties present in the system, i.e the uncertainty in the curvature and the effects of the bounded orientation terms, the sliding mode control technique seems to suit the requirement of the system. In this section, the nominal model and its associated uncertainties are presented for each subsystem and then a robust sliding mode controller is designed which guarantees the convergence of the uncertain equations.

3.2.1 Model Incorporating Uncertainty

As stated before, the angles α and β are not measurable through ultrasound images. However, these values are considered to be bounded. In reality, due to the presence of the tissue and the limited curvature of the needles, α and β cannot go unbounded. In practice, larger values of these angles correspond to more needle bending, which depends on the desired path travelled by the needle, thus having a feasible desired trajectory for the needle also puts limits on α and β ranges. The limitation can be imposed at the path planning level.

Therefore, it is assumed that $|\alpha| < \alpha^*$ and $|\beta| < \beta^*$, where $\alpha^*, \beta^* \in (0, \pi/2)$ which are determined according to the application at the path planning level. Besides, the value of the curvature k represents a bounded uncertain value as $\underline{k} < k < \bar{k}$. Using these bounds, b_y and b_x in (3.7) and (3.3) satisfy the following inequalities

$$\underline{k}v^2 \cos \beta^* \leq b_x \leq \bar{k}v^2 \tag{3.10a}$$

$$\underline{k}v^2 \cos \alpha^* \leq b_y \leq \bar{k}v^2 \tag{3.10b}$$

Defining $\hat{k}$, $\hat{b}_y$ and $\hat{b}_x$ as the geometric mean of the above bounds, i.e., $\hat{k} = \sqrt{\underline{k}\bar{k}}$, $\hat{b}_y = -\hat{k}v^2\sqrt{\cos \alpha^*}$ and $\hat{b}_x = \hat{k}v^2\sqrt{\cos \beta^*}$, and substituting in (3.3) and (3.7), the nominal subsystem in the x direction can be expressed as

$$\dot{\hat{x}}_a = \hat{b}_x \hat{u}_x \tag{3.11}$$

with

$$\left(\frac{\underline{k} \cos \beta^*}{\bar{k}}\right)^{1/2} \leq \frac{\hat{b}_x}{b_x} \leq \left(\frac{\bar{k} \cos \beta^*}{\underline{k}}\right)^{1/2} \tag{3.12}$$

Similarly, the nominal subsystem in the y direction can be written as

$$\dot{\hat{y}}_a = \hat{f}_y + \hat{b}_y \hat{u}_y \tag{3.13}$$

with

$$|\hat{f}_y - f_y| \leq 2\bar{k}v^2 \tag{3.14a}$$

$$\left(\frac{\underline{k} \cos \alpha^*}{\bar{k}}\right)^{1/2} \leq \frac{\hat{b}_y}{b_y} \leq \left(\frac{\bar{k} \cos \alpha^*}{\underline{k}}\right)^{1/2} \tag{3.14b}$$

3.2.2 Sliding Mode Controller

Considering the y direction, the sliding surface S_y is defined as

$$S_y = \dot{e}_y + ce_y \tag{3.15}$$

with c being a positive constant and $e_y = y - y_d$, where y_d is the desired deflection in y direction to be followed. Taking the time derivative of this sliding surface and substituting from (3.6) gives

$$\dot{S}_y = f_y + b_y u_y - \ddot{y}_d + c\dot{e}_y \tag{3.16}$$

This equation gives the equivalent control law for the averaged system, which constraints the sliding surface to remain on zero.

Substituting (3.13) in (3.16) and solving $\dot{S}_y = 0$ for $\hat{u}_y$ gives

$$\hat{u}_y = \frac{1}{\hat{b}_y}\left(-\hat{f}_y + \ddot{y}_d - c\dot{e}_y\right) \tag{3.17}$$

However, this control law is only valid for the nominal system, which is different from the real system. This can be dealt with by changing the control signal in the following theorem:

Theorem 1. *Consider system (3.7). Selecting $F_y = 2\bar{k}v^2$, $\lambda_y = \left(\frac{\bar{k}\cos\beta^*}{k}\right)^{1/2}$ and $\eta > 0$, the control law*

$$u_y = \hat{u}_y - \frac{1}{\hat{b}_y}K_y sgn(S_y) \tag{3.18}$$

with S_y defined in (4.2) and

$$K_y = \lambda_y(F_y + \eta) + (\lambda_y - 1)|\hat{b}_y\hat{u}_y| \tag{3.19}$$

ensure the convergence to the sliding surface $S_y = 0$.

Proof. Consider the Lyapunov candidate function

$$V_y = \frac{1}{2}S_y^2 > 0 \tag{3.20}$$

Taking the time derivative of S_y and substituting from (3.7), (3.17) and (3.18) gives

$$\dot{S}_y = \left(f_y - \frac{b_y}{\hat{b}_y}\hat{f}_y - (1 - \frac{b_y}{\hat{b}_y})(\ddot{y}_d - c\dot{e}_y) - \frac{b_y}{\hat{b}_y}K sgn(S_y)\right) \tag{3.21}$$

Using (3.19), the above equation can be written as

$$
\begin{aligned}
\dot{S}_y = -\text{sgn}(S_y) &\left(-(f_y - \hat{f}_y)\text{sgn}(S_y) + \frac{b_y}{\hat{b}_y}\lambda_y F_y \right) \\
- \text{sgn}(S_y) &\left(|\hat{b}_y\hat{u}_y|(\lambda_y - 1 - (\frac{b_y}{\hat{b}_y} - 1)\text{sgn}(S_y)\text{sgn}(\hat{b}_y\hat{u}_y)) \right) \\
- \text{sgn}(S_y) &\frac{b_y}{\hat{b}_y}\eta
\end{aligned}
\tag{3.22}
$$

From (3.14), since $|f_y - \hat{f}_y| < F_y$ and $\lambda_y > \frac{b_y}{\hat{b}_y} > 1$, the above equations leads to

$$
\dot{S}_y \leq -\eta\text{sgn}(S_y)
\tag{3.23}
$$

which by multiplying the sides of this inequality by S_y gives

$$
S_y\dot{S}_y \leq -\eta|S_y|
\tag{3.24}
$$

which shows the finite time convergence of the sliding surface S_y. □

Similarly, for the x direction the sliding surface S_x is defined as

$$
S_x = \dot{e}_x + ce_x
\tag{3.25}
$$

in which $e_x = x - x_d$ with x_d being the desired deflection in the x direction and c being a positive constant. The equivalent control law $\hat{u}_x$ is found as

$$
\hat{u}_x = \frac{1}{\hat{b}_x}(\ddot{x}_d - c\dot{e}_x)
\tag{3.26}
$$

Theorem 2. *Consider system (3.3). Selecting $\lambda_x = \left(\frac{\bar{k}\cos\beta^*}{\underline{k}} \right)^{1/2}$ and $\eta > 0$ the control law*

$$
u_x = \hat{u}_x - \frac{1}{\hat{b}_x}K_x sgn(S_x)
\tag{3.27}
$$

with

$$
K_x = \lambda_x\eta + (\lambda_x - 1)|\hat{b}_x\hat{u}_x|
\tag{3.28}
$$

ensure the convergence to the sliding surface $S_x = 0$, where S_x and $\hat{u}_x$ are defined in (3.25) and (3.26), respectively.

Proof. Similar to Theorem 1. □

3.3 Path Planner

In the presence of anatomical obstacles, the needle should be guided on a pre-planned path. This path should be found as a feasible trajectory that minimizes the targeting error and avoids any obstacles. In this case, the steering problem turns into a trajectory tracking problem, which is explained in the next section. The control method proposed in the previous section is a general controller that does not depend on any specific planning method as only the position error and its time derivative are involved in the control algorithm. The feasible path can be found using offline path planning methods. However, the targeting accuracy can be improved by doing online re-planning to compensate for any disturbances caused by tissue inhomogeneity. This online re-planning can be updated at a slower rate with respect to the control loop to ensure that there will be a feasible path from the current position to the target while manoeuvring around the obstacles.

Here, an offline path planner is used to find a desired path that reaches the target point and avoids collisions with anatomical obstacles. The location of the target point and the obstacles are determined by pre-operation scans which are fed to the planner which uses the kinematic 3D unicycle equations (1.4). In this planning method, the insertion depth is divided into n points at which needle rotations should occur. The values of the needle roll angle at these n intervals are the output of the planner. Having a closed-form response [20], Algorithm 1 can be used to find the rotation values at n samples. In this algorithm, the function `costfunction` calculates the tip deflection at each sample n and also at the obstacle to minimize the tip deflection error at the target and maximize the distance from the obstacle. However, the proposed control method is not limited to this planner and any other offline or online path planning methods can be used to produce the desired trajectory or make corrections to find a feasible path from current needle's position to the target.

Algorithm 1: Path Planner

---

1 Initialize: T_0
2 Select T randomly
3 $Cost_0 = \texttt{costfunction}(T_0)$
4 **while** $i < \textit{Max\_iteration}$ **do**
5 $Cost = \texttt{costfunction}(T)$
6   **if** $Cost < Cost_0$ **then**
7 $T_0 \leftarrow T$
8 $Cost_0 \leftarrow Cost$
9   **end**
10   **else if** $prob(Cost, Cost_0, T_0, T) > \textit{random}()$ **then**
11 $T_0 \leftarrow T$
12 $Cost_0 \leftarrow Cost$
13   **end**
14 $\texttt{update}(T)$
15 $i = i + 1$
16 **end**

3.4 Experiments

In this section, the performance of the proposed controller implemented in the switching framework is verified using the experimental setup shown in Fig. 1.3. Validation is performed by conducting three sets of experiments, each having nine trials. The insertion points for all trials are spaced far enough apart to prevent any crossing with previous needle tracks in the tissue. The experiments are implemented for two different scenarios. The first scenario is aligned with the main goal of this work, in which the needle is moved on a straight line and is applicable to brachytherapy procedures. It should be noted that in this scenario, it is desired to steer the needle on a straight path in 3D space, which is equivalent to keeping the needle deflection in both the x and y direction close to zero. Two different plastisol phantom tissues are used in these experiments. These tissues are made of 80% plastic and two different percentage of softener (M-F Manufacturing Co., Fort Worth, TX, USA), 20% and 10%, to have with different stiffness. The Young's modulus of elasticity of these tissues is 25 kPa and 35 kPa. The needles used in these experiments are standard 18-gauge brachytherapy needles (Eckert & Ziegler BEBIG Inc., Oxford, CT, USA) made of stainless steel, with an outer diameter of 1.27 mm, an inner diameter of 1 mm, and a bevel angle of approximately $20°$. In order to show the ability of the proposed structure for steering the needle on a curved

path, in the second scenario, the needle is moved on a pre-planned path, which is applicable in the presence of obstacles on the needle's way to the target. In this scenario, since it is aimed to steer the needle on a curved path, highly flexible notched needles [98] are used.

The trials are performed for a constant insertion velocity of $v = 2$ mm/sec and an insertion depth of 140 mm. Using previous data and pre-operative experiments, the curvature is selected as $0.0024 \leq k \leq 0.0027$ mm^{-1}, which is used in the simulations to find the bounds α^* and β^* as 0.2 rad. γ_d is selected such that $|\tan \gamma_d| = 1$ and the value of the sliding mode parameters c and η are selected as 0.1 and 0.5, respectively, using simulations and trial and error.

In the first scenario, the desired path is defined as a straight line, which is equivalent to keeping the needle deflection in both the x and y directions equal to zero. The results for tissue 1 show a mean absolute error of 0.37 mm in x and 0.3 mm in y. Implementing the same scenario for tissue 2 results in a mean absolute error of 0.28 mm and 0.4 mm for x and y, respectively. Since the control method used here is robust with respect to uncertainties, the errors obtained from two different tissues are of the same order, which shows show that the method does not depend on the tissue parameters.

In the second scenario, the needle is steered on a pre-planned path to reach a depth of 140 mm and to avoid an obstacle at a depth of a 80 mm to simulate pubic arch interference (PAI) [99], which is common in patients with a large prostate. PAI obstructs the needle path to the anterior prostate, resulting in poor seed placement and dose reduction [100]. According to [101], the average prostate size for men between the ages of 40 and 50 is 44 mm in width, 31 mm in height and 37 mm in length. To simulate a severe PAI, a 10 mm interference between pubic arch and prostate is considered and modeled as an obstacle with radius of 2 mm. The desired path is found using the algorithm introduced in section 3.3 for $n = 5$.

The results show a mean absolute error of 0.36 mm and 0.24 mm in the x and y directions, respectively. The maximum targeting error obtained from the experiments is 0.83 mm for x and 1.08 mm for y, as summarized in Table 3.2. Fig. 3.2(a), 3.2(d) and 3.2(g) represent the results for one of the trials in the x direction from each experimental set. The deflection in the y direction is shown in Fig. 3.2(b), 3.2(e) and 3.2(h), and the four switched modes are shown in Fig. 3.2(c), 3.2(f) and 3.2(i). To have a better idea of the path followed, a 3D plot for one of the trials for case 3 is shown in Fig. 3.3.

40

The switching framework proposed in this chapter provides the opportunity to use different control strategies. Any controller designed for the two subsystems which satisfies the system constraints can be used. Here, the sliding mode controller is used as an example to show the effectiveness of the method, however, it is not the only choice. Comparing the results, the maximum error obtained in the experiments is 1.5 mm which is less than 2 mm, the size of the smallest lesion detectable in ultrasound images [88]. The errors are also of the same order as for other methods proposed in the literature, such as [102] and [46], in which the final targeting errors are 1.08 mm and 1.3 mm, respectively. This new formulation also has the capability to be used with other control strategies to improve performance, which requires further research.

Table 3.2: Summary of the experimental results using the PWM framework

Case	Tissue	Scenario	x direction				y direction			
			Mean Absolute Error [mm]	Standard Deviation σ [mm]	RMSE [mm]	Max Targeting Error [mm]	Mean Absolute Error [mm]	Standard Deviation σ [mm]	RMSE [mm]	Max Targeting Error [mm]
1	Tissue 1	Move on a straight line	0.37	0.4	0.48	1.5	0.3	0.31	0.31	0.6
2	Tissue 2	Move on a straight line	0.28	0.26	0.34	0.94	0.4	0.44	0.44	1.4
3	Tissue 1	Obstacle Avoidance	0.36	0.33	0.47	0.83	0.24	0.25	0.25	1.08

3.5 Concluding Remarks

In this chapter, a formulation for transforming the needle steering problem in 3D space into a switching framework is proposed. In this formulation, the needle tip deflection is projected into two directions, for which two controllers can be designed independently and translated as duty cycles. The duty cycles are then combined to form a four-mode switching system which simultaneously compensates for deflections in both directions. Later using the sliding mode technique, a robust sliding mode controller is designed for each subsystem and implemented in the proposed switching framework. The proposed framework can be combined with other available control strategies for minimizing the deflection error. The sliding mode controller proposed here is a conservative method, in which all unknown values are incorporated as uncertainties. In the next chapter, a sliding-based method is introduced to replace the switching behavior with continuous rotations to reduce the number of rotations and the possible tissue trauma.
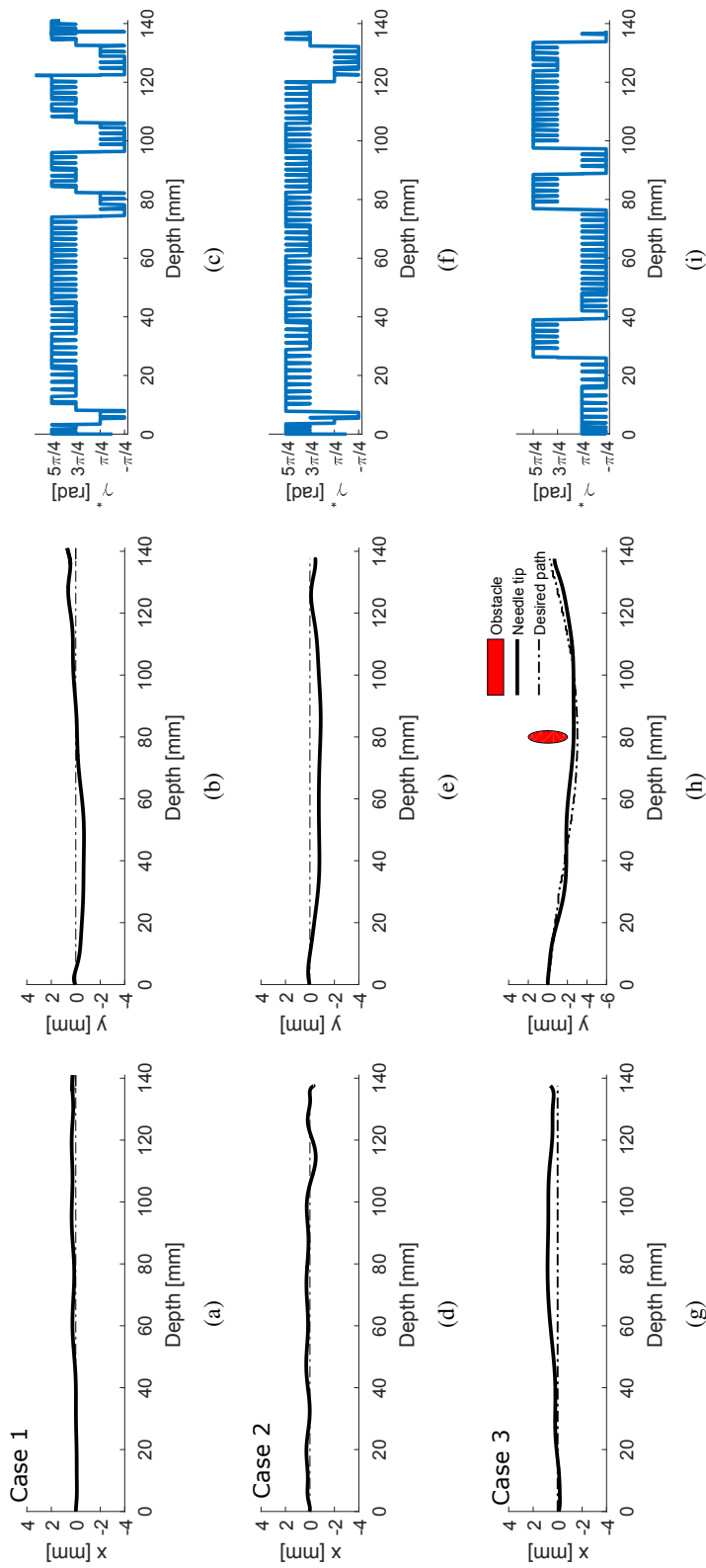
Figure 3.2: Experimental results presenting the needle tip deflection in one trial in plastisol tissue with insertion velocity of 2 mm/sec and insertion depth of 140 mm. (a), (b): deflection for tissue 1 and desired path of straight line. (c): angle γ_d determining the switching mode for case 1. (d), (e): deflection for tissue 2 and desired path of straight line. (f): angle γ_d determining the switching mode for case 2. (g), (h): deflection for tissue 1 and desired path of pre-defined curve. (i): angle γ_d determining the switching mode for case 3.
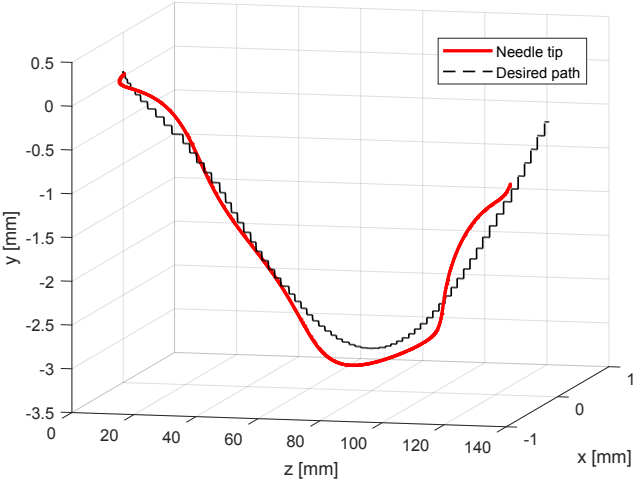
Figure 3.3: 3D representation of the needle following the desired curved path in one of the trials.

Chapter 4

Sliding-based 3D Needle Steering

This chapter presents a sliding-based control method to steer the needle in 3D space as the needle is inserted to the desired depth and toward the desired position. In the needle/tissue system, due to the tissue inhomogeneity, the needle/tissue interaction and the needle's path curvature encounter uncertainties, for which it is desired to design controllers robust with respect to uncertainties and disturbances. The proposed method compensates for position errors by performing the required needle rotations, which can be tiny adjustments to the needle orientation. This removes any unnecessary rotations and reduces the trauma on tissue caused by continuous rotations. In this method, the position information from the ultrasound images is used, and no information about the needle tip orientation and/or tissue properties is required to find the control signal.

In this work, two surfaces are considered and the required rotation angle is found using these two sliding surfaces to compensate the tip deflection error in 3D space. The proposed method is then improved by using an adaptive-structure controller, in which the sliding surfaces are rotated. This modification relaxes some constraints imposed by stability conditions. Moreover, it removes any dependence of the parameters on the needle path's curvature.

4.1   Steering Method

The proposed method is based on determining the desired value of the needle roll angle γ that steers the needle to the desired deflection, which depends on the application. There are different applications for needle insertion systems such as biopsy and brachytherapy. In biopsy it is desired to reach a constant desired deflection, regardless of the path. In brachytherapy, the path traveled by the needle is important as the seeds are implanted on the needle track during the needle retraction. In this procedure the goal is to minimize the deflection at all depths, which is equivalent to having zero deflection at all times. In both cases the desired deflection values are constants. Having the desired value γ_d, the needle axial rotation velocity u can be found such that γ tracks the desired value γ_d, which steers the needle to the desired deflection. According to (1.4), having full control over γ requires
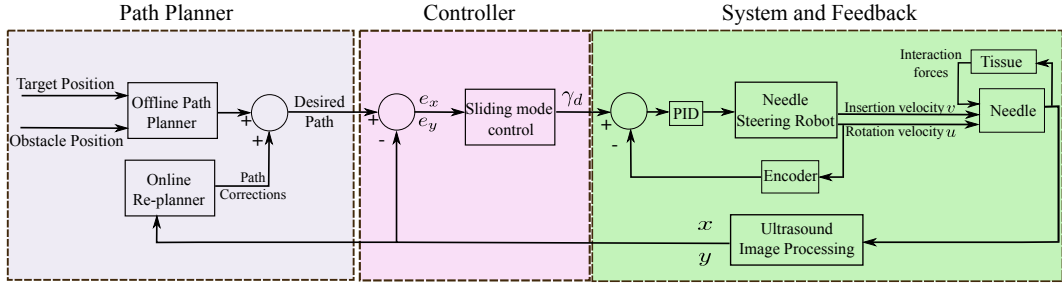
44

Figure 4.1: The closed-loop structure consisting of system, controller and path planner.

knowledge of needle tip orientation, i.e., the angles γ and β. Measuring the orientation requires utilizing a needle-mounted sensor, which itself suffers from sterilization and size issues. Since suitable sensors are not accessible, state observers can be employed to estimate the needle tip orientation using the measured needle tip position [47]. The estimation of the needle tip orientation is not a trivial task, which is not the focus of this work. In this chapter the control strategy finds the desired value of the angle γ which is considered as the desired needle base angle. Since clinically used needles (also used here) are torsionally highly stiff and also the curvature for these needles is very small, we have assumed that angle γ is equal to the needle base angle γ_d. Besides, since the method used here is based on sliding mode control, the method will be robust with respect to these errors. The control structure is shown in Fig. 4.1. In this figure, the control structure is implemented as a cascade loop. The inner loop uses a PID controller to control the needle base angle. The outer loop is a sliding mode controller which determines the desired angle as the input of the inner loop. In other words, the sliding mode controller determines when and how much for the needle be rotated to decrease the error, and the PID controller in the inner loop is responsible for rotating the needle to the desired angle. This PID controller is totally independent from the sliding mode controller and is designed to be fast enough so its dynamics can be neglected.

4.1.1   Fixed Structure

The main idea of a sliding mode controller is to define a suitable error dependent sliding surface S and the corresponding switching law to bring the system manifolds onto the sliding surface and decrease it. To this end the switching law should make the time derivative of the Lyapunov function $V = \frac{1}{2}S^2$ negative definite, which is equivalent to a decreasing surface

and consequently a decreasing error. Here, two sliding surfaces are defined for the x and y directions and the needle roll angle is switched in four different modes. Like all sliding based controllers, the system response consists of two phases, the reaching phase and the sliding phase [97]. In the reaching phase the system moves towards the desired surface $S_i = 0, (i = x, y)$ and in the sliding phase, in the ideal case, the system states remain on the desired surface, which makes the error go to zero. For the system considered here, the reaching phase is when the value of S_x and S_y are decreasing, however the sliding phase will never happen for this system as it does not have any equilibrium point other than the velocity being equal to zero. As long as the needle is being inserted, the velocities are changing and the needle bends. This will make the sliding phase involve chattering, which can be compensated for by accepting some bounds on error and performing the switches at some time intervals. This is equivalent to keeping the sliding surfaces close to zero. To this end, define the following sliding surfaces

$$S_x = b_x \dot{e}_x + e_x \tag{4.1}$$

$$S_y = b_y \dot{e}_y + e_y \tag{4.2}$$

Having x_d and y_d as the desired deflections in the x and y directions which should be reached at a certain depth, $e_x = x - x_d$ and $e_y = y - y_d$ represent the position errors in the x and y directions, respectively, and b_x and b_y are the design parameters to be chosen later.

Considering the desired position in 3D space is a constant deflection at a certain depth, i.e. $\dot{x}_d = \dot{y}_d = 0$, the time derivatives of the sliding surfaces are:

$$\dot{S}_x = b_x \ddot{x} + \dot{x} \tag{4.3}$$

$$\dot{S}_y = b_y \ddot{y} + \dot{y} \tag{4.4}$$

Taking the time derivative of $\dot{x}$ and $\dot{y}$ in (1.4) and substituting from (1.4), the above equations can be written as

$$\dot{S}_x = b_x k v^2 \cos \beta \sin \gamma + v \sin \beta \tag{4.5}$$

CHAPTER 4. SLIDING-BASED 3D NEEDLE STEERING

$$\dot{S}_y = -b_y k v^2 \cos\alpha \cos\gamma - b_y k v^2 \sin\beta \sin\alpha \sin\gamma + v \cos\beta \sin\alpha \qquad (4.6)$$

In these equations, since $-\pi/2 \le \beta \le \pi/2$, it is assumed that $\cos\beta$ is always positive. As stated before, since in sliding mode control the sign of the sliding surface and its derivative are of interest, considering the x direction, (4.5) consists of two terms on the right hand side, which can be positive or negative. If the absolute value of the first term is greater than the second term, regardless of the sign of the second term, $\dot{S}_x$ will have the same sign as the first term. Mathematically, this can be written as

$$|b_x k v^2 \cos\beta \sin\gamma| > v \sin\beta \qquad (4.7)$$

If (4.7) is satisfied, using the assumption that $\cos\beta > 0, k > 0, b_x > 0$ and $v > 0$, then $\operatorname{sgn}(\dot{S}_x)$ is the same as $\operatorname{sgn}(\sin\gamma)$. This inequality is equivalent to

$$|\sin\gamma| > \frac{1}{b_x k v}|\tan\beta| \qquad (4.8)$$

Similarly for the y direction, if

$$|\cos\gamma| > |\sin\beta \tan\alpha \sin\gamma| + \frac{1}{b_y k v}|\cos\beta \tan\alpha| \qquad (4.9)$$

$\operatorname{sgn}(\dot{S}_y)$ is determined by $-\operatorname{sgn}(\cos\gamma)$. Assuming (4.8) and (4.9) are satisfied, (which later will be considered as a constraint), the sign of S_x and S_y can be used to determine in which quadrant γ should reside. The four different possibilities are shown in Fig. 4.2. For example, if $S_x > 0$ and $S_y < 0$, in order to have a decreasing error it is needed to have $\dot{S}_x < 0$ and $\dot{S}_y > 0$, which is equivalent to $\sin\gamma < 0$ and $\cos\gamma < 0$ or having γ in the 3rd quadrant. Moreover, in order to incorporate the magnitude of the sliding surfaces S_x and S_y in compensating the error, the desired angle γ_d is defined as

$$\gamma_d = \operatorname{atan2}(-S_x, S_y) \qquad (4.10)$$

where $\gamma_d \in [-\pi, \pi]$ and the function atan2 is the tangent inverse function, which takes into account the sign of the two inputs to return the appropriate quadrant of the calculated angle.
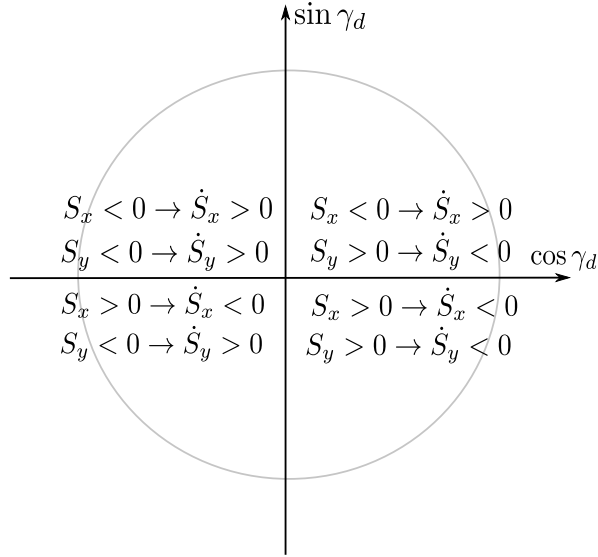
Figure 4.2: The four possibilities for S_x and S_y and the corresponding quadrant for γ_d.

This selected quadrant (or mode) plays the main role in decreasing the error as it ensures that both sliding surfaces S_x and S_y decrease simultaneously.

To ensure that (4.8) and (4.9) are satisfied simultaneously, the system parameters can be selected such that these two inequalities are satisfied for the worst case of α and β. Assume $|\alpha| < \alpha^*$ and $|\beta| < \beta^*$ where $\alpha^* > 0$ and $\beta^* > 0$ are the bounds of angles α and β, respectively. The above inequalities can be written as

$$
\begin{aligned}
\arcsin\left(\frac{1}{b_x kv}\tan\beta^*\right) &< |\gamma_d| < \\
\arccos\left(\sin\beta^*\tan\alpha^* + \frac{1}{b_y kv}\cos\beta^*\tan\alpha^*\right)
\end{aligned}
\tag{4.11}
$$

in which α and β are substituted by α^* and β^*, respectively. The values of b_x, b_y and the upper bounds α^* and β^* should be selected such that the arguments of $\arcsin$ and $\arccos$ are less than 1 and (4.11) is feasible. According to the target point, the value of α^* and β^* can be determined at the planning level considering that larger values of α^* and β^* correspond to more needle bending leading to a larger reachable workspace.

This condition is also affected by the value of the sliding surface parameters, b_x and b_y, which should be selected in accordance with α^*, β^* and k. According to (4.1) and (4.2), in order to have a faster response, it is desired to have smaller values of of b_x and b_y because
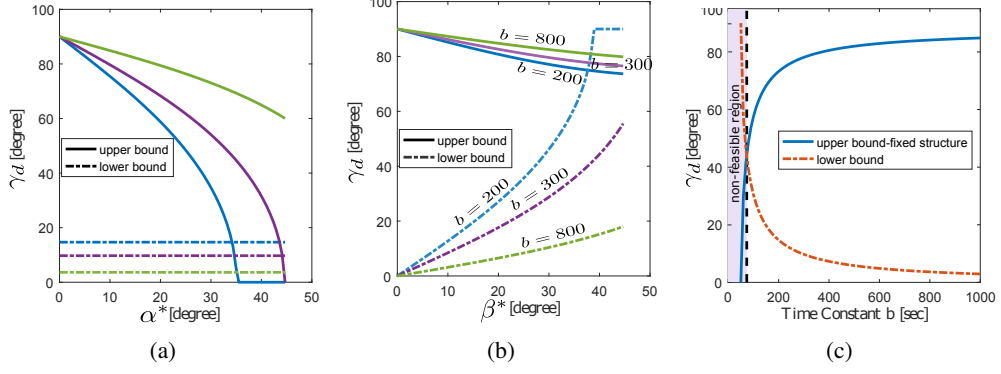
Figure 4.3: The effect of the design parameters on the feasible range of γ_d for $k = 0.002$ mm^{-1} and $b_x = b_y = b$. (a) shows the effect of increasing α^* for different values of b and $\beta^* = 0.2$ rad. (b) shows the effect of increasing β^* for different values of b and $\alpha^* = 0.2$ rad. (c) shows the effect of increasing b for $\alpha^* = \beta^* = 0.2$ rad.

they determine the convergence time of e_x and e_y as S_x and S_y tend to zero. However, this condition forces α^* and β^* to be small to make (4.11) feasible. The effect of α^*, β^* and b_i $(i = x, y)$ on the desired value γ_d is shown in Fig. 4.3 for $k = 0.002$ mm^{-1} and $b_x = b_y$. Fig. 4.3(a) and 4.3(b) show that small values of α^* and β^* lead to a larger range for γ_d. For example, if $\alpha^* = \beta^* = 0$, (4.11) simplifies to $0 < |\gamma_d| < \pi/2$, the maximum acceptable region. In this case, the sliding surface parameters can be selected arbitrarily, however, having $\alpha^* = \beta^* = 0$ is equivalent to having no deflection at the needle tip throughout the insertion, which according to the physical nature of the system is not possible. Moreover, increasing α^* and β^* makes the acceptable range for γ_d smaller until no value for γ_d can be found. Fig. 4.3(c) shows the effect of sliding parameter $b_x = b_y$ for the fixed values of $\alpha^* = \beta^* = 0.2$ rad. As can be seen, by increasing b the feasible range for γ_d gets larger, and smaller values of b_i $(i = x, y)$ might lead to a non-feasible value for γ_d.

4.1.2 Adaptive Structure

As stated before, it is desired to have small sliding surface parameters as they determine the convergence time of the error in both the x and y directions. From (1.4), it is clear that as the needle is moving forward, there are no equilibrium points for the system and it is not possible to make the time derivative of the system state errors zero. Using the sliding surface in the previous section, the system is pushed toward the constant sliding surface and kept as
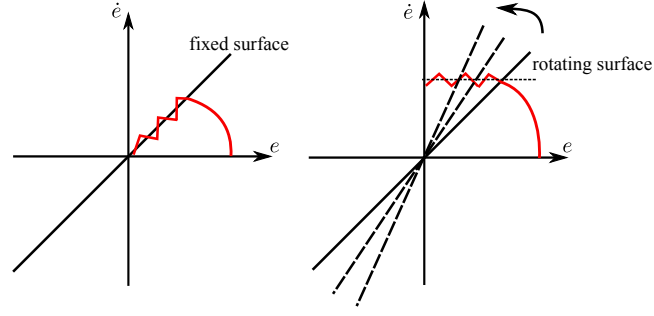
Figure 4.4: Fixed and adaptive sliding surfaces in the phase plane.

close as possible to this surface, which moves the errors in the x and y directions and their first derivative toward zero. Since the time derivatives of the system states are changing, it is only possible to focus on the deflection error and not its derivative. This can be done by rotating the sliding surface at a constant rate in such a way that as the needle is inserted, the error signals in the x and y directions approach zero. This is shown in Fig. 4.4. The sliding surfaces defined by (4.1) and (4.2) represent a line in the phase plane whose slope equals $\frac{1}{b_i}$ $(i = x, y)$. By changing b_i, the lines rotate about the origin. As is shown, by increasing the slope of the line and rotating the sliding surface toward the vertical axis, the error in the phase plane approaches zero. In this case, the sliding surfaces are defined as in (4.1) and (4.2) but the parameters b_x and b_y are variable, which leads to

$$\dot{S}_i = b_i \ddot{e}_i + \dot{e}_i \left(\dot{b}_i + 1 \right), \ i = x, y \tag{4.12}$$

Selecting $\dot{b}_i = -1$ leads to

$$\dot{S}_x = b_x k v \cos \beta \sin \gamma \tag{4.13}$$

$$\dot{S}_y = -b_y k v \cos \alpha \cos \gamma + b_y k v \sin \beta \sin \alpha \sin \gamma \tag{4.14}$$

It should be noted that the parameters b_x and b_y should always be positive. This can be guaranteed by knowing the desired insertion depth, D, the constant insertion velocity, v, and choosing the initial value $b_i(0) \geq \frac{D}{v}$. With the proposed fixed and adaptive structures, the rotating sliding surface removes the constraint imposed by (4.8) and relaxes the constraint

imposed by (4.9) as

$$|\tan \gamma_d| < \frac{1}{\sin \beta^* \tan \alpha^*} \tag{4.15}$$

in which there is no dependence on the needle path curvature k. This condition is obtained for the worst case representing a conservative performance. The effect of this saturation is shown in Fig. 4.5 by performing simulations for different values of the upper bound for γ_d and ignoring the stability. The results are shown for $b(0) = 80$, with an insertion velocity of 2 mm/sec, a maximum insertion depth of 140 mm, and the desired path being a straight line. The figure shows that the effect of limiting γ_d is negligible; however, having saturation on γ_d ensures the stability of the system. In the fixed structure, the values of sliding surface parameters b_i are lower bounded due to the constraints imposed by the stability condition, and for these fixed values, the weight of the error in the sliding surface does not change. In the adaptive structure, as the needle reaches the desired depth, b_i gets smaller and the position error in the sliding surface gets more heavily weighted, leading to smaller errors.

Equations (4.13) and (4.14) obtained for the adaptive structure are simpler than (4.5) and (4.6), for which (4.10) still ensures $\dot{S}_x S_x < 0$ and $\dot{S}_y S_y < 0$. Assuming $\gamma = \gamma_d$ at each time interval, substituting γ_d in (4.13) gives:

$$\dot{S}_x < -\eta_x S_x, \quad S_x > 0 \tag{4.16a}$$

$$\dot{S}_x > -\eta_x S_x, \quad S_x < 0 \tag{4.16b}$$

$$\dot{S}_y < -\eta_y S_y, \quad S_y > 0 \tag{4.17a}$$

$$\dot{S}_y > -\eta_y S_y, \quad S_y < 0 \tag{4.17b}$$

with

$$\eta_x = \frac{b_x k v \cos \beta^*}{\sqrt{S_{x0}^2 + S_{y0}^2}} > 0 \tag{4.18a}$$

$$\eta_y = \frac{b_y k v |\cos \alpha - \cos \alpha^*|}{\sqrt{S_{x0}^2 + S_{y0}^2}} > 0 \tag{4.18b}$$

where S_{x0} and S_{y0} are the values of S_x and S_y, at the beginning of the time interval, respectively. Multiplying the sides of (4.16) and (4.17) by S_x and S_y, respectively, gives $S_x \dot{S}_x < -\eta_x S_x^2$ and $S_y \dot{S}_y < -\eta_y S_y^2$, which show the finite time convergence of the sliding surface during the reaching phase.

4.1.3   Stability

It should be noted that according to the physical properties of the system, it is not possible for the three angles, representing the orientation, to go unbounded. With its desired value being γ_d, which is bounded, the roll angle will obviously remain bounded. Unbounded β and α would be equivalent to the needle tracking a full circle in the tissue, which according to the curvature of the needle and in the presence of tissue, is not possible. However, In order to use the proposed method, the system states should stay in (1.3) so that the equations are valid. Since the control law is updated at the beginning of the intervals, assuming $\gamma = \gamma_d$ and taking its time derivative gives

$$\dot{\gamma} = -\frac{\dot{S}_x S_y - \dot{S}_y S_x}{S_x^2 + S_y^2} = -\cos\gamma \tan\beta \tag{4.19}$$

from which

$$\tan\beta = \frac{1}{\cos\gamma} \frac{\dot{S}_x S_y - \dot{S}_y S_x}{S_x^2 + S_y^2} \tag{4.20}$$

Note that $\cos\gamma \neq 0$ as γ is selected according to (4.15). Consider the following Lyapunov function:

$$V = \frac{1}{2} \left(\tan^2\beta + M \left(S_x^2 + S_y^2 \right) \right) \tag{4.21}$$

Here, M is a large positive constant. Taking the time derivative of (4.21) and substituting from (4.20) and using $\tan\gamma = \frac{S_x}{S_y} sgn(S_x S_y)$ gives

$$\dot{V} = S_x \dot{S}_x \left(M + kv \frac{sgn(S_x S_y)(1 + \tan^2\beta)}{S_x^2 + S_y^2} \right) + \\ S_y \dot{S}_y \left(M - kv \frac{sgn(S_x S_y)(1 + \tan^2\beta)S_x^2}{(S_x^2 + S_y^2)S_y^2} \right) \tag{4.22}$$

Since $S_x \dot{S}_x < 0$ and $S_y \dot{S}_y < 0$, choosing $M > max(kv\frac{(1+\tan^2\beta^*)}{S_x^2+S_y^2}), kv\frac{(1+\tan^2\beta^*)S_x^2}{(S_x^2+S_y^2)S_y^2})$, the above equation ensures that $\dot{V} \leq 0$, which is equivalent to V being decreasing during
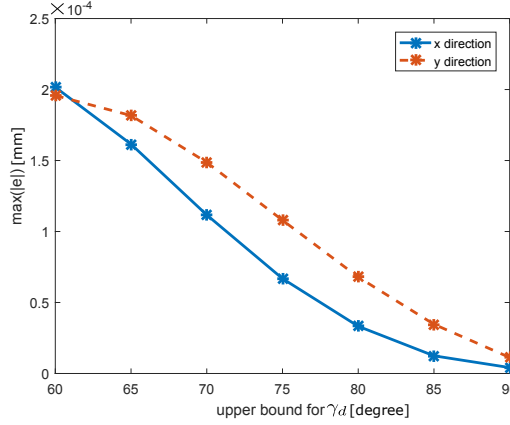
Figure 4.5: The effect of upper bound on γ_d on performance in simulations for moving the needle on a straight line.

the reaching phase, in which $S_x \neq 0$ and $S_y \neq 0$. During the sliding (i.e. chattering) phase, if $S_x = 0$ then $\gamma_d = 0$ and still the above inequality holds. If $S_y = 0$, γ_d should be saturated by the constraint (4.15), for which $\dot{\gamma} \neq 0$ and S_y moves away from zero. This shows that V remains bounded or $\beta \neq \pm\pi/2$.

It should be noted that β^* is selected properly according to the application and the needle/tissue specifications as follows. From the system equations (1.4), $|\dot{\beta}| \leq kv$. Starting from zero initial condition (which is true as the needle is unbent at the beginning), the maximum value of β can be found by taking the integral of this inequality. Since the needle length, L, is bounded and the variation of the needle length inside the tissue is $\dot{\ell} = v$, the maximum value of β can be found as $\beta < kL$. Using this maximum value, β^* can be selected accordingly. In practice, since the needle path curvature is small and the needle length is limited, $|\beta|$ will also remain bounded and less than β^*. Similar discussion can be made for the angle $|\alpha|$.

4.1.4 Simulations

In this section simulations are presented to study the effectiveness of the proposed method and to compare it with other methods proposed in the literature. Here, the proposed method is compared with methods based on continuous rotations [31, 46]. In practical applications, it is desired to limit the number of needle rotations since too many rotations may cause tissue damage and trauma by cutting the tissue and by heating produced by needle/tissue friction.

(a)

(b)
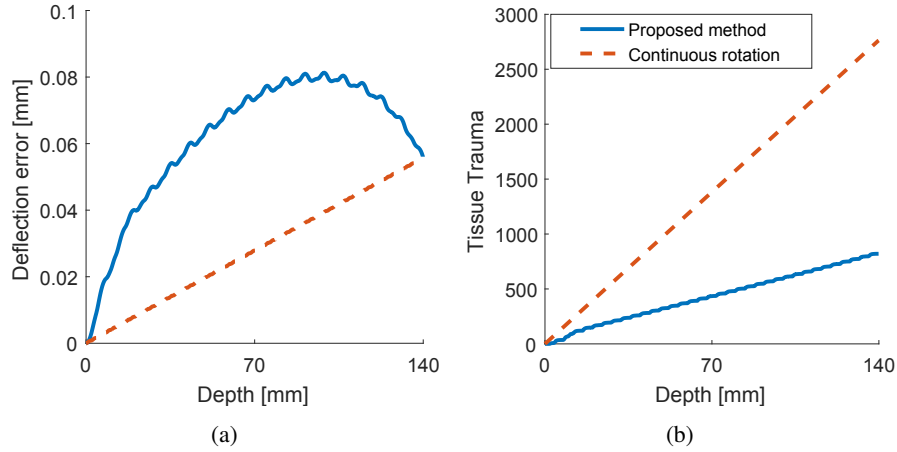
Figure 4.6: Simulation results comparing the deflection and tissue trauma for different methods with the desired trajectory of a straight line. (a): Norm of needle tip deflection. (b): Tissue trauma

This issue has been previously studied in the literature [93, 94]. The tissue trauma can be measured as the heat and energy transferred to the tissue caused by needle rotations. The measure for tissue trauma is defined as

$$\text{Trauma} = \int_0^t u^2 dt \tag{4.23}$$

where t is the insertion time and u is the rotational velocity. The simulations are performed for the adaptive structure proposed in the previous section with an insertion velocity of 2 mm/sec and an insertion depth of 140 mm. The constant rotational velocity for the comparison is selected as 2π rad/sec and the desired performance is to move the needle on a straight line. As a needle rotates with constant velocity, it moves on a helical path whose radius depends on the rotational velocity, faster rotations leading to smaller errors. However, this behavior gives rise to the drilling effect, which causes tissue trauma. In our proposed method, the needle is only rotated when necessary, which is equivalent to making small adjustments to reduce the error in both the x and y directions. The results depicted in Fig. 4.6 show that the proposed method yields a maximum position error of 0.08 mm, which is still negligible, but results in reduced trauma on tissue.

54

4.1.5 Tracking Method

The desired path generated by the planner is the reference input to the control loop that should be followed by the needle tip. The sliding mode controller is then responsible for calculating the angle γ_d to make this tracking happen. The difference between a desired trajectory and a straight line is that the time derivatives of the desired trajectory are not necessarily zero. However, in the constraints derived in section 4.1, it is assumed $\dot{x}_d = \ddot{x}_d = \dot{y}_d = \ddot{y}_d = 0$. In order to apply the same conditions and control strategy to trajectory tracking, it is possible to discretize the desired path by sampling and holding to break the tracking problem into several small regulation problems. In this method, the desired trajectory turns into a set of successive small steps, each of which should be reached by the needle during the discretization sample time. In order to have small errors at the end of each step, a sawtooth wave is applied to the sliding surface parameters b_x and b_y by resetting them at each discretization step to their initial values such that they remain positive all the time. This discretization is the only modification made for the tracking problem and can be performed at the planner/re-planner level.

4.2 Experiments

To verify the accuracy of the proposed controller, the experimental setup shown in Fig. 1.3 is used. In our experiments highly flexible notched needles proposed in [98] with experimentally identified mean deflection radius of curvature of 400 mm are used. The phantom tissue used in these experiments is plastisol, made of 80% liquid plastic and 20% plastic softener (M-F Manufacturing Co., Fort Worth, TX, USA) with an estimated Young's modulus of elasticity of 35 kPa. The position signal obtained by image processing, is filtered to reduce noise and the velocity is found by taking the time derivative of the position signal. Since the needle tip deflection changes are much slower than the noise imposed on the signals, the effects of the filter on the system dynamics can be neglected. The insertions are performed for a constant insertion velocity of $v = 2$ mm/sec. The settling time of the needle axial rotation with the PID controller is about 0.2 sec, which is considered in the update time of the desired value γ_d. The upper bounds α^* and β^* are selected as 0.15 rad. The experiments are performed in two different scenarios, in each of which eight trials were conducted.

In the first scenario, the needle is inserted to the desired depth of 140 mm and aimed to move on a straight line as in a conventional brachytherapy procedure, i.e., $x_d = y_d = 0$. The initial value $b(0)$ is selected to be 80. The results indicate a mean absolute error of 0.54 ± 0.37 and 0.23 ± 0.2 mm and a maximum targeting error of 1.0 and 0.81 mm for the x and y directions, respectively, as summarized in Table 6.1. The needle tip error for different trials as well as the needle tip track for one of the trials are shown in Fig. 4.7 and Fig. 4.8. In the second scenario, the needle is inserted to the target point at a depth of 140 mm and is steered to avoid an obstacle at a depth of a 80 mm. The desired path is obtained using the algorithm introduced in section 3.3.

Here, the path is the reference to the closed-loop system and the controller keeps the needle on the desired path. The path generated by the planner is then discretized by a sample time of 1 sec. The initial values of the sliding surface parameters b_i are selected as 3, which are reset to their initial values every 1 second. From Table 6.1, the mean absolute error of 0.48 ± 0.55 and 0.51 ± 0.61 mm is obtained for the x and y directions, respectively. The maximum targeting error is 1.14 mm for the x direction and 1.03 mm for the y direction. The needle tip error for eight trials and tip position for one of the trials are shown in Fig. 4.7 and Fig. 4.8, respectively. The experimental results show a maximum position error of 1.14 mm.

4.3   Concluding Remarks

In this chapter, a non-model-based control structure for steering beveled-tip needles in soft tissue is presented. In this control scheme, two sliding surfaces are defined to account for the needle tip deflection error in the x, and y directions, as the needle is inserted to reach the desired depth. The controller compensates the positioning errors by performing adjustments of the needle roll angle to reduce the tissue trauma. The convergence of the deflection error is shown using the 3D unicycle equations. The constraints imposed by this convergence analysis are relaxed by using an adaptive-structure controller and rotating the sliding surfaces. From the experiments, the mean absolute and maximum error are 0.5 mm and 1.14 mm, respectively, which are comparable with the results in the literature. The proposed method only uses information about the needle tip position obtained from ultrasound im-

Table 4.1: Summary of the experimental results using the sliding mode controller

Desired Position	Results- x direction				Results-y direction			
	Mean Absolute Error [mm]	Standard deviation (σ)	RMSE [mm]	Max Targeting Error [mm]	Mean Absolute Error [mm]	σ	RMSE [mm]	Max Targeting Error [mm]
1st scenario	0.54	0.37	0.63	1.0	0.23	0.20	0.28	0.81
2nd scenario	0.45	0.52	0.55	1.03	0.44	0.5	0.54	1.03
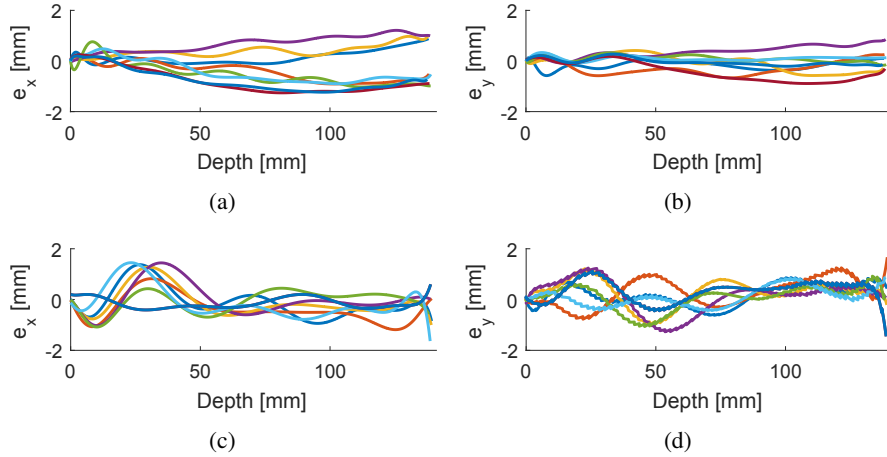
Figure 4.7: Needle tip error for needle insertion in plastisol tissue. (a),(b): show the needle tip error for 8 trials in the x and y directions for moving on a straight line ($x_d = 0$ mm, $y_d = 0$ mm). (c),(d): show the needle tip error for 8 trials in the x and y directions for moving on a desired trajectory.

ages and no information about the needle tip orientation is involved in finding the control action. However, since the needle path depends on the tip orientation, having knowledge about the needle tip pose, i.e., its Cartesian position and orientation, would be helpful for accurate needle steering, although only the Cartesian position of the needle tip can be measured from ultrasound images. In the next chapters, the problem of estimating system states in robot-assisted brachytherapy using state observers and their application in needle steering is studied.
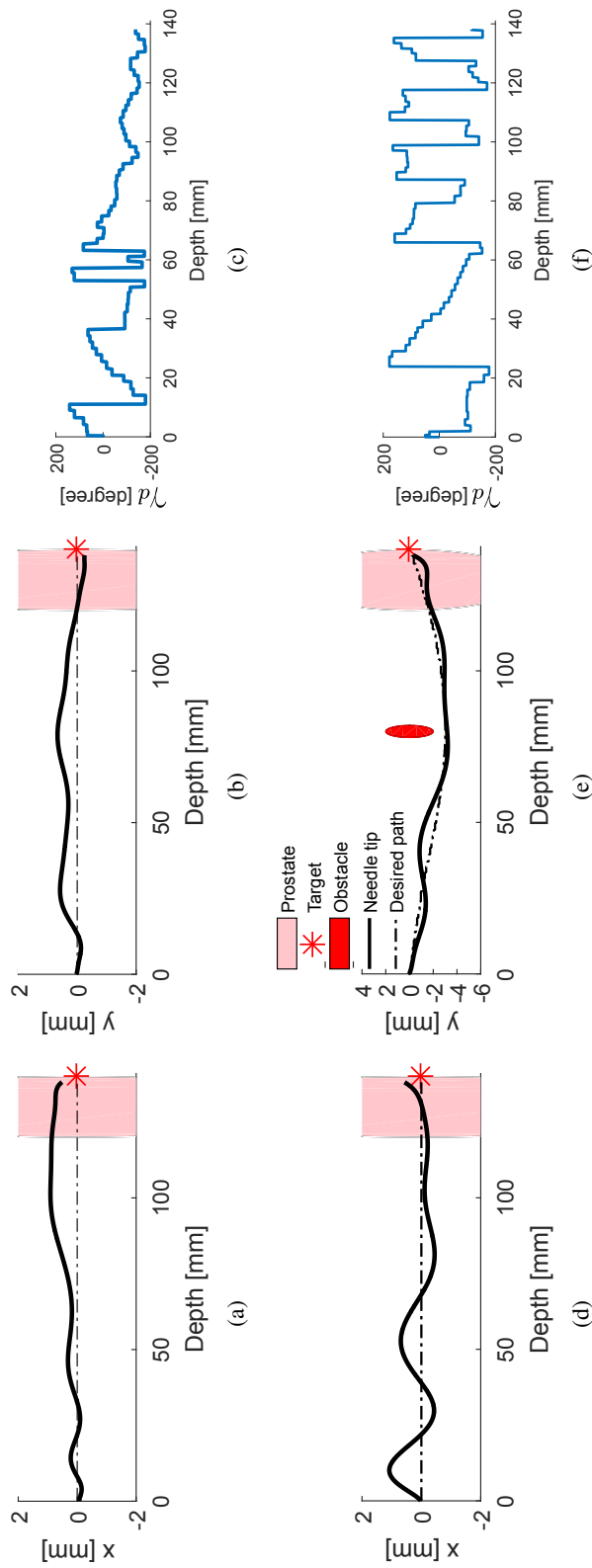
Figure 4.8: Representative results for needle insertion in plastisol tissue for two scenarios: (a),(b),(c): moving on a straight line; (d),(e),(f): moving on a desired trajectory. (a) and (b) show the needle tip position in the x and y directions and (c) is the desired needle roll angle obtained from the sliding mode controller. (d) and (e) show the needle tip position in the x and y directions and (f) is the desired needle roll angle obtained from the sliding mode controller.

Chapter 5

Image-Based Partial Observation of Needle Orientation

Since the needle path depends on the tip orientation, knowing the needle tip pose, i.e., its Cartesian position and orientation, will be helpful for accurate needle steering. The needle tip pose can be measured using different methods; however, these methods should satisfy the clinical requirements. Ultrasound imaging is a low-cost non-invasive imaging modality, which has been widely used in clinical applications. Ultrasound images combined with image processing techniques can be used for measuring the needle tip position; however, due to the small diameter of the needle and the low resolution of the images, the needle tip orientation cannot be measured from the ultrasound images. Moreover, due to the sterilization issues, the use of needle-mounted sensors is not clinically feasible. Alternatively, using mathematical models for the needle-tissue interaction and the measured variables, i.e., the position data, state observers can be employed to get an estimate of the needle tip orientation.

In this chapter, we propose a nonlinear observer that uses Cartesian position measurement data to estimate the orientation of the needle tip as the needle is inserted into the tissue. With certain assumptions and constraints on system states and inputs, the zero convergence of the proposed observer error is shown using Lyapunov-based methods. Both simulations and experiments evaluate its performance.

5.1   Observer Equations

Consider the following transformation:

$$
s = \begin{bmatrix} x \\ \sin\beta \\ -\cos\beta\sin\gamma \end{bmatrix} \tag{5.1}
$$

from which the pitch and yaw angles can be found as

$$\beta = \arcsin(s_2) \tag{5.2a}$$

$$\gamma = atan2(-s_3/\cos\beta, \cos\gamma) \tag{5.2b}$$

where $atan2(a,b)$ is the function that calculates $\arctan(\frac{b}{a})$ taking the sign of both arguments into account. Defining $s_f = \cos\beta\cos\gamma$ and taking time derivative from it we have

$$\dot{s_f} = \frac{d}{dt}(\cos\beta\cos\gamma) = -(\sin\gamma\cos\beta)u = us_3 \tag{5.3}$$

and consequently

$$s_f = \int_0^t us_3(\tau)d\tau \tag{5.4}$$

which can be used to find $\cos\gamma$. Moreover, it is easy to see that $\cos\gamma$ can be found as

$$\cos\gamma = \zeta\frac{\sqrt{1-(s_2^2+s_3^2)}}{\cos\beta} \tag{5.5}$$

where $\zeta = sign(\cos\gamma)$ depends on the bevel orientation. From (1.3) we have $\cos\beta > 0$ and using (5.1) and (5.5), the transformed system equations can be written as

$$\dot{s} = \begin{bmatrix} vsin\beta \\ kv\cos\beta\sin\gamma \\ kv\sin\beta - u\cos\beta\cos\gamma \end{bmatrix} = \begin{bmatrix} vs_2 \\ -kvs_3 \\ kvs_2 - \zeta u\sqrt{1-(s_2^2+s_3^2)} \end{bmatrix} \tag{5.6}$$
$$y = \begin{bmatrix} 1 & 0 & 0 \end{bmatrix}s = x$$

in which the deflection of needle tip in the x direction has been considered as the output and the needle rotation velocity u acts as the input. The system equations can be re-written in the form

$$\dot{s} = As + \phi(u,s) \tag{5.7}$$

with

$$A = \begin{bmatrix} 0 & v & 0 \\ 0 & 0 & -vk \\ 0 & 0 & 0 \end{bmatrix} \tag{5.8a}$$

$$\phi(u,s) = \begin{bmatrix} 0 \\ 0 \\ kvs_2 - u\sqrt{1 - (s_2^2 + s_3^2)} \end{bmatrix} \tag{5.8b}$$

Now consider the following observer [103]

$$\dot{\hat{s}} = A\hat{s} + \phi(u,\hat{s}) + \Delta_\theta L(\hat{y} - y) \tag{5.9}$$

where $L = \begin{bmatrix} L_1 & L_2 & L_3 \end{bmatrix}^T$ is the observer gain, which should be selected such that $A+LC$ is Hurwitz, and

$$\Delta_\theta = diag\{\theta, \theta^2, \theta^3\} \tag{5.10}$$

with $\theta > 1$.

5.1.1 Convergence of the Observer

In this section, it is shown that under certain assumptions and by proper choice of the observer gain, the observation error will tend to zero. To show the convergence of the proposed observer, define the observation error as $e = \Delta_\theta(\hat{s} - s)$. Using the system equation (5.7) and observer equation (5.9), we have

$$\dot{e} = \theta(A + LC)e + \Delta_\theta^{-1}\delta_\phi(u,s) \tag{5.11}$$

with $\delta_{\phi 1}(u,s) = \delta_{\phi 2}(u,s) = 0$ and

$$\delta_{\phi 3}(u,s) = kv(\hat{s}_2 - s_2) \\ + \zeta u(\sqrt{1 - (\hat{s}_2^2 + \hat{s}_3^2)} - \sqrt{1 - (s_2^2 + s_3^2)}) \tag{5.12}$$

If the nonlinear term $\delta_\phi(u, s)$ is a Lipschitz function, i.e. $\exists c > 0$ such that $\|\phi(u,s) - \phi(u,\hat{s})\| \leq c\|s - \hat{s}\|$, where $\|.\|$ denotes the euclidean norm of $\mathbb{R}^n$, for $\theta > 1$, equation (5.9) forms an exponential observer [103]. However, since the function $\sqrt{1 - (s_2^2 + s_3^2)}$ does not satisfy the Lipschitz continuity condition as $(s_2^2 + s_3^2) \rightarrow 1$, using the fact that $|s_i| \leq 1$ $(i = 2, 3)$, assume

$$\sqrt{1 - (s_2^2 + s_3^2)} \geq \epsilon \tag{5.13}$$

due to which (5.12) can be upper bounded as

$$|\delta\phi(3)| \leq \frac{\bar{u}}{2\epsilon}((\hat{s}_2^2 - s_2^2) + (\hat{s}_3^2 - s_3^2)) + kv|\hat{s}_2 - s_2| \tag{5.14}$$

where $\bar{u} > 0$ is the upper bound for the input signal u. (5.14) can be simplified to

$$|\delta\phi| \leq (kv + \frac{\bar{u}}{\epsilon})\|e\| \tag{5.15}$$

Now consider the Lyapunov function

$$V(e) = \frac{1}{2}e^T P e \tag{5.16}$$

with P being a positive definite matrix. Since L is chosen such that $A + LC$ is Hurwitz, then P can be found as the response of the algebraic Lyapunov equation $(A + LC)^T P + P(A + LC) = -I$. We have

$$\dot{V} = -\theta\|e\|^2 + 2e^T P \delta\phi(s, u) \tag{5.17}$$

From (5.15) the above equality can be written as

$$\dot{V} \leq (-\theta + 2\|P\|(\frac{\bar{u}}{\epsilon} + kv))\|e\|^2 \tag{5.18}$$

Choosing $\theta > 2\|P\|(\frac{\bar{u}}{\epsilon} + kv)$ leads to $\dot{V} < 0$.

5.1.2   Assumptions and Constraints

In the previous section, the convergence of the proposed observer was shown for the region obtained from (5.13). However if $\sqrt{1 - (s_2^2 + s_3^2)} \rightarrow 0$, which is equivalent to $|\sin\beta| \rightarrow 1$
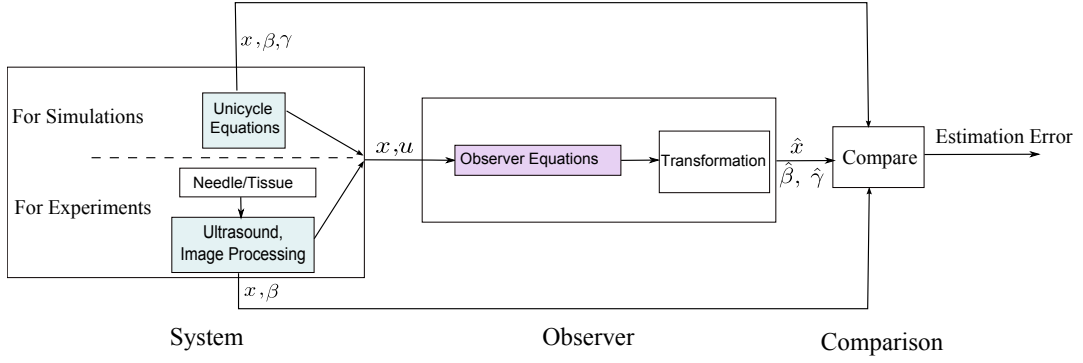
Figure 5.1: Block diagram of the observation system for (a): Simulation, (b): experiments

or $|\sin\gamma| \to 1$, there is no guarantee for convergence of the estimation error at these points as the Lipschitz continuity condition is not satisfied. However if the observer is combined with path planning methods and/or controllers, it is possible to use the proposed observer. The kinematic equations (1.2) are well defined on $\mathcal{U}$ in (1.3). If path planners are employed to steer the needle on a desired path, $\beta = \pm\frac{\pi}{2}$ can be avoided in planning level. On the other hand, since γ is directly related to the input u, it may have any value. Moreover, to have $\cos\gamma > 0$ or $\cos\gamma < 0$, which affects the needle path in the y-direction, the angle γ should pass the critical point $\cos\gamma = 0$, meaning that it is not possible to limit the angle γ to $[-\pi/2, \pi/2]$. Nevertheless, in practice, if the input u is designed such that $\gamma = n\pi/2$ is only a transient via point, i.e. the point that has to be passed to reach other points, and the goal is to keep γ at angles other that $n\pi/2$, then the proposed observer can be used to estimate the angles β and γ and the convergence of the observation error to zero is guaranteed.

5.1.3   Implementation Considerations

According to (5.9), in order to avoid any numerical problems in implementing the observer equations, the term $1 - (\hat{s}_2^2 + \hat{s}_3^2)$ should always be positive. In all simulations in this chapter, in any case that this condition is not satisfied, this term is substituted by zero.

5.2 Evaluation

5.2.1 Simulations

In this section, simulation results are presented to evaluate the performance of the proposed observer. As shown in Fig. 5.1 The system and observer are simulated using the kinematic unicycle equations (1.2) and observer equations (5.9), respectively. The simulations are performed for the insertion velocity $v = 2$ mm/sec and the needle path curvature $k = 0.0019$ mm^{-1} for system and $k = 0.002\ mm^{-1}$ for the observer to simulate 5% uncertainty for this parameter. The inputs to the observer are the input signal u (needle rotation velocity) and the needle tip position in the x direction and the outputs are transformed system states $\hat{s}$, from which the angles β and γ can be calculated using (5.2). In simulations, the value of γ is controlled to have different values other than $n\pi/2$. The observer gain is selected to be $L = [-100 \quad -1.05 \ 1.37]$ to make the matrix $A + LC$ Hurwitz $\theta = 6\pi \times 10^4$. The initial values for x and β is considered to be zero and for γ is $3°$. The results are shown in Fig. 5.2. The results show a maximum estimation error of 10^{-14} mm and 10^{-7} rad for x and β and a maximum estimation error of 0.05 rad for γ. The results show the convergence of the proposed observer for the considered region.

5.2.2 Experiments

This section shows the results from implementing the proposed observer in real-time for estimating the angles β and γ as the needle is inserted into phantom tissue. In these experiments the needle base's angle is measured by an encoders whose time derivative is considered as the input signal u in (1.2) and the control algorithm proposed in chapter 2 is employed in which the main goal is compensating for the needle deflection in y direction by $180°$ axial rotations at appropriate depths. This method only requires the needle deflection in the y direction. The needle path curvature is selected as $0.002\ mm^{-1}$ The insertion velocity in the experiments is 2 mm/sec and the maximum insertion depth is 100 mm. The experiments are performed 6 times. The observer gain L is identical to the values used in the simulations and $\theta = 10^6$.

Table 5.1: Summary of the experimental results using the proposed observer

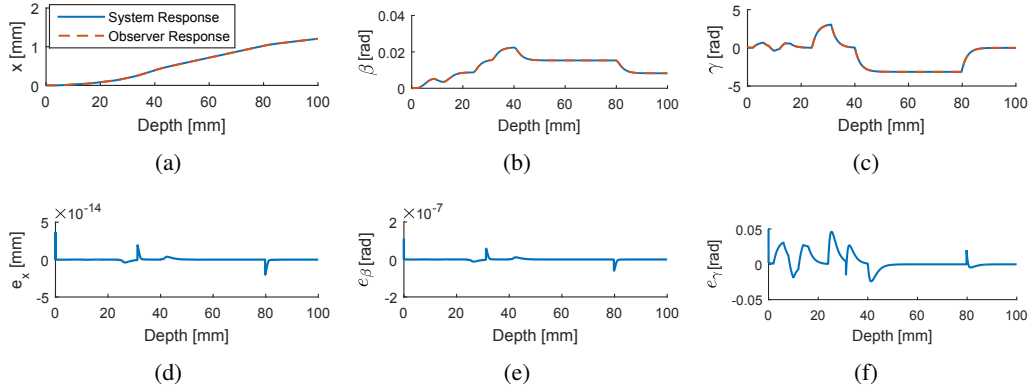|	Average Absolute Estimation Error	MRSE	Standard Deviationσ
e_x[mm]	2e-14	5e-13	5e-13
e_β[rad]	0.02	0.04	0.037

Figure 5.2:   Simulation results using unicycle equations and the proposed observer. (a),(b),(c): the system and observer response for x, β and γ. (d),(e),(f): estimation error

The evaluation is performed by comparing the estimated variables with the real values obtained from experiments. As stated before, only the position of the needle tip can be measured from 2D ultrasound images and the angles β and γ can not be measured in real-time. However, the angle β can be considered as the angle between the Z axis of the moving frame $\{B\}$ with respect to the z axis of the fixed frame $\{A\}$ in $x - z$ plane, which can be found by off-line curve fitting on position data. However, there is no way for measuring the angle γ from 2D ultrasound images. The results are shown in Fig. 5.3. This figure represents the estimation error for position in the x direction and the the angle β for 6 trials. In this figure, to compensate for noisy position measurements, polynomials are fitted to the position data and the real value β is calculated at each insertion depth. The observer response is also smoothed by fitting polynomials to the estimated value $\hat{\beta}$, as shown in Fig. 5.3 . The results are summarized in Table 5.1, which shows the performance of the observer in estimating the position in the x direction and the angle β representing average errors of 2×10^{-14} mm and 0.02 rad, respectively. Due to impossibility of measuring the real value of the angle γ using the current equipment, this value is not shown in the figures.
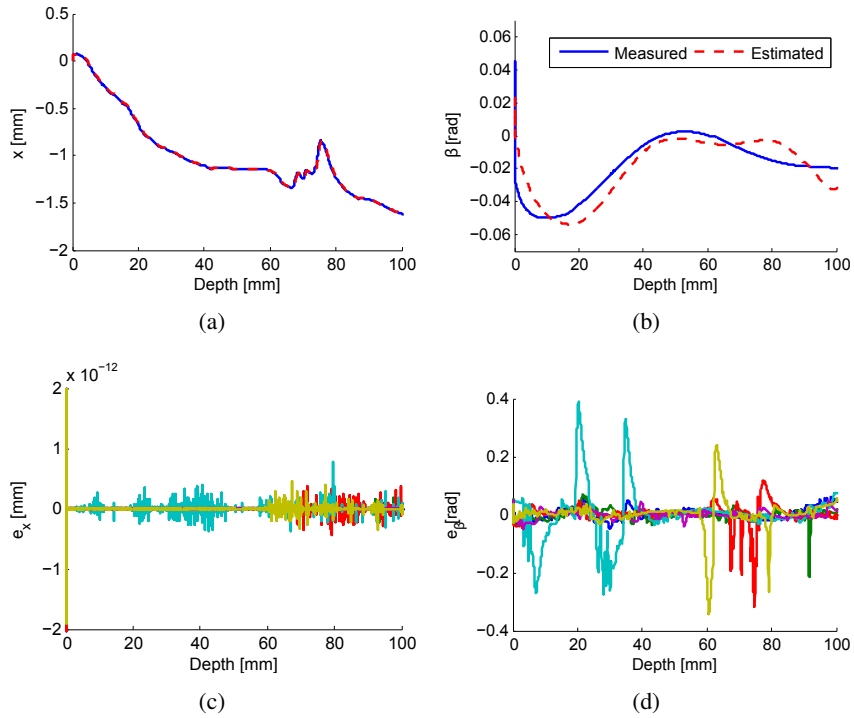
Figure 5.3: Experimental results for needle insertion and observer state estimation for gelatin tissue and insertion velocity of 2 mm/sec and insertion depth of 100 mm . (a) demonstrates the estimated position in x direction as well as the real values for one of the trials. (b) demonstrate the polynomial fitted values of estimated and real value of pitch angle for one of the trials. (c),(d), show the estimation error for the trials.

5.3   Concluding Remarks

In this chapter, we have presented an observer for partially estimating the needle tip orientation during insertion. In this method, nonlinear transformations are applied on a 3D unicycle model of the needle, based on the observer equations. The inputs to the observer are the input signal u (needle rotation velocity) and the position measurements in the x direction which is obtained from 2D ultrasound images. Due to the singularities imposed by the nonlinear transformations, the convergence of the observer is shown under some assumptions and constraints. The proposed observer in this chapter is able to estimate the needle tip orientation in terms of β and γ. The yaw angle α is not estimated using this structure. Moreover, in this formulation, the critical points limit the observer to some extent. In the next chapter an approximate high gain observer is introduced, which guarantees the boundedness of the estimation error and relaxes limited workspace constraint. The designed observer is combined with a controller and used in a feedback control loop for needle steering.

Chapter 6

Image-Guided Observer-Based Control for Needle Steering

In the previous chapter, we designed a nonlinear observer for partial estimation of the needle tip orientation, where the convergence and stability of the observer were only guaranteed for a limited workspace. In this chapter, an approximate high-gain observer is used to estimate the rotation matrix representing the needle tip orientation. The proposed observer is shown to be stable even at singularities, which guarantees the boundedness of the observation error. Moreover, the upper bound of the error can be obtained as a function of the observer gain, system parameters and the input upper bound. It is shown that without any state transformations the system equations can be written as three subsystems including linear terms. Although these equations are simple, they fail to meet the Lipschitz continuity condition, which makes the observer design more challenging. To overcome this limitation, the method introduced in [104], which deals with non-Lipschitz systems is used. Compared to other observers developed in this context [47, 5], the proposed observer does not impose any limitation on the operation region as it deals with the singularities. However, this method can only guarantee the boundedness of the observation error, i.e., the difference between the actual value and the estimated value of the needle tip orientation. The observer gain can be appropriately selected to achieve the desired error bound. When combined with a closed-loop controller, this is sufficient for satisfactory needle tip positioning performance.

Remembering the primary goal of designing an observer, the observer/controller combination, is designed such that the stability and performance of both the controller and the observer are guaranteed. As with any observer, a requirement of the proposed observer is to have a bounded input signal for the system, which is equivalent to the boundedness of the control input in a feedback configuration. This leads to the idea of limiting the control signal before applying to the system and designing the controller accordingly. This assumption is not very limiting as in practice eventually the actuators saturate, and the magnitude of the control signal has some upper bound. Nevertheless, saturation should be considered in the

controller design to ensure the stability and performance of the observer-based controller. The observation error and the effects of the introduced saturation on the control signal are considered as an additive uncertainty. Taking the uncertainty into account, a parametrized state feedback controller is designed using pole placement method and is analyzed using LMI optimizations to find the region of attraction for the tracking error.

6.1   Needle Orientation Observer

From (1.2a), it is easy to see that the vector $\dot{\boldsymbol{p}}$ is the last column of matrix R multiplied by v. By expanding (1.2b), the second column of R can also be presented by second time derivative of the position vector multiplied by $1/kv^2$. Moreover, from the orthogonality property of the rotation matrix, the elements $r_{i1}, i = 1, 2, 3$, can be written as

$$r_{i1} = \pm\sqrt{1 - (r_{i2}^2 + r_{i3}^2)} \tag{6.1}$$

Assuming the needle is inserted continuously in the Z direction without retractions, the needle position in 3D space can be projected into $X - Z$ and $Y - Z$ planes, forming 2D maps of needle deflection. Using (1.2) and defining the new vector $\boldsymbol{s_i} = \begin{bmatrix} \boldsymbol{p}(i) & vr_{i3} & (-kv^2)r_{i2} \end{bmatrix}$, the planar motion of the needle in the $X - Z$ plane for $i = 1$ and in the $Y - Z$ plane for $i = 2$ can be expressed in state space as

$$\dot{\boldsymbol{s_i}} = A\boldsymbol{s_i} + B\phi(\boldsymbol{s_i}) \tag{6.2a}$$

$$y = C\boldsymbol{s_i} \tag{6.2b}$$

with

$$A = \begin{bmatrix} 0 & 1 & 0 \\ 0 & 0 & 1 \\ 0 & 0 & 0 \end{bmatrix} \tag{6.3a}$$

$$B = \begin{bmatrix} 0 & 0 & 1 \end{bmatrix}^T \tag{6.3b}$$

$$C = \begin{bmatrix} 1 & 0 & 0 \end{bmatrix} \tag{6.3c}$$

$$\phi(\boldsymbol{s_i}) = \underbrace{-(kv)^2 s_{i2}}_{\phi_L} \pm \underbrace{(kv^2)\sqrt{1 - ((s_{i2}/v)^2 + (s_{i3}/kv^2)^2)}\, u}_{\phi_\Delta} \tag{6.3d}$$

Since the equations representing the planar motion have the same form for $i = 1, 2$, in the sequel, the index i is omitted for simplicity. The new state vector $\boldsymbol{s}$ is related to the position and orientation of the needle tip. Whereas s_1 is directly measured from images, s_2 and s_3 need to be observed. The following section is devoted to observer design process for the 2D case because, as explained above, the 3D observation problem can be resolved to two 2D problems. Later in Section 6.2, a controller is designed.

For the observable system (6.2)-(6.3), the main challenge in designing a state observer for (6.2) is the nonlinear term $\phi(\boldsymbol{s})$ as the function $\phi_\Delta = \sqrt{1 - ((s_2/v)^2 + (s_3/kv^2)^2)}$ is both continuous and bounded but does not satisfy the Lipschitz continuity condition when $((s_2/v)^2 + (s_3/kv^2)^2) \rightarrow 1$. To deal with this constraint, the following the high-gain approximate observer is used [104]

$$\dot{\hat{\boldsymbol{s}}} = A\hat{\boldsymbol{s}} + B\phi(\hat{\boldsymbol{s}}) + \frac{1}{2}M_\theta^{-1}C^T (y - C\hat{\boldsymbol{s}}) \tag{6.4a}$$

$$\hat{y} = C\hat{\boldsymbol{s}} \tag{6.4b}$$

where A, B, C and ϕ are defined in (6.3) and $\hat{\boldsymbol{s}}$ is the estimated state vector. M_θ is a positive-definite matrix that satisfies the algebraic Lyapunov equation

$$-\theta M_\theta - A^T M_\theta - M_\theta A + C^T C = 0 \tag{6.5}$$

with $\theta > 1$. Defining the estimation error as $e = \hat{s} - s$ and the Lyapunov function $V(e) = e^T M_\theta e$, the time derivative of $V(e)$ is obtained as

$$\dot{V}(e) = -\theta e^T M_\theta e + 2e^T M_\theta \left(\phi(u, \hat{s}) - \phi(u, s)\right) \tag{6.6}$$

Since ϕ_L in (6.3) is a Lipschitz function with some Lipschitz constant ℓ and the non-Lipschitz term involving ϕ_Δ to be bounded by some $\sup |u\phi_\Delta| = \delta/2$, in [104] it is shown that the observation error is upper-bounded as

$$\|e\| \leq \theta^2 \left(\frac{c_2}{c_1}\right) \|e(0)\| \exp(-\mu t) + \frac{\delta \bar{M}}{c_1 \mu} \left(1 - \exp(-\mu t)\right) \tag{6.7}$$

In this equation, $c_1 = \sqrt{|\lambda_{min}(M_1)|}$, $c_2 = \sqrt{|\lambda_{max}(M_1)|}$, in which λ denotes the eigenvalue of the matrix and $\bar{M} = \sqrt{M_{1_{3,3}}}$, where M_1 is the solution of (6.5) for $\theta = 1$. Also, $\mu = \frac{1}{2}\theta - (\ell/c_1)\bar{M}$ and θ is chosen such that $\mu > 0$. In this equation, the first term exponentially approaches zero; however, the second term increases exponentially to the value $\delta\bar{M}/c_1\mu$. Therefore, there exists some $T \geq 0$ such that the observation error is upper bounded by

$$\|e(t)\| \leq \bar{\beta} \frac{\delta \bar{M}}{c_1 \mu}, \quad t \geq T \tag{6.8}$$

in which $\bar{\beta}$ is slightly greater than one.

6.2 Controller

6.2.1 Controller Structure

In this section, the observer introduced in the previous section is combined with a controller to control the needle tip position in a plane. As stated in the previous section, with the assumption of bounded input signal u, the designed observer ensures the boundedness of the estimation error. In this section, the designed controller is a nonlinear state feedback. By redefining the nonlinear term $\phi(s) = \Omega$, (6.2) turns to a linear system with Ω as its input. Using this definition the control input u is found by

$$u = \frac{\Omega - \phi_L}{\phi_\Delta} \tag{6.9}$$

Remark 1. *The above equation can be used for finding the control signal u when $\phi_\Delta \neq 0$. However, if $\phi_\Delta \to 0$, using (6.9) is not practical as it will yield an unbounded control signal. To overcome this problem, ϕ_Δ can be replaced by ϕ'_Δ defined as*

$$\phi'_\Delta = \begin{cases} \phi_\Delta & |\phi_\Delta| > \phi_0 \\ \phi_0 & |\phi_\Delta| \leq \phi_0 \end{cases} \tag{6.10}$$

where ϕ_0 is a small positive number.

If Ω is bounded, (6.10) ensures the control signal u is bounded. In this case, the closed-loop system equation can be written as

$$\dot{s} = As + B\frac{\phi_\Delta}{\hat{\phi}'_\Delta}\Omega + B(\hat{\phi}_L - \frac{\phi_\Delta\phi_L}{\hat{\phi}'_\Delta}) \tag{6.11}$$

where $(\hat{\cdot})$ represents evaluation at estimated values $\hat{s}$. Assuming $\frac{\phi_\Delta}{\hat{\phi}'_\Delta} \to 1$, the above equation can be written as

$$\dot{s} = As + B\bar{\Omega}\sigma(\Omega/\bar{\Omega}) + w(t) \tag{6.12}$$

where $\bar{\Omega} > 0$ is the upper bound of Ω. The saturation function is defined as $\sigma(t) = sign(t)min(1, |t|)$ and $w(t)$ is a disturbance term.

Remark 2. *Since the system state vector s is estimated using the observer introduced in the previous chapter, as long as the input signal to the system is bounded, the estimation error remains bounded. Remembering that the columns of a rotation matrix are unit vectors, using the assumptions $|\hat{s}_2| \leq 1+\bar{e}$, where $\bar{e}$ is the upper bound for the observation error, the upper bound on the disturbance term can be found as*

$$|w(t)| \leq (kv)^2(1 + \bar{e}) \tag{6.13}$$

From here, the goal is to design the state feedback control law $\Omega = F\hat{s}$ in the presence of the saturation function and the bounded disturbance $w(t)$, from which the control signal u can be found as

$$u = \frac{F\hat{s} + (kv)^2\hat{s}_2}{\hat{\phi}'_\Delta} \tag{6.14}$$

6.2.2   Controller Design

The state feedback gain F should be designed to ensure the convergence of the response in the presence of the input saturation. The following notations are used in the sequel to re-formulate the design problem [105].

Notation. *Denoting the system trajectories starting from initial condition x_0 by $\psi(t, x_0)$, the domain of attraction of the origin (DOA) is defined as $\mathcal{J} = \{x_0 \in \mathbf{R}^3 : \lim_{t \to \infty} \psi(t, x_0) = 0\}$. If $w(t) = 0$, an ellipsoid $\mathcal{E}(P, \rho) = \{x \in \mathbf{R}^3 : x^T P x \leq \rho\}$ with P being a positive-definite matrix is contractively invariant if the time derivative of the Lyapunov function $V(x) = x^T P x$ is negative-definite for all $x \in \mathcal{E}(P, \rho)$. If $w(t) \neq 0$, an ellipsoid $\mathcal{E}(P, \rho)$ is called strictly invariant if the time derivative of the Lyapunov function $V(x) = x^T P x$ is negative-definite for all $w(t)$ with $|w(t)| < 1$ and all $x \in \partial \mathcal{E}(P, \rho)$, the boundary of $\mathcal{E}(P, \rho)$. A set is called invariant if all the trajectories starting from this set remain inside it for all times, regardless of the disturbance $w(t)$.*

Using the above notations, when $w(t) = 0$, the convergence of the system can be expressed as ensuring for the desired set, all the trajectories starting from this set converge to zero. The problem is then defined as designing the state feedback gain F such that a pre-defined set resides in the DOA. Moreover, to have some control over the convergence rate, the controller gain F is designed using pole placement method. For simplicity, the feedback gain F is parameterized by a control design parameter ε to shift the system poles by -2ε to the left. This leads to having the state feedback gain F_ε elements as polynomials in ε. The desired state feedback gain F_ϵ, which places the eigenvalues of A at -2ϵ can be found as

$$F_\epsilon = \begin{bmatrix} -8\epsilon^3 & -12\epsilon^2 & -6\epsilon \end{bmatrix} \tag{6.15}$$

Since in reality $w(t) \neq 0$, the state feedback control gain should be designed to ensure disturbance rejection. The problem here will be to ensure that for the designed state feedback gain, there exist two invariant sets $\mathcal{E}(P, \rho_1)$ and $\mathcal{E}(P, \rho_2)$ with $\rho_1 < \rho_2$ and ρ_1 small enough such that the system trajectories starting from $\mathcal{E}(P, \rho_2)$ enter the smaller invariant set $\mathcal{E}(P, \rho_1)$.

Lemma. *[105] Given two ellipsoids $\mathcal{E}(P, \rho_1)$ and $\mathcal{E}(P, \rho_2)$ with $\rho_2 > \rho_1 > 0$, if there exist $H_1, H_2 \in \mathbf{R}^n$ and a positive number η such that*

$$(A + BM(F, H_i))^T P + P(A + BM(F, H_i))$$
$$+\frac{1}{\eta}PEE^T P + \frac{\eta}{\rho_i}P < 0 \qquad i = 1, 2 \qquad (6.16)$$

and $\mathcal{E}(P, \rho_i) \subset \mathcal{L}(H_i)$, where $M(F, H) = \{H, F\}$ and $\mathcal{L}(H) = \{x \in \mathbf{R}^n : |hx| \leq 1\}$ then for every $\rho \in [\rho_1, \rho_2]$, there exist an H such that (6.16) is satisfied and $\mathcal{E}(P, \rho) \subset \mathcal{L}(H)$ which is equivalent to $\mathcal{E}(P, \rho)$ being strictly invariant.

In order to guarantee that the designed controller is convergent in the presence of non-zero disturbance, it is only required to find two invariant ellipsoids $\mathcal{E}(P, \rho_1)$ and $\mathcal{E}(P, \rho_2)$ with $\rho_1 < \rho_2$ and ρ_1 small enough satisfying the conditions of the lemma. This can be expressed as the following optimization problem with LMI constraints [105]:

$$\inf_{Q>0, g_1, g_2} \delta \qquad (6.17a)$$

$$s.t. \ (a) \ \begin{bmatrix} X_{R2} & I \\ * & Q \end{bmatrix} \geq 0 \qquad (6.17b)$$

$$(b) \ \begin{bmatrix} Q/\rho_1 & Q \\ * & \delta X_{R1} \end{bmatrix} \geq 0 \qquad (6.17c)$$

$$(c) \ \begin{array}{l} \rho_i Q A^T + \rho_i A Q + M(\rho_i F Q_i, G)^T B^T \\ +BM(\rho_i F Q, G) + \frac{\rho_i}{\eta}EE^T + \frac{\eta}{\rho_i}Q_i < 0 \end{array} \qquad (6.17d)$$

$$(d) \ \begin{bmatrix} 1 & g_i \\ * & \rho_i Q \end{bmatrix} \geq 0 \qquad (6.17e)$$

where $i = 1, 2$, $Q_1 = \frac{\rho_1}{\rho_2}Q$ and $Q_2 = \rho_2 Q$. X_{R2} and X_{R1} are estimations of the DOA and the guaranteed convergence area, respectively. For simplicity and in order to have a convex optimization, it is possible to assume $\rho_2 = 1$ and fix ρ_1 and η. Changing ρ_1 from 0 to 1 and η from 0 to ∞, the infimum δ^* can be found. From this optimization, the matrix P defining the two ellipsoids can be found by $P = Q^{-1}$.

6.3 Evaluation

6.3.1 Controller Implementation

According to the rotational nature of the system, the closed-loop behavior of the system is different from usual control problems causing the designed controller not working properly. In a usual state feedback control loop, larger errors lead to a larger control signal to put the maximum effort to compensate the error. Here, since the system states, i.e., velocity and acceleration, are related to the rotation matrix entries, their maximum and minimum are defined in a full 2π rotation, and any excessive 2π rotations cause the states to oscillate between their maximum and minimum values. To compensate this, the rotations should be limited to 2π, and large control inputs should be interpreted as maximum effort or the maximum acceleration. In the planar case, if the needle is rotated by $180°$, the bevel and consequently the needle path is flipped. This can also be seen from the $\pm$ sign in (6.3). From here it can be seen that to apply the maximum effort, the bevel should be kept in one half-plane. This can be done by keeping the needle base angle θ_b in one half-plane by multiplying the control input u by $sgn(\cos(\theta_b))$. Whenever the bevel passes one half-plane, u is reversed to bring it back. Also, the chattering caused by the sign function can be reduced by replacing this function with a hysteresis block.

6.3.2 Simulation

The block diagram of the system and the proposed observer is shown in Fig. 6.1. The simulations are performed in Matlab/Simulink for the constant insertion velocity of 2 mm/sec and the curvature of 0.0014 mm^{-1}, however, the value of the curvature used in the observer equations is considered as 0.002 mm^{-1} to simulate the uncertainty of 5% in the value of this parameter. The upper bound for the rotational velocity u is selected to be $\bar{u} = 3\pi$. Using these values the observer parameter θ is selected as 15 for which using (6.8), the upper bound of error norm is obtained as 0.03. In a real application, there might be a difference between the initial needle tip position and the observer initial values. This can also be true for the needle base angle, as the needle can be inserted with an arbitrary initial bevel orien-
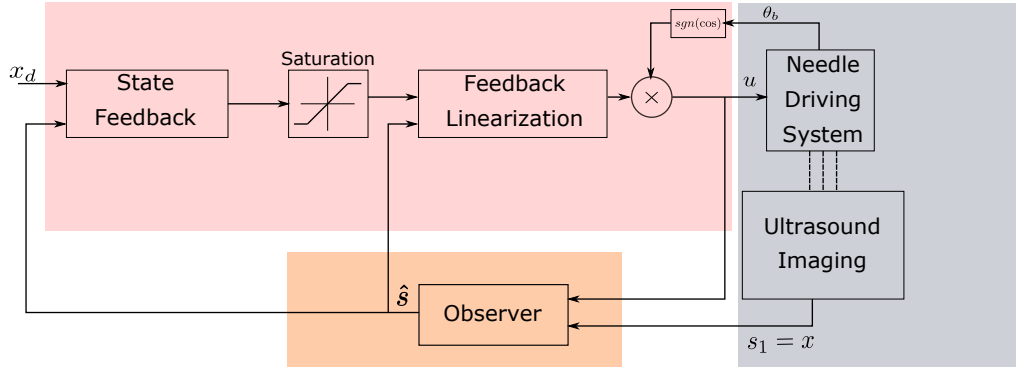
Figure 6.1: The block diagram of the observer/controller loop.
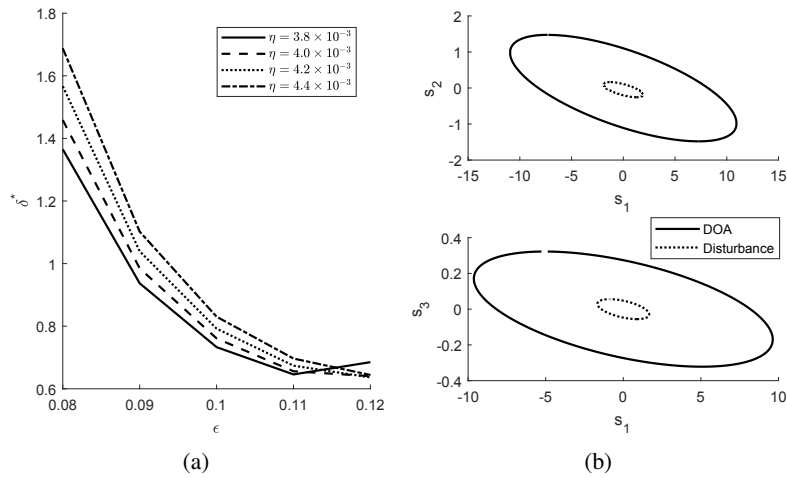
Figure 6.2: State feedback design and its effect on DOA. (a): The effect of different values of ε on δ^* for different values of η. (b): The 2D projection of the DOA and the guaranteed disturbance rejection area for $\varepsilon = 0.11$.

tation, however, since there will are initial bending in the needle shaft, the initial condition is selected as $\boldsymbol{s}(0) = \begin{bmatrix} 5 & 0 & 0.001 \end{bmatrix}$.

To find the state feedback gain F and the guaranteed DOA and the disturbance rejection area, ρ_1 is fixed to 0.03. F is found for different values of ε and the optimization (6.17) is solved for $X_{R1} = I_{3\times3}$, $X_{R2} = diag(0.1, 1, 50)$ and different values of η such that the LMI constraints are feasible. The results are shown in Fig. 6.2(a). The value of ε which gives the minimum value of δ^* is selected for finding the controller gain. Fig. 6.2(b) also represents the guaranteed DOA and the disturbance rejection area. It should be noted that these results show the conservative guaranteed convergence region.

(a)   (b)   (c)

Figure 6.3: The simulation results for $\varepsilon = 0.11$, the desired deflection $x_d = 0$ and the initial condition $s_1(0) = 5$ mm, $s_2(0) = 0$ mm/sec and $s_3(0) = 0.001$ mm/sec^2
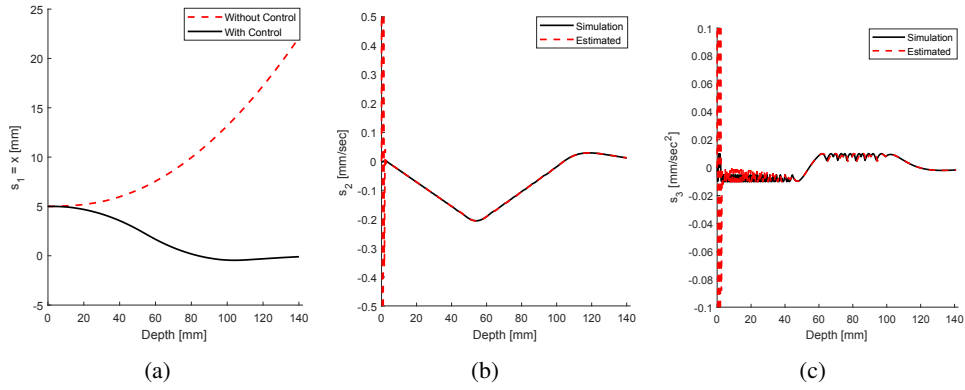
6.3.3 Experiments

To evaluate the performance of the proposed method experiments are performed at constant insertion velocity of 2 mm/sec and the insertion depth of 120 mm for eight trials and two different scenarios. In the first scenario, it is desired to keep the needle deflection equal to zero, which is equivalent to holding the needle in one plane. In the second scenario, the needle is steered to reach the desired deflection of 3 mm, which can be interpreted as compensating the initial insertion error. Both scenarios are implemented using two different tissues. The first tissue is plastisol phantom tissue, which is made of 80% liquid plastic and 20% plastic softner (M-F Manufacturing Co., Fort Worth, TX, USA) with Young's modulus of elasticity of 35 kPa. Both scenarios are also implemented on the biological tissue (beef) embedded into 15% gelatin mixture to simulate a 2-layer non-homogeneous tissue. Moreover, since the position data obtained from ultrasound images are noisy, the position data is filtered before applying to the observer.

The results are shown in Fig. 6.4(a)-6.4(l). These figures show the planar deflection error for eight different trials as well as the real needle position, the estimated position and the needle base angle for one of the trials. Though other states estimated by the observer are used in calculating the control signal, the responses are not shown here as there are no ground truth measurements available for comparison. The summary of the results is shown in table 6.1. As the results show, the mean final deflection error and the maximum final error are 0.73 mm and 1.24 mm, respectively, which are less than 2 mm.
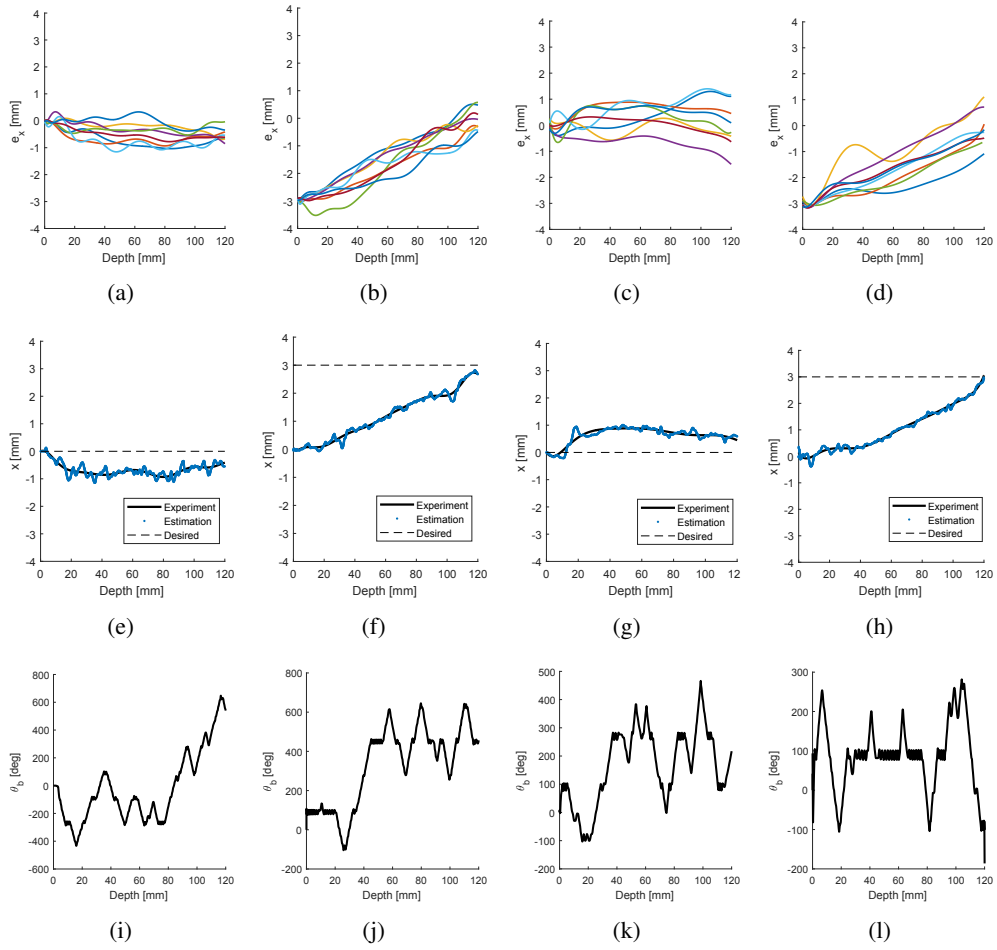
Figure 6.4: Experimental results using the proposed observer/controller for insertion velocity of 2 mm and insertion depth of 120 mm in different tissues and different scenarios. (a), (e), (i): results for inserting the needle into phantom tissue with $x_d = 0$ mm, representing deflection error for different trials, one of the trials and the needle base angle, respectively. (b), (f), (j): results for inserting the needle into phantom tissue with $x_d = 3$ mm, representing deflection error for different trials, one of the trials and the needle base angle, respectively. (c), (g), (k): results for inserting the needle into phantom tissue with $x_d = 0$ mm, representing deflection error for different trials, one of the trials and the needle base angle, respectively. (d), (h), (l): results for inserting the needle into phantom tissue with $x_d = 3$ mm, representing deflection error for different trials, one of the trials and the needle base angle, respectively.

Table 6.1: Summary of the experimental results using the proposed observer/controller

Tissue	x_d [mm]	Mean Absolute Error [mm]	σ	RMSE	Mean Final Error [mm]	Max Final Error [mm]
Phantom	0	0.27	0.44	0.5	0.49	0.71
Tissue	3	1.58	1.05	1.8	0.36	0.99
Biological Tissue	0	0.51	0.43	0.62	0.73	1.24
	3	1.6	1.01	1.9	0.53	1.22

6.4 Concluding Remarks

In this work, 3D unicycle needle equations are used, and it is shown that without any change in the variables, the equations represent partially linear sets of equations, which incorporate both position and orientation data. A high gain observer is designed to deal with the non-Lipschitz property of the equations and estimate the needle tip pose. Using LMI optimizations, the controller is designed to compensate for the out of plane motions. The performance of the proposed observer/controller combination is verified using simulations and experiments for different scenarios. Further developments are required to extend this structure to 3D needle steering. However, it should be noted that 3D unicycle model used in designing the observer is a very simple model that ignores the effects of the needle/tissue interaction forces. Further studies are required to investigate the effectiveness of this model in designing observers.

Chapter 7

Conclusions and Future Works

This thesis proposed and validated the feasibility of different control strategies in steering flexible needles in soft tissue. From the control perspective, the main challenges in designing the controller for needle/tissue system arise from the under-actuation property and the nonholonomic constraints imposed on the needle kinematics. In this work, we proposed different control strategies to deal with these challenges as well as the uncertainties and measurement limitations. In Chapter 2 a 2D control strategy is proposed to steer the needle toward fixed points in soft tissue. Two possible bevel orientations ($0°$ and $180°$) are considered for the needle, which lead to a switching control system with two modes. The controller is a sliding-based method which is supplied with the needle deflection error obtained from ultrasound images and switches the system to the proper mode for reducing the targeting error. The constraints on switching parameters are derived using kinematic unicycle equations for the needle to ensure the stability of the system and convergence of the error. Experiments are performed on phantom tissues and biological tissue using the experimental setup.

In Chapter 3, we extended the 2D switching structure to the 3D environment. In this chapter, the model-averaging technique is used to provide a new formulation, in which the 3D needle equations are divided into two subsystems, representing the in- and out-of-plane motions. Each subsystem is considered as a planar switching system with two modes determining the two possible bevel orientations which are $180°$ apart. Assuming the switching between the two modes is performed according to some duty cycle in a PWM framework, the performance of each subsystem is approximated with the averaged subsystem in the PWM period. Each averaged subsystem has its virtual input, for which controllers can be designed. The virtual inputs are used to find the duty cycle for each subsystem. A switching pattern is represented using the duty cycle of both subsystems to steer the needle on the desired path.

However, since the method proposed in Chapter 3 is based on the PWM switching, in Chapter 4 a sliding mode controller is proposed to find the desired value of the needle base angle to reduce the number of rotations and the tissue trauma. In this method, for each subsystem, a sliding surface is defined, and the two sliding surfaces are combined to find the

desired needle base angle. The proposed structure improves the number of rotations and the tissue trauma by making small adjustments at the needle base.

The methods proposed in the previous chapters use only the position data obtained from ultrasound images. However, since the path traveled by the needle depends on the needle tip orientation, having information about the needle tip orientation will be helpful in the controller design process. Due to the small diameter of the needle and the low resolution of the images, it is not possible to retrieve the orientation information from the ultrasound images. In this work, this problem is dealt with by using state observers. In Chapter 5, an observer is proposed for partially estimating the needle tip orientation during insertion. In this method, nonlinear transformations are applied on a 3D unicycle model. The inputs to the observer are the input signal u (needle rotation velocity) and the position measurements in the x direction which are obtained from 2D ultrasound images. The convergence of the observer is shown under some assumptions and constraints, and the evaluation of the observer is performed using simulations and experiments. In Chapter 6, using the coordinate-free 3D representation of the needle equations, it is shown that without any state transformations the system equations can be written as three subsystems including linear terms. Using these equations, the high gain observer designed in this chapter guarantees the boundedness of the estimation error. The observer is combined with a controller, which accounts for constraints imposed by the observer and guarantees the stability of the controller/observer combination.

The goal in all methods above is to improve the needle tip positioning. This improvement is defined as reducing the 5 mm positioning error obtained from manual insertions to a maximum value of 2 mm, which is the size of the smallest lesion detectable in the ultrasound images. In this work, error compensation is considered in either 2D or 3D environments. The methods proposed in Chapter 2 and Chapter 6 deal with 2D error compensation and the methods proposed in Chapter 3 and Chapter 4 represent 3D needle steering. The errors obtained from all these methods are less than 2 mm, which are in the same order of the error in other methods proposed in the literature, like [102], in which the final targeting error is 1.08 mm and 1.3 mm in [46]. Besides, considering the characteristics of the controllers, the methods proposed in Chapters 2 and 4 are non-model-based controllers, which do not depend on the system's equation, whereas the methods in Chapters 3 and 6 are based on

the system's model. Moreover, the switching-based methods in Chapters 2 and 3 may cause more trauma on the tissue compared to the other methods in Chapters 4 and 6.

In this report, we presented a fully-automated control structure; however, it is always possible to involve a clinician during the operation. The automated needle insertion experiments in this thesis are only meant for repeatability of the trials. There is no reason the proposed method cannot be used in robot-assisted procedures where the control action in the steering algorithm is the axial needle rotation while the other degree of freedom of the system, which is the insertion velocity, can be commanded directly by the clinician. In other words, the steering algorithm is only there to find and implement the best rotations as the clinician performs the insertion.

Moreover, in this work, a modified kinematic bicycle model is developed for better estimating the needle tip defection in soft tissue. The proposed model adds new parameters to the conventional bicycle model to account for the effect of variable tissue stiffness on the needle path. This alleviates the assumption made in the bicycle model that the tissue is stiff relative to the needle. When this assumption is violated, the tissue compression forces caused by needle deflection cause the needle path to deviate from a constant curvature path as predicted by the conventional bicycle model. To account for this, the back wheel of the bicycle is replaced in our work with an omnidirectional wheel enabling us to add correction terms to the bicycle equations.

7.0.1 Future Work

The proposed methods can be further expanded to have moving targets and obstacles, online estimation of the system parameters and observer/controller combination for trajectory tracking in the 3D environment. Further developments and experiments are required to verify the performance of the proposed structures. The designed observer can be studied separately to provide information about the needle tip orientation to improve the image processing and needle tip tracking.

Other controllers can be used in the PWM switching framework, and the performance of these methods regarding positioning error and tissue trauma can be studied. Moreover, the observers can be combined with other controllers taking the parameter uncertainties into account. As well, the proposed controller, observer and extended model can be combined

to account for tissue inhomogeneity and form a general needle steering structure in the 3D environment. Adaptation laws can also be incorporated into these structures to have an online estimation of the needle path curvature to improve the accuracy of the methods. Finally, the methods can be combined with path planning techniques to avoid stationary and moving obstacles. To this end, further developments and different structures and controller/observer combinations are required which remain as future goals.

References

[1] B. Fallahi, R. S. Sloboda, and M. Tavakoli, "Applications of observers in medical robotics," *at-Automatisierungstechnik*, vol. 66, no. 3, pp. 268–279, 2018.

[2] B. Fallahi, C. Rossa, R. S. Sloboda, N. Usmani, and M. Tavakoli, "Sliding-based switching control for image-guided needle steering in soft tissue," *IEEE Robotics and Automation Letters*, vol. 1, no. 2, pp. 860–867, 2016.

[3] B. Fallahi, R. Sloboda, N. Usmani, and M. Tavakoli, "Model averaging and input transformation for 3D needle steering," *Journal of Medical Robotics Research*, p. 1841004, 2018.

[4] B. Fallahi, C. Rossa, R. S. Sloboda, N. Usmani, and M. Tavakoli, "Sliding-based image-guided 3D needle steering in soft tissue," *Control Engineering Practice*, vol. 63, pp. 34–43, 2017.

[5] B. Fallahi, C. Rossa, R. Sloboda, N. Usmani, and M. Tavakoli, "Partial estimation of needle tip orientation in generalized coordinates in ultrasound image-guided needle insertion," in *IEEE International Conference on Advanced Intelligent Mechatronics (AIM), 2016.* IEEE, 2016, pp. 1604–1609.

[6] B. Fallahi, M. Khadem, C. Rossa, R. Sloboda, N. Usmani, and M. Tavakoli, "Extended bicycle model for needle steering in soft tissue," in *Intelligent Robots and Systems (IROS), 2015 IEEE/RSJ International Conference on.* IEEE, 2015, pp. 4375–4380.

[7] L. A. Torre, F. Bray, R. L. Siegel, J. Ferlay, J. Lortet-Tieulent, and A. Jemal, "Global cancer statistics, 2012," *CA: a cancer journal for clinicians*, vol. 65, no. 2, pp. 87–108, 2015.

[8] R. Taschereau, J. Pouliot, J. Roy, and D. Tremblay, "Seed misplacement and stabilizing needles in transperineal permanent prostate implants," *Radiotherapy and Oncology*, vol. 55, no. 1, pp. 59–63, 2000.

[9] S. P. DiMaio and S. E. Salcudean, "Needle insertion modeling and simulation," *IEEE Transactions onRobotics and Automation*, vol. 19, no. 5, pp. 864–875, 2003.

[10] R. Alterovitz, K. Goldberg, J. Pouliot, R. Taschereau, I. Hsu *et al.*, "Needle insertion and radioactive seed implantation in human tissues: Simulation and sensitivity analysis," in *Proceedings of the IEEE International Conference on Robotics and Automation, ICRA 2003.*, vol. 2. IEEE, 2003, pp. 1793–1799.

[11] S. P. DiMaio and S. E. Salcudean, "Interactive simulation of needle insertion models," *IEEE Transactions on Biomedical Engineering*, vol. 52, no. 7, pp. 1167–1179, 2005.

[12] O. Goksel, S. E. Salcudean, and S. P. Dimaio, "3D simulation of needle-tissue interaction with application to prostate brachytherapy," *Computer Aided Surgery*, vol. 11, no. 6, pp. 279–288, 2006.

[13] E. Dehghan and S. E. Salcudean, "Needle insertion parameter optimization for brachytherapy," *IEEE Transactions on Robotics*, vol. 25, no. 2, pp. 303–315, 2009.

[14] K. Yan, W. S. Ng, K. V. Ling, Y. Yu, T. Podder, T.-I. Liu, and C. Cheng, "Needle steering modeling and analysis using unconstrained modal analysis," in *The First IEEE/RAS-EMBS International Conference on Biomedical Robotics and Biomechatronics, BioRob 2006.* IEEE, 2006, pp. 87–92.

[15] K. G. Yan, T. Podder, Y. Yu, T.-I. Liu, C. W. Cheng, and W. S. Ng, "Flexible needle–tissue interaction modeling with depth-varying mean parameter: preliminary study," *IEEE Transactions on Biomedical Engineering*, vol. 56, no. 2, pp. 255–262, 2009.

[16] N. Chentanez, R. Alterovitz, D. Ritchie, L. Cho, K. K. Hauser, K. Goldberg, J. R. Shewchuk, and J. F. O'Brien, *Interactive simulation of surgical needle insertion and steering*. ACM, 2009, vol. 28, no. 3.

[17] O. Goksel, E. Dehghan, and S. E. Salcudean, "Modeling and simulation of flexible needles," *Medical engineering & physics*, vol. 31, no. 9, pp. 1069–1078, 2009.

[18] S. Misra, K. B. Reed, B. W. Schafer, K. Ramesh, and A. M. Okamura, "Mechanics of flexible needles robotically steered through soft tissue," *The International journal of robotics research*, 2010.

[19] R. J. Roesthuis, M. Abayazid, and S. Misra, "Mechanics-based model for predicting in-plane needle deflection with multiple bends," in *4th IEEE RAS & EMBS International Conference on Biomedical Robotics and Biomechatronics, BioRob 2012*. IEEE, 2012, pp. 69–74.

[20] R. J. Webster, J. S. Kim, N. J. Cowan, G. S. Chirikjian, and A. M. Okamura, "Nonholonomic modeling of needle steering," *The International Journal of Robotics Research*, vol. 25, no. 5-6, pp. 509–525, 2006.

[21] N. Hamzé, I. Peterlík, S. Cotin, and C. Essert, "Preoperative trajectory planning for percutaneous procedures in deformable environments," *Computerized Medical Imaging and Graphics*, vol. 47, pp. 16–28, 2016.

[22] F. Gîrbacia, D. Pîslă, S. Butnariu, B. Gherman, T. Gîrbacia, and N. Plitea, "An evolutionary computational algorithm for trajectory planning of an innovative parallel robot for brachytherapy," in *New Advances in Mechanisms, Mechanical Transmissions and Robotics*. Springer, 2017, pp. 427–435.

[23] R. Tsumura and H. Iwata, "Trajectory planning for abdominal fine needle insertion based on insertion angles," *IEEE Robotics and Automation Letters*, vol. 2, no. 2, pp. 1226–1231, 2017.

[24] R. Alterovitz, K. Goldberg, and A. Okamura, "Planning for steerable bevel-tip needle insertion through 2D soft tissue with obstacles," in *Proceedings of the 2005 IEEE International Conference on Robotics and Automation, 2005. ICRA 2005.* IEEE, 2005, pp. 1640–1645.

[25] R. Alterovitz, A. Lim, K. Goldberg, G. S. Chirikjian, and A. M. Okamura, "Steering flexible needles under Markov motion uncertainty," in *IEEE/RSJ International Conference on Intelligent Robots and Systems, 2005.(IROS 2005). 2005.* IEEE, 2005, pp. 1570–1575.

[26] R. Alterovitz, M. Branicky, and K. Goldberg, "Constant-curvature motion planning under uncertainty with applications in image-guided medical needle steering," in *Algorithmic Foundation of Robotics VII*. Springer, 2008, pp. 319–334.

[27] W. Park, J. S. Kim, Y. Zhou, N. J. Cowan, A. M. Okamura, and G. S. Chirikjian, "Diffusion-based motion planning for a nonholonomic flexible needle model," in *Proceedings of the 2005 IEEE International Conference on Robotics and Automation, 2005. ICRA 2005.* IEEE, 2005, pp. 4600–4605.

[28] M. Khadem, C. Rossa, N. Usmani, R. S. Sloboda, and M. Tavakoli, "Semi-automated needle steering in biological tissue using an ultrasound-based deflection predictor," *Annals of biomedical engineering*, vol. 45, no. 4, pp. 924–938, 2017.

[29] J. Xu, V. Duindam, R. Alterovitz, and K. Goldberg, "Motion planning for steerable needles in 3D environments with obstacles using rapidly-exploring random trees and backchaining," in *IEEE International Conference on Automation Science and Engineering, 2008. CASE 2008.* IEEE, 2008, pp. 41–46.

[30] V. Duindam, R. Alterovitz, S. Sastry, and K. Goldberg, "Screw-based motion planning for bevel-tip flexible needles in 3D environments with obstacles," in *IEEE International Conference on Robotics and Automation, 2008. ICRA 2008.* IEEE, 2008, pp. 2483–2488.

[31] D. S. Minhas, J. A. Engh, M. M. Fenske, and C. N. Riviere, "Modeling of needle steering via duty-cycled spinning," in *Engineering in Medicine and Biology Society, 2007. EMBS 2007. 29th Annual International Conference of the IEEE.* IEEE, 2007, pp. 2756–2759.

[32] A. Majewicz, J. J. Siegel, A. A. Stanley, and A. M. Okamura, "Design and evaluation of duty-cycling steering algorithms for robotically-driven steerable needles," in *IEEE International Conference on Robotics and Automation (ICRA), 2014.* IEEE, 2014, pp. 5883–5888.

[33] S. Patil and R. Alterovitz, "Interactive motion planning for steerable needles in 3D environments with obstacles," in *3rd IEEE RAS and EMBS International Conference on Biomedical Robotics and Biomechatronics (BioRob), 2010.* IEEE, 2010, pp. 893–899.

[34] G. J. Vrooijink, M. Abayazid, S. Patil, R. Alterovitz, and S. Misra, "Needle path planning and steering in a three-dimensional non-static environment using two-

REFERENCES

dimensional ultrasound images," *The International journal of robotics research*, vol. 33, no. 10, pp. 1361–1374, 2014.

[35] S. Patil, J. Burgner, R. J. Webster, and R. Alterovitz, "Needle steering in 3-D via rapid replanning," *IEEE Transactions on Robotics*, vol. 30, no. 4, pp. 853–864, 2014.

[36] W. Sun, S. Patil, and R. Alterovitz, "High-frequency replanning under uncertainty using parallel sampling-based motion planning," *IEEE Transactions on Robotics*, vol. 31, no. 1, pp. 104–116, 2015.

[37] W. Sun, J. Van Den Berg, and R. Alterovitz, "Stochastic extended lqr: Optimization-based motion planning under uncertainty," in *Algorithmic Foundations of Robotics XI*. Springer, 2015, pp. 609–626.

[38] P. Li, S. Jiang, D. Liang, Z. Yang, Y. Yu, and W. Wang, "Modeling of path planning and needle steering with path tracking in anatomical soft tissues for minimally invasive surgery," *Medical engineering & physics*, vol. 41, pp. 35–45, 2017.

[39] P. Moreira, R. Patil, R. Alterovitz, and S. Misra, "Needle steering in biological tissue using ultrasound-base online curvature estimation," in *& International Conference on Robotics and Automation (ICRA), 2014*. IEEE, 2014.

[40] K. B. Reed, V. Kallem, R. Alterovitz, K. Goldbergxz, A. M. Okamura, and N. J. Cowan, "Integrated planning and image-guided control for planar needle steering," in *2nd IEEE RAS & EMBS International Conference on Biomedical Robotics and Biomechatronics, 2008. BioRob 2008*. IEEE, 2008, pp. 819–824.

[41] N. Abolhassani, R. V. Patel, and F. Ayazi, "Minimization of needle deflection in robot-assisted percutaneous therapy," *The international journal of medical Robotics and computer assisted surgery*, vol. 3, no. 2, pp. 140–148, 2007.

[42] A. Haddadi, O. Goksel, S. E. Salcudean, and K. Hashtrudi-Zaad, "On the controllability of dynamic model-based needle insertion in soft tissue," in *Engineering in Medicine and Biology Society (EMBC), 2010 Annual International Conference of the IEEE*. IEEE, 2010, pp. 2287–2291.

[43] M. Khadem, C. Rossa, R. S. Sloboda, N. Usmani, and M. Tavakoli, "Ultrasound-guided model predictive control of needle steering in biological tissue," *Journal of Medical Robotics Research*, vol. 1, no. 01, p. 1640007, 2016.

[44] J. Sovizi, S. Kumar, and V. Krovi, "Approximating Markov chain approach to optimal feedback control of a flexible needle," *Journal of Dynamic Systems, Measurement, and Control*, vol. 138, no. 11, p. 111006, 2016.

[45] M. Abayazid, G. J. Vrooijink, S. Patil, R. Alterovitz, and S. Misra, "Experimental evaluation of ultrasound-guided 3D needle steering in biological tissue," *International journal of computer assisted radiology and surgery*, vol. 9, no. 6, pp. 931–939, 2014.

[46] D. C. Rucker, J. Das, H. B. Gilbert, P. J. Swaney, M. I. Miga, N. Sarkar, and R. J. Webster, "Sliding mode control of steerable needles," *IEEE Transactions on Robotics*, vol. 29, no. 5, pp. 1289–1299, 2013.

[47] V. Kallem and N. J. Cowan, "Image guidance of flexible tip-steerable needles," *Robotics, IEEE Transactions on*, vol. 25, no. 1, pp. 191–196, 2009.

[48] M. Motaharifar, H. A. Talebi, A. Afshar, and F. Abdollahi, "Adaptive observer-based controller design for a class of nonlinear systems with application to image guided control of steerable needles," in *American Control Conference (ACC), 2012*. IEEE, 2012, pp. 4849–4854.

[49] P. Moreira and S. Misra, "Biomechanics-based curvature estimation for ultrasound-guided flexible needle steering in biological tissues," *Annals of biomedical engineering*, pp. 1–11, 2014.

[50] M. Abayazid, M. Kemp, and S. Misra, "3D flexible needle steering in soft-tissue phantoms using fiber Bragg grating sensors," in *IEEE International Conference on Robotics and Automation (ICRA), 2013*. IEEE, 2013, pp. 5843–5849.

[51] N. Shahriari, E. Hekman, M. Oudkerk, and S. Misra, "Design and evaluation of a computed tomography CT-compatible needle insertion device using an electromagnetic tracking system and CT images," *International journal of computer assisted radiology and surgery*, pp. 1–8, 2015.

[52] N. Popescu, D. Popescu, M. Ivanescu, D. Popescu, C. Vladu, and I. Vladu, "Force observer-based control for a rehabilitation hand exoskeleton system," in *9th Asian Control Conference (ASCC)*. IEEE, 2013, pp. 1–6.

[53] T. Haidegger, B. Benyó, L. Kovács, and Z. Benyó, "Force sensing and force control for surgical robots," *IFAC Proceedings Volumes*, vol. 42, no. 12, pp. 401–406, 2009.

[54] B. Siciliano and O. Khatib, *Springer handbook of robotics*. Springer, 2016.

[55] S. Viteckova, P. Kutilek, and M. Jirina, "Wearable lower limb robotics: A review," *Biocybernetics and Biomedical Engineering*, vol. 33, no. 2, pp. 96–105, 2013.

[56] S. A. Kolakowsky-Hayner, J. Crew, S. Moran, and A. Shah, "Safety and feasibility of using the ekso bionic exoskeleton to aid ambulation after spinal cord injury," *J Spine*, vol. 4, p. 003, 2013.

[57] P. Beyl, K. Knaepen, S. Duerinck, M. Van Damme, B. Vanderborght, R. Meeusen, and D. Lefeber, "Safe and compliant guidance by a powered knee exoskeleton for robot-assisted rehabilitation of gait," *Advanced Robotics*, vol. 25, no. 5, pp. 513–535, 2011.

[58] P. Heo, G. M. Gu, S.-j. Lee, K. Rhee, and J. Kim, "Current hand exoskeleton technologies for rehabilitation and assistive engineering," *International Journal of Precision Engineering and Manufacturing*, vol. 13, no. 5, pp. 807–824, 2012.

[59] B. Chen, H. Ma, L.-Y. Qin, F. Gao, K.-M. Chan, S.-W. Law, L. Qin, and W.-H. Liao, "Recent developments and challenges of lower extremity exoskeletons," *Journal of Orthopaedic Translation*, vol. 5, pp. 26–37, 2016.

[60] I. Díaz, J. J. Gil, and E. Sánchez, "Lower-limb robotic rehabilitation: literature review and challenges," *Journal of Robotics*, vol. 2011, 2011.

[61] P. Maciejasz, J. Eschweiler, K. Gerlach-Hahn, A. Jansen-Troy, and S. Leonhardt, "A survey on robotic devices for upper limb rehabilitation," *Journal of neuroengineering and rehabilitation*, vol. 11, no. 1, p. 3, 2014.

[62] A. Mohammadi, M. Tavakoli, H. Marquez, and F. Hashemzadeh, "Nonlinear disturbance observer design for robotic manipulators," *Control Engineering Practice*, vol. 21, no. 3, pp. 253–267, 2013.

[63] W.-H. Chen, D. J. Ballance, P. J. Gawthrop, and J. O'Reilly, "A nonlinear disturbance observer for robotic manipulators," *IEEE Transactions on industrial Electronics*, vol. 47, no. 4, pp. 932–938, 2000.

[64] C. Mitsantisuk and K. Ohishi, "Robotics-assisted rehabilitation therapy for the hands and wrists using force sensorless bilateral control with shadow and mirror mode," in *IEEE International Conference on Mechatronics (ICM)*. IEEE, 2015, pp. 541–546.

[65] A. U. Pehlivan, D. P. Losey, and M. K. O'Malley, "Minimal assist-as-needed controller for upper limb robotic rehabilitation," *IEEE Transactions on Robotics*, vol. 32, no. 1, pp. 113–124, 2016.

[66] S. A. Fakoorian, V. Azimi, M. Moosavi, H. Richter, and D. Simon, "Ground reaction force estimation in prosthetic legs with nonlinear kalman filtering methods," *Journal of Dynamic Systems, Measurement, and Control*, 2017.

[67] C. Mitsantisuk, S. Katsura, and K. Ohishi, "Kalman-filter-based sensor integration of variable power assist control based on human stiffness estimation," *IEEE Transactions on Industrial Electronics*, vol. 56, no. 10, pp. 3897–3905, 2009.

[68] A. M. Okamura, C. Simone, and M. D. O'leary, "Force modeling for needle insertion into soft tissue," *IEEE transactions on biomedical engineering*, vol. 51, no. 10, pp. 1707–1716, 2004.

[69] M. R. Kermani, R. V. Patel, and M. Moallem, "Friction identification and compensation in robotic manipulators," *IEEE Transactions on Instrumentation and Measurement*, vol. 56, no. 6, pp. 2346–2353, 2007.

[70] A. Asadian, M. R. Kermani, and R. V. Patel, "A novel force modeling scheme for needle insertion using multiple kalman filters," *IEEE Transactions on Instrumentation and Measurement*, vol. 61, no. 2, pp. 429–438, 2012.

[71] Y. Fukushima and K. Naemura, "Estimation of the friction force during the needle insertion using the disturbance observer and the recursive least square," *ROBOMECH Journal*, vol. 1, no. 1, pp. 1–8, 2014.

[72] A. Maghsoudi and M. Jahed, "A comparison between disturbance observer-based and model-based control of needle in percutaneous applications," in *38th Annual Conference on IEEE Industrial Electronics Society, IECON*. IEEE, 2012, pp. 2104–2108.

[73] T. Murakami, F. Yu, and K. Ohnishi, "Torque sensorless control in multidegree-of-freedom manipulator," *IEEE Transactions on Industrial Electronics*, vol. 40, no. 2, pp. 259–265, 1993.

[74] D. Suzuki, K. Yu, and K. Ohnishi, "A quantitative stiffness assessment method in liver biopsy teleoperations," in *39th Annual Conference of the IEEE Industrial Electronics Society, IECON*. IEEE, 2013, pp. 3281–3286.

[75] A. Hagemann, K. Rohr, H. S. Stiehl, U. Spetzger, and J. M. Gilsbach, "Biomechanical modeling of the human head for physically based, nonrigid image registration," *IEEE transactions on medical imaging*, vol. 18, no. 10, pp. 875–884, 1999.

[76] M. Hu, G. Penney, M. Figl, P. Edwards, F. Bello, R. Casula, D. Rueckert, and D. Hawkes, "Reconstruction of a 3D surface from video that is robust to missing data and outliers: Application to minimally invasive surgery using stereo and mono endoscopes," *Medical image analysis*, vol. 16, no. 3, pp. 597–611, 2012.

[77] M. Sauvée, A. Noce, P. Poignet, J. Triboulet, and E. Dombre, "Three-dimensional heart motion estimation using endoscopic monocular vision system: From artificial landmarks to texture analysis," *Biomedical Signal Processing and Control*, vol. 2, no. 3, pp. 199–207, 2007.

[78] R. Richa, P. Poignet, and C. Liu, "Three-dimensional motion tracking for beating heart surgery using a thin-plate spline deformable model," *The International Journal of Robotics Research*, vol. 29, no. 2-3, pp. 218–230, 2010.

[79] B. Yang, W.-K. Wong, C. Liu, and P. Poignet, "3D soft-tissue tracking using spatial-color joint probability distribution and thin-plate spline model," *Pattern recognition*, vol. 47, no. 9, pp. 2962–2973, 2014.

[80] T. Ortmaier, M. Groger, D. H. Boehm, V. Falk, and G. Hirzinger, "Motion estimation in beating heart surgery," *IEEE Transactions on Biomedical Engineering*, vol. 52, no. 10, pp. 1729–1740, 2005.

[81] A. Thakral, J. Wallace, D. Tomlin, N. Seth, and N. Thakor, "Surgical motion adaptive robotic technology (smart): Taking the motion out of physiological motion," in *Medical Image Computing and Computer-Assisted Intervention–MICCAI 2001*. Springer, 2001, pp. 317–325.

[82] S. G. Yuen, P. M. Novotny, and R. D. Howe, "Quasiperiodic predictive filtering for robot-assisted beating heart surgery," in *IEEE International Conference on Robotics and Automation, ICRA*, 2008, pp. 3875–3880.

[83] M. Bowthorpe and M. Tavakoli, "Physiological organ motion prediction and compensation based on multirate, delayed, and unregistered measurements in robot-assisted surgery and therapy," *IEEE/ASME Transactions on Mechatronics*, vol. 21, no. 2, pp. 900–911, 2016.

[84] S. Yuen, S. Kesner, N. Vasilyev, P. Del Nido, and R. Howe, "3D ultrasound-guided motion compensation system for beating heart mitral valve repair," *Medical Image Computing and Computer-Assisted Intervention–MICCAI 2008*, pp. 711–719, 2008.

[85] R. Richa, A. P. Bó, and P. Poignet, "Towards robust 3D visual tracking for motion compensation in beating heart surgery," *Medical Image Analysis*, vol. 15, no. 3, pp. 302–315, 2011.

[86] B. Yang, C. Liu, W. Zheng, and S. Liu, "Motion prediction via online instantaneous frequency estimation for vision-based beating heart tracking," *Information Fusion*, vol. 35, pp. 58–67, 2017.

[87] C. Rossa and M. Tavakoli, "Issues in closed-loop needle steering," *Control Engineering Practice*, vol. 62, pp. 55–69, 2017.

[88] P. Moreira and S. Misra, "Biomechanics-based curvature estimation for ultrasound-guided flexible needle steering in biological tissues," *Annals of biomedical engineering*, vol. 43, no. 8, pp. 1716–1726, 2015.

[89] M. Waine, C. Rossa, R. Sloboda, N. Usmani, and M. Tavakoli, "Three-dimensional needle shape estimation in trus-guided prostate brachytherapy using 2-D ultrasound images," *IEEE journal of biomedical and health informatics*, vol. 20, no. 6, pp. 1621–1631, 2016.

[90] T. Lehmann, M. Tavakoli, N. Usmani, and R. Sloboda, "Force-sensor-based estimation of needle tip deflection in brachytherapy," *Journal of Sensors*, vol. 2013, 2013.

[91] H. D. Taghirad, *Parallel robots: mechanics and control*. CRC press, 2013.

[92] V. Utkin *et al.*, "Sliding mode control design principles and applications to electric drives," *IEEE Transactions on Industrial Electronics*, vol. 40, no. 1, pp. 23–36, 1993.

[93] T. Podder, D. Clark, D. Fuller, J. Sherman, W. Ng, L. Liao, D. Rubens, J. Strang, E. Messing, Y. Zhang *et al.*, "Effects of velocity modulation during surgical needle insertion," in *IEEE-EMBS 2005. 27th Annual International Conference of the Engineering in Medicine and Biology Society, 2005.* IEEE, 2005, pp. 5766–5770.

[94] P. J. Swaney, J. Burgner, H. B. Gilbert, and R. J. Webster, "A flexure-based steerable needle: high curvature with reduced tissue damage," *IEEE Transactions on Biomedical Engineering*, vol. 60, no. 4, pp. 906–909, 2013.

[95] J.-J. E. Slotine, W. Li *et al.*, *Applied nonlinear control.* Prentice hall Englewood Cliffs, NJ, 1991, vol. 199, no. 1.

[96] M. Abayazid, P. Moreira, N. Shahriari, S. Patil, R. Alterovitz, and S. Misra, "Ultrasound-guided three-dimensional needle steering in biological tissue with curved surfaces," *Medical engineering & physics*, vol. 37, no. 1, pp. 145–150, 2015.

[97] S. J. Dodds *et al.*, "Feedback control," *London: Springer*, p. 5, 2015.

[98] M. Khadem, C. Rossa, N. Usmani, R. S. Sloboda, and M. Tavakoli, "Introducing notched flexible needles with increased deflection curvature in soft tissue," in

Advanced Intelligent Mechatronics (AIM), 2016 IEEE International Conference on. IEEE, 2016, pp. 1186–1191.

[99] K. Wallner, W. Ellis, K. Russell, W. Cavanagh, and J. Blasko, "Use of trus to predict pubic arch interference of prostate brachytherapy," *International Journal of Radiation Oncology Biology Physics*, vol. 43, no. 3, pp. 583–585, 1999.

[100] J. Fukada, N. Shigematsu, J. Nakashima, T. Ohashi, O. Kawaguchi, and M. Oya, "Predicting pubic arch interference in prostate brachytherapy on transrectal ultrasonography-computed tomography fusion images," *Journal of radiation research*, pp. 753–759, 2012.

[101] S.-J. Zhang, H.-N. Qian, Y. Zhao, K. Sun, H.-Q. Wang, G.-Q. Liang, F.-H. Li, and Z. Li, "Relationship between age and prostate size," *Asian J Androl*, vol. 15, no. 1, pp. 116–120, 2013.

[102] A. Krupa, "3D steering of a flexible needle by visual servoing," in *International Conference on Medical Image Computing and Computer-Assisted Intervention*. Springer, 2014, pp. 480–487.

[103] G. Besançon, *Nonlinear observers and applications*. Springer, 2007, vol. 363.

[104] A. Vargas and J. A. Moreno, "Approximate high-gain observers for non-lipschitz observability forms," *International Journal of Control*, vol. 78, no. 4, pp. 247–253, 2005.

[105] T. Hu, Z. Lin, and B. M. Chen, "An analysis and design method for linear systems subject to actuator saturation and disturbance," *Automatica*, vol. 38, no. 2, pp. 351–359, 2002.

Appendix A

Bicycle Model for Needle

Consider the needle shown in Fig. 1.4. In this model, the insertion velocity is equal to wheel rolling velocity v_z in the body frame $\{B\}$. Due to the planar motion of the bicycle, the velocity of frame $\{B\}$ along its x axis is zero. Writing in body frame this constraint can be expressed as

$$e_1^T v_{ab}^b = 0 \tag{A.1}$$

Since the velocity of frame $\{B\}$ does not have any projections along its y axis, it can be written in the body frame as

$$e_2^T v_{ab}^b = 0 \tag{A.2}$$

Moreover, since the front wheel frame $\{C\}$ is rigidly connected to the back wheel frame the relative linear and angular velocity of the frame $\{C\}$ with respect to frame $\{B\}$ is zero. The velocity constraints of the body frame $\{C\}$ can be expressed in body frame as

$$e_1^T v_{ac}^b = e_2^T v_{ac}^b = 0 \tag{A.3}$$

in these equations v_{ab}^b and v_{ac}^b denote the linear velocity of the body frames $\{B\}$ and $\{C\}$ with respect to the fixed frame $\{A\}$ expressed in body frames, respectively and the vectors $e_i, i = 1, 2, 3$, represent the standard basis vectors in $\mathbb{R}^3$. Equations (A.1)-(A.3) can be simplified to

$$\begin{bmatrix} 1 & 0 & 0 & 0 & 0 & 0 \\ 0 & 1 & 0 & 0 & 0 \\ 0 & 0 & 1 & -\frac{1}{k} & 0 & 0 \\ 0 & 0 & 0 & 0 & 1 & 0 \end{bmatrix} V_{ab}^b = 0 \tag{A.4}$$

in which $k = \tan \phi \ell_1^{-1}$ denote the constant curvature of the needle tip path. $V_{ab}^b = \begin{bmatrix} v_{ab}^b & \omega_{ab}^b \end{bmatrix}^T$ is the 6-DOF representation of linear and angular velocities of the moving frame $\{B\}$. For $\ell_1 \neq 0$ and $\phi \in [0, \pi/2]$, solving for the null space of the matrix in (A.4) leads to the kinematic equation (1.1).

Appendix B

Extended Bicycle model

In this chapter, we propose an extension to the kinematic bicycle model that will account for needle tip deflection with non-constant curvature. Using experimental data from needle insertion into different phantom tissues, we show that the radius of curvature of the needle tip path is influenced by the tissue stiffness. The kinematic bicycle model is modified to have new parameters enabling one to account for path variations caused by tissue deformation.

B.1   Equations

In this section, we extend the bicycle model for a needle that follows a non-constant curvature path in tissue. The modified model incorporates new parameters to the bicycle's kinematic equations to account for deviations of the needle path from a circle. The effect of tissue deformation can be interpreted as letting the needle have sideways movements orthogonal to the insertion direction. These movements are modeled by slippage of the bicycle wheels. As explained in the previous section, the original kinematic bicycle equations were derived by imposing the pure roll and non-slip constraints on the wheels.

In order to allow for sideways motion of the needle, we replace the back wheel of the bicycle with a wheel that is able to move in two directions. Omni-directional wheels shown in Fig. B.1(a) can move independently in two orthogonal directions. Such wheels satisfy the wheel plane constraint but violate the non-slip constraint. Orthogonal to the wheel plane, the motion constraint will be

$$^{B}v_y - \omega R = 0 \tag{B.1}$$

in which ω_R denotes the rotation velocity of the rollers. This is the degree of freedom added to the system allowing the wheel to have lateral movements.

Here, we replace the back wheel of the bicycle with the omni-directional wheel of Fig. B.1(a), as shown in Fig. B.1(b). In this figure, ϕ, ℓ and α denote the fixed front wheel angle, the distance between the two wheels and the rotation angle of the needle tip in body frame $\{B\}$, respectively. This rotation of the needle tip from the insertion direction by angle θ is
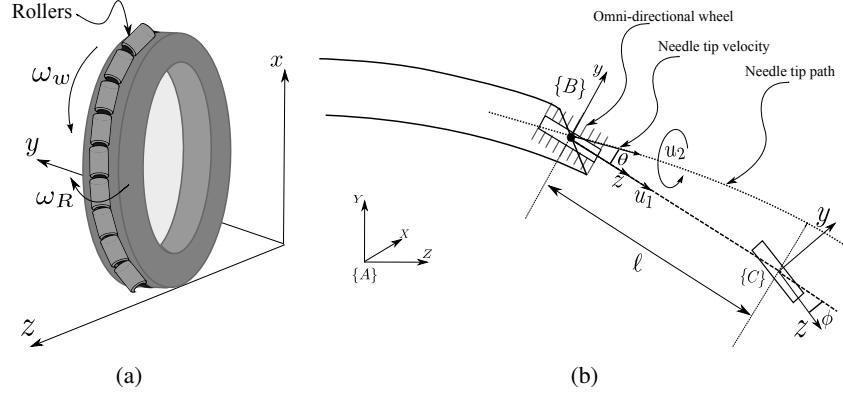
Figure B.1: (a): An omni-directional wheel represents the bicycles back wheel. (b): Modified bicycle model of a bevel tip needle. The frames $\{C\}$ and $\{B\}$ are attached to front and back wheels. The back wheel is located at needle tip

due to the lateral movement of the back wheel causing the needle to be tangent to the non-circular path. The inputs u_1 and u_2 denote the insertion velocity along the z axis of frame $\{B\}$ (which equals ^Bv_z) and the rotation velocity of the needle about its axis, respectively.

The lateral movements of the back wheel enables us to model the deviations of the needle tip trajectory from a circular path predicted by the conventional bicycle model. While the front wheel satisfies the pure rolling and non-slipping constraints of conventional wheels, the back wheel satisfies the roll and slip constraints Therefore, the kinematic constraints on the front and back wheels are different.

The non-zero slip velocity is our modification to the conventional bicycle model. This value simulates the tissue deformation that deviates the needle tip position from a circular path. Since the amount of tissue compression depends on needle deflection, and the tip deflection and tip angle are related through trigonometric functions, we will consider ^Bv_y as a function of needle tip angle. Moreover, the lateral movements can only happen when the needle is moving forward into tissue. In other words, when the insertion velocity ^Bv_z is zero there will be no lateral movements. Accordingly, let us define the slippage equation of the back wheel as

$$^Bv_y = f(\alpha', \lambda)\,^Bv_z \tag{B.2}$$

in which λ is a tissue specific parameter (related to its mechanical properties) and f is an arbitrary function that we will define later that relates λ to the amount of lateral movements.

APPENDIX B. EXTENDED BICYCLE MODEL

The angle α' is the needle tip rotation in the fixed frame $\{A\}$ and is equal to $\alpha + \theta$. For a stiff tissue, λ equals zero and the needle tip travels on a circular path with $^B v_y = 0$, which implies $f(\alpha, 0) = 0$. Using (B.2) and the constraints on the front and back wheels, the time variations of the back wheel angle is obtained as

$$\dot{\alpha} = \frac{1}{l}[tan\phi + f(\alpha', \lambda)]^B v_z \tag{B.3}$$

In (B.3), $\dot{\alpha}$ is composed of two terms. The latter term represents the correction done to the original constant curvature solution using slippage of the back wheel. Using (B.2), the needle tip angle in body frame $\{B\}$ is found as

$$\theta = tan^{-1}\left(\frac{^B v_y}{^B v_z}\right) = tan^{-1}(f(\alpha', \lambda)). \tag{B.4}$$

Using (B.2) and (B.4), the kinematics of the modified bicycle can be written as

$$\dot{y} = \left(\frac{sin\alpha'}{cos\theta}\right)^B v_z \tag{B.5a}$$

$$\dot{z} = \left(\frac{cos\alpha'}{cos\theta}\right)^B v_z \tag{B.5b}$$

$$\dot{\alpha'} = \frac{\dot{\alpha}}{1 - \partial\theta/\partial\alpha'} \tag{B.5c}$$

in which $\partial\theta/\partial\alpha'$ is the partial derivative of α with respect to α' and $\dot{\alpha}$ is defined in (B.3). Similar to equations (A.1) and (A.3), (B.5) can be written in the body frame $\{B\}$ as

$$e_1^T v_{ab}^b = 0 \tag{B.6a}$$

$$e_2^T v_{ab}^b = f(\alpha', \lambda)e_3^T v_{ab}^b \tag{B.6b}$$

$$e_1^T \omega_{ab}^b = \frac{1}{\ell}(tan\phi - f(\alpha', \lambda))e_3^T v_{ab}^b \tag{B.6c}$$

$$e_2^T \omega_{ab}^b = 0 \tag{B.6d}$$

99

APPENDIX B. EXTENDED BICYCLE MODEL

The equations (B.6b)-(B.6d) can be simplified to

$$
\begin{bmatrix}
1 & 0 & 0 & 0 & 0 & 0 \\
0 & 1 & -f(\alpha',\lambda) & 0 & 0 & 0 \\
0 & 0 & 1 & -\frac{\ell}{\ell k - f(\alpha',\lambda)} & 0 & 0 \\
0 & 0 & 0 & 0 & 1 & 0
\end{bmatrix}
V_{ab}^b = 0
\tag{B.7}
$$

in which $k = tan\phi\ell^{-1}$. As expected for $\lambda = 0$, (B.7) is equivalent to (A.4). Thus, the kinematic model (1.1) is found as $\dot{g}_{ab}(t) = g_{ab}(t)(u_1 V_1 + u_2 V_2)$ with $V_1 = \begin{bmatrix} 0 & f(\alpha',\lambda) & 1 & k - \frac{f(\alpha',\lambda)}{\ell} & 0 & 0 \end{bmatrix}^T$ and $V_2 = \begin{bmatrix} 0 & e_3^T \end{bmatrix}^T$.

B.2 Constraints on the Slippage Equation

In this section, we determine the constraints on the parameters of (B.2) for which the kinematics equations (B.5) can be solved. Assuming that the needle tip angle relative to the fixed and the body frames take values in the range $[-\pi/2, \pi/2]$, the kinematic equations of the modified bicycle model can only be solved if the following conditions are satisfied:

$$
cos(\theta) \neq 0 \rightarrow \theta \neq \pm\frac{\pi}{2}
\tag{B.8}
$$

$$
1 - \frac{\partial\theta}{\partial\alpha'} \neq 0
\tag{B.9}
$$

in which $\pm$ is selected depending on whether the needle tip points upward or downward. To derive these conditions and in order to keep the analysis traceable and avoiding complexities, the angle θ that gives the slippage of the back wheel through (B.4) is defined as

$$
\theta = \lambda_1 \alpha'^2 + \lambda_2 \alpha'.
\tag{B.10}
$$

To simplify the equation, we will assume the needle path points toward the negative y axis and $\alpha', \alpha \in [-\pi/2, 0]$. In this case, (B.8) simplifies to

$$
\lambda_1 > \frac{\lambda_2^2}{2\pi}.
\tag{B.11}
$$

100

Using this inequality, (B.9) can be written as

$$(1 - \lambda_2) - 2\lambda_1\alpha' > -\lambda_2^2\alpha'/\pi + (1 - \lambda_2). \tag{B.12}$$

For the right hand side of this inequality to be non-zero requires $\alpha' > -\pi/4$, which for $\alpha' \in [-\pi/2, 0]$ is acceptable and the right hand side will always be positive satisfying (B.9). From (B.11), if $\lambda_1 = 0$ then $\lambda_2 = 0$ and $\lambda_2 \neq 1$, which satisfies (B.9) for $\alpha' = 0$. Although this condition seems to be restrictive, one can see that the absolute value of needle angle obtained from experiments for soft tissues is usually less than $\pi/4$.

B.3 Experiments

In order to study the effect of tissue stiffness on the needle path, experiments are performed on different types of tissues samples with different stiffness using the experimental setup introduced in section 2.3. To assess the accuracy of the proposed model (B.5), the experiments are performed in two different transparent phantom tissues of two different types. The first tissue is made of plastisol gel (M-F Manufactoring Co., Fort Worth, USA) for which the amount of added plastic softener determines the stiffness of the tissue. The needle is inserted at two different velocities of 20 and 40 mm/sec. The second tissue is made of agar of type A360-500 (Fisher Scientific International Inc., Hampton, NH, USA) for which the ratio of agar to water used adjusts the stiffness of the tissue sample. The needle is inserted with constant insertion velocities of 20 and 60 mm/sec. In these experiments the insertion depth and needle tip deflection, are calculated from recorded images.

From (B.10), the unknown constant parameters λ_1 and λ_2 are to be found by using experimental data. These parameters are found by fitting (B.5c) to time variations of needle tip angle, $\dot{\alpha}'$, calculated from the experimental data. To this end, third order time dependent polynomials are fitted to the depth and deflection data and the needle tip angle is approximated by

$$\alpha' = sin^{-1}(\frac{\Delta y}{\Delta d}) \tag{B.13}$$

in which Δy and Δd denote the variations of the deflection and depth between two sample times, respectively. Using the approximated α', its time variations is fitted to (B.5c) using
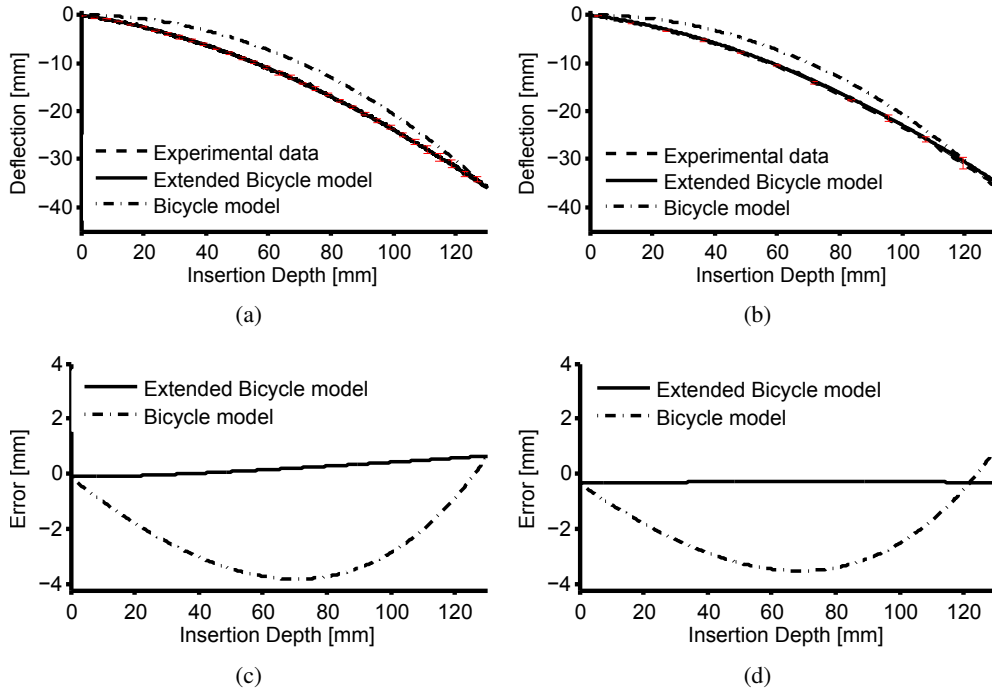
Figure B.2: Experimental results for needle insertion in agar tissue for different velocities. (a), (b): Needle deflection estimated from the modified bicycle model and the original bicycle model compared to experimental data for the insertion velocity of 20 mm/sec and 60 mm/sec, in agar tissue. (c), (d): Comparison of needle tip deflection estimation error for the modified bicycle model and the original bicycle model for the insertion velocity of 20 mm/sec and 60 mm/sec.

the `lsqcurvefit` function in Matlab. The obtained values for λ_1 and λ_2 are imported to the model equations (B.5) and the model is simulated for the same velocities as experiments.

For comparison, the experimental data is also fitted to standard bicycle model in which the needle path is estimated by a constant curvature path (circle). The results from both methods are shown in Fig. B.2 and Fig. B.3. In these figures, the simulated deflection is compared to the average of three trials. For the agar tissue, the maximum prediction error obtained is 0.66 mm and 3.79 for the extended bicycle model and the original bicycle model, respectively. For plastisol tissue, the maximum prediction error is 0.43 mm and 1.46 mm for the extended bicycle model and the original bicycle model, respectively. The results are summarized in Table B.1. Comparing the maximum errors, we can conclude that for these combination of needle and tissue, the modified bicycle model generates smaller errors which is obtained by introducing new parameters to the kinematic equations of bicycle.
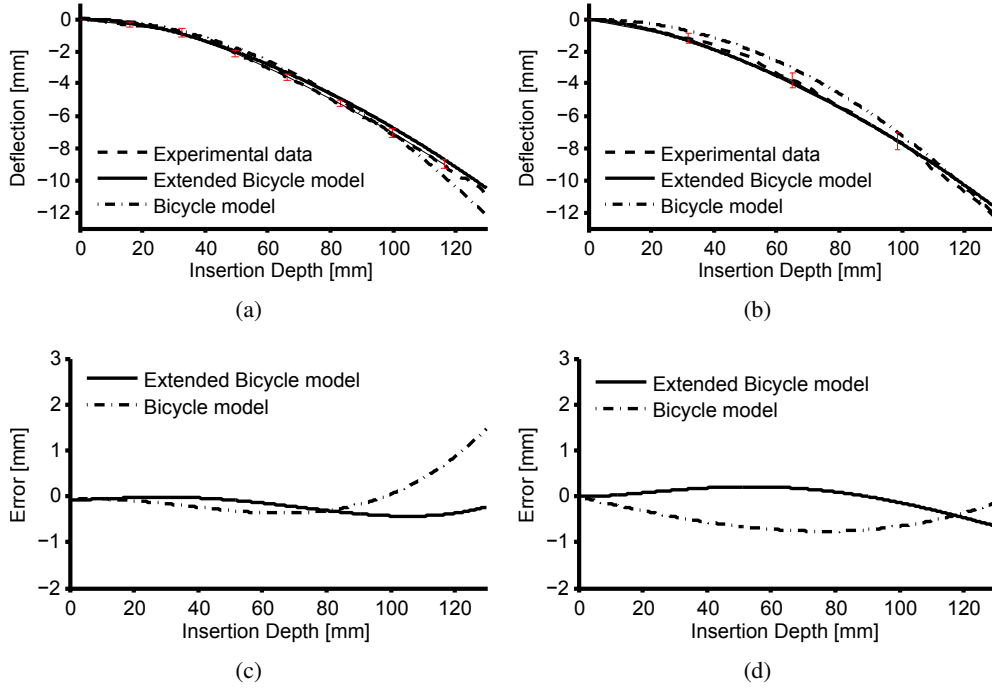
Figure B.3: Experimental results for needle insertion in plastisol tissue for different veloci-ties. (a), (b): Needle deflection estimated from the modified bicycle model and the original bicycle model compared to experimental data for the insertion velocity of 20 mm/sec and 60 mm/sec in plastisol tissue. (c), (d): Comparison of needle tip deflection estimation error for the modified bicycle model and the original bicycle model for the insertion velocity of 20 mm/sec and 60 mm/sec.

Table B.1: Identified model parameters and maximum error in needle tip estimation

Insertion parameters		Fitted model parameters		Maximum Error [mm]	
Tissue	Velocity [mm/sec]	λ_1	λ_2	Extended model	Bicycle model
Agar	20	0.49	0.22	**0.66**	3.79
	60			**0.33**	3.49
Plastisol	20	0.144	0.032	**0.43**	1.46
	40			**0.63**	0.76